IMAGE: A MAP OF THE STARS OF THE ORION CONSTELLATION

JournalPreview

London Journal of Engineering Research

Volume 24 | Issue 1 | Compilation 1.0

Great Britain Journals Press

WWW.JOURNALSPRESS.COM

JournalPreview

LONDON JOURNAL ENGINEERING RESEARCH

Journal Content
In this Issue

Great Britain Journals Press

Navigating Risks: A Comprehensive Functional Hazard Assessment of eVTOL Power Battery Systems

Wang Y., Baghai M. & Xiao G

Aviage Systems

ABSTRACT

With the advancement of the power battery and electric propulsion technology, the versatile redundancy enables the eVTOL aircraft design to be more reliable and cost-effective, thereby to be safer. This mandate the conducting of systematic aircraft level safety mitigation and comprehensive functional hazard assessment to ensure a fail-safe design, and process assurance to address the potential development errors in a pragmatic manner. After describing the application scenarios of eVTOL, the safety mitigation effects of applying crashworthiness and ballistic rescue system (BRS) on eVTOL aircraft were analyzed and elaborated, and the flight profile of eVTOL was refined based on the aircraft level safety objectives. Utilizing the commercial aircraft system engineering approach, an aircraft level functional hierarchy was proposed for eVTOL, emphasizing completeness and correctness. Insight of the innovative features of the electric power battery system, the well-established aircraft functional hazard assessment (FHA) methodology was deployed to scrutinize the functional invento.

Keywords: power battery system evtol functional hazard assessment fail-safe design process assurance.

Classification: LCC Code: TK1001-1841

Language: English

Great Britain Journals Press

LJP Copyright ID: 392921
Print ISSN: 2631-8474
Online ISSN: 2631-8482

London Journal of Engineering Research

Volume 24 | Issue 1 | Compilation 1.0

Navigating Risks: A Comprehensive Functional Hazard Assessment of eVTOL Power Battery Systems

Wang Y.[α], Baghai M.[σ] & Xiao G.[ρ]

ABSTRACT

With the advancement of the power battery and electric propulsion technology, the versatile redundancy enables the eVTOL aircraft design to be more reliable and cost-effective, thereby to be safer. This mandate the conducting of systematic aircraft level safety mitigation and comprehensive functional hazard assessment to ensure a fail-safe design, and process assurance to address the potential development errors in a pragmatic manner. After describing the application scenarios of eVTOL, the safety mitigation effects of applying crashworthiness and ballistic rescue system (BRS) on eVTOL aircraft were analyzed and elaborated, and the flight profile of eVTOL was refined based on the aircraft level safety objectives. Utilizing the commercial aircraft system engineering approach, an aircraft level functional hierarchy was proposed for eVTOL, emphasizing completeness and correctness. Insight of the innovative features of the electric power battery system, the well-established aircraft functional hazard assessment (FHA) methodology was deployed to scrutinize the functional inventory.

Utilizing the conventional power battery system architecture found in Electric Vehicle (EV), the pertinent functions of the eVTOL's power battery system have been allocated in order to identify potential weaknesses and opportunities for improvement from a safety perspective in extant EV power battery systems. Suggestions were made after discussions that, prior to installing existing power battery systems into eVTOL aircraft applications, developers must not only enhance the availability, reliability, and safety of the battery system, but also identify and mitigate single-point failures and design errors within the extant battery system to substantiate the compliance to safety courses in airworthiness regulations.

Keywords: power battery system evtol functional hazard assessment fail-safe design process assurance.

Author α: AVIAGE SYSTEMS, 666 Zixing Rd, Minhang, Shanghai 200241, China.
σ: AVIAGE SYSTEMS US, Peoria, AZ 85318, USA.
ρ: Shanghai Jiaotong University, Minhang, Shanghai 200240, China.

I. INTRODUCTION

As a novel component, the power battery system within electric Vertical TakeOff and Landing (eVTOL) aircraft introduces supplementary functionalities and components not found in traditional aircraft which is relying on fossil fuel-based power generation and distribution systems. Although the automobile functional safety is performed for Electric Vehicle (EV) power battery system, they do not align with the standards of aviation applications including eVTOL. The pressing concern within the eVTOL industry centers on establishing pragmatic and acceptable safety objectives for these systems and enhancing existing EV power battery systems to meet the safety requisites of eVTOL in a cost-effective manner.

To ensure the safe of flight for aircrafts, safety assessment methodology, system development processes, and SW/HW development standards have been established for commercial aviation [1]. The Functional Hazard Assessment (FHA) is of fundamental importance in civil aviation industry, for both air transportation and general aviation including eVTOL aircraft. A systematic FHA also

London Journal of Engineering Research

helps the designer to insightfully understand the functionality and safety risk at the very beginning, especially for the innovative portion of the aircraft, namely power battery system in eVTOL. It also contributes to the reasonable implementation fail-safe design and development assurance level definition.

II. AIRWORTHINESS CERTIFICATION REQUIREMENTS

Before industry development considerations in ARP 4754 (1996) [2], and even before System Safety Analysis and Assessment for Part 25 Airplanes in AC 25.1309-1 (1982) [3], the aviation industry utilized the function failure condition and severity to substantiate that "Catastrophic Failure Conditions must be Extremely Improbable" and "No single failure will result in a Catastrophic Failure Condition". The target and approach remain the same through the following decades, through the AC 25.1309-1A, AC 25.1309-1B arsenal draft, AC 20-174 and ARP 4754A [4]/ ARP 4761[5], and will remain in the same way for the next updated version ARP 4754B.

According to the latest airworthiness regulatory progress for eVTOL, the FHA is mandatory for design and development of eVTOL aircraft with and without occupants. Additional to the safety regulations applicable, the airworthiness criteria were defined for Model JAS4-1 Powered Lift, in whichFAA proposes that compliance with the criteria will provide an equivalent level of safety to existing rules. The clause, JS4.2430, addresses the criteria for electric energy systems [6]:

2.1 Each Energy System Must

1. *Be designed and arranged to provide independence between multiple energy-storage and supply systems, so that failure of any one component in one system will not result in loss of energy storage or supply of another system.*
2. *Be designed to prevent catastrophic events due to lightning strikes, taking into* account direct and indirect effects on the aircraft where the exposure to lightning is likely.

The same safety assessment method, including FHA, is applicable to the UAS eVTOL that is closest to actual operation without pilot, namely EH216-S. For details, please refer to the clause numbered PEU.F010 (Systems, Equipment, and Installation) in the Special Conditions issued by the Civil Aviation Administration of China [7]:

1. *Regarding for the System, Equipment and Installation included in PEU.F000(a), considered separately and in relation to other systems, must be designed so that -*
2. *The occurrence of any catastrophic failure condition is extremely improbable, and cannot be caused by a single point of failure.*

The usage of Lithium-ion (Li-ion) batteries has increased significantly in recent years due to their long lifespan, high power density, and environmental benefits. However, various internal and external faults can occur during the battery operation, leading to performance issues and potentially serious consequences, such as thermal runaway, fires, or explosion [8]. The battery management systems (BMS) has led international standards to demand functional safety in electro-mobility applications, with a special focus on electric vehicles [9].In [10], it provides a Guidance for Designing Safety into UAM and eVTOL, it suggests decomposing the function at the aircraft level with associated severity classification, then performs an FHA and a Systems Theoretic Process Analysis (STPA)on an eVTOL vehicle undergoing an UAM passenger carrying reference scenario. In [11], the System Functional Hazard Assessment (SFHA) on a specific unmanned aircraft according to the ATA sections is presented and identifies 311 hazards in which 108 cases were categorized as catastrophic.

The research from NASA [12] describes the preliminary considerations for classifying hazards of unmanned aircraft systems. But very little of the research is specific to functionalities, failure conditions and classifications of eVTOL power battery systems neither the aircraft level safety mitigation approaches and effectiveness.

This manuscript comprehensively dissects the eVTOL's flight profile and delves into the impact of aircraft-level safety mitigation strategies. It

proffers a meticulously constructed hierarchical framework for eVTOL's aircraft-level functionalities. Employing a rigorous and systematic approach, it conducts a detailed Functional Hazard Analysis (FHA) with a specific focus on the power battery system, thereby elucidating potential safety lacunae inherent in the incorporation of contemporary Electric Vehicle (EV) power battery systems into the eVTOL aircraft paradigm.

III. SAFETY OBJECTIVES OF EVTOL

From a safety standpoint, severity classification for aircraft level Failure Conditions (FC) is subject to the eVTOL ConOps (concept of operation), e.g. number of passengers, travel area, flight distance and altitude, etc., aircraft level safety mitigation and implementation, and the flight profile definitions, including flight phases definition. This necessitates the execution of a comprehensive analysis of application scenarios.

3.1 State of the Art for eVTOLConOps

Numerous eVTOL ConOps studies conducted by a range of entities, including Uber [13], the Federal Aviation Administration (FAA) [14], the European Union Aviation Safety Agency (EASA) [15], NASA [16], NUAIR [17], Wisk Aero & Skyport [18] (Also known as vertiport), and others, have been published and ongoing updating. These studies have proposed business models, defined operational contexts, and outlined application scenarios with the aim of rendering urban air travel accessible to the general populace as a secure, economically viable, and pragmatic supplement and substitute for conventional modes of transportation. Almost all the application scenarios of eVTOL are targeted to Urban Air Mobility (UAM) operations, which makes better sense from business perspectives.

Besides the business aspects within all these descriptions of broad operational concepts, high-level functional capabilities and system requirements were also captured, which can be used to deduct the safety requirements for eVTOL.

Regarding for the eVTOL aircraft configuration, NASA practical concept vehicles [19] were designed with a range of potential aircraft types and propulsion system architectures, targeting at the UAM vision (six occupants at 1,200lb and 75 nm range),as illustrated in Fig. 1. These eVTOL configuration include:

- Multirotor/quadrotor aircraft, with turboshaft and electric propulsion.
- Side-by-side aircraft, with turboshaft and electric propulsion.
- Lift and cruise aircraft with electric and turbo-electric propulsion.
- Quiet single-main rotor helicopter with turboshaft and electric propulsion.
- Tiltwing aircraft with turbo-electric propulsion.

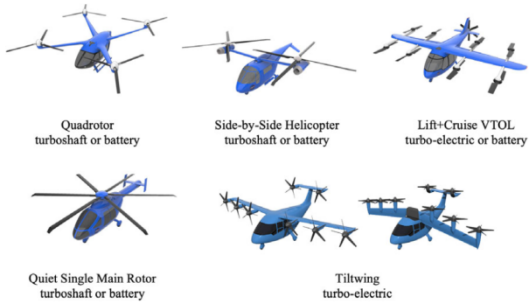

Fig. 1: Categorization of Emerging Electric Aircraft

3.2 Aircraft Level Safety Mitigation

Similar to the conventional general aviation aircraft development, meeting the safety standards mandated by certification regulations is paramount in bolstering safety measures for eVTOLs. Before delving into the safety impacts introduced by the power battery system and redundancy in propulsion, it is important to acknowledge the top-level safety mitigation effectiveness for the eVTOL aircraft configurations. What if the safety mitigations proven to be effective are deployed into an eVTOL aircraft? The following section clarified the effects of applying the crashworthiness mitigation and Ballistic Recovery Systems (BRS) in eVTOL aircraft.

3.2.1 Crashworthiness

According to 27.561 and 27.562 in the 14 FAR part 27 and part 29 for rotor wing general aviation, the aircraft should be tested to be safe for occupants

at a velocity 30 ft/sec with a peak deceleration of 30 G's and occupants must be able to evacuate themselves after the impact. These certification clauses would be most likely applicable to vast majority of eVTOL, including multirotor, Lift Plus Cruise (LPC) and tilt wing VTOL aircraft configurations. As a proof to this point, the Crashworthiness Requirements Special Condition for VTOL from EASA demands the same test conditions.

Regarding to eVTOL aircraft, the vertical movement is quite stable at a very low speed, like a free fall test. This indicates the initial height of a rough free fall movement test of eVTOL crashworthiness should be no less than 10 meters, i.e. 32 ft above ground level (AGL) attitude. Before flying higher than this height, a thorough self-check would be performed to ensure the eVTOL is in a healthy condition and suitable for further operating. This altitude can be recognized as the decision point from safety perspective for eVTOL operation during takeoff, like the speed of V1 for making Rejected Take-Off (RTO) decision for transportation aircraft.

The effectiveness of crashworthiness is a sophisticated topic various from case to case. A study from NASA presented crashworthiness design mechanisms and the implementation within a six-passenger LPC eVTOL concept vehicle, which were evaluated under multi-axis dynamic loading conditions [20]. The results of this study found the effectiveness of energy attenuating design mechanisms to be dependent on the complexity of load environment in which they were employed. An increase in off-axis loading resulted in a decrease in occupant protective capability.

3.2.2 Ballistic Rescue System

BRS is a parachute designed to be deployed in the event of an off-nominal condition for small aircraft. The BRS systems developed for Cirrus aircraft have been installed on numerous makes and models of aircraft [21]. The successful deployment of the parachute within a BRS requires enough time for inflation the canopy with minimum vertical height and/or horizontal speed as presented in Fig. 2. According to the installation and user guide from BRS suppliers [22][23], the minimum firing height of 100 ft (30 m) for canopy without slider (measured at 38mph (60km/h) in horizontal flight) and 200 ft (60 m) for canopy with slider, may not always be a safe height from which to fire the system. The eVOTL aircraft is a complex design requiring integrity of the structure, indicating the parachute with slider takes preference. It would be the common choice for a BRS with slider from safety and customers experiences perspective.

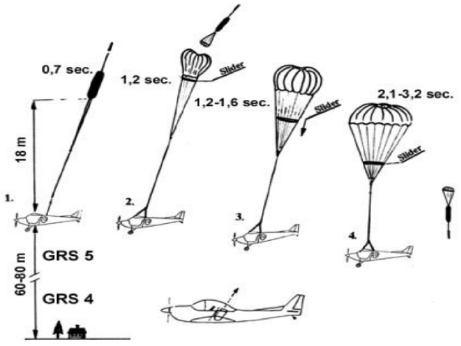

Fig. 2: Successful Deployment of BRS Parachute

In summary, the manuscript suggests a minimum firing height of 200-250 ft (60–76 m) for eVTOL BRS. Since the eVTOL aircraft is usually heavier and slower than a typical light sport aircraft (LSA) application, 250 ft (76m) should be the recommended altitude of BRS application. The BRS provides some deceleration stress even below the minimal height, it would be of 10% efficiency under 150 ft and 50 % efficiency between 150 ft and 250 ft. The also provide the protection against crash and can lower the catastrophic severity to hazardous.

3.2.3 eVTOL Flight Profile Refinement

Although the flight profile was demonstrated in the Con Ops as part of the application scenario, further clarification and refinement of quantitative parameters are needed after an effectiveness analysis from a safety perspective regarding crashworthiness and the application of Ballistic Rescue Systems (BRS), before the failure conditions assessment for each of the function.

Based on the scrutiny of crashworthiness and BRS, the altitude above ground scales in the

eVTOL flight envelop can be further clarified as following:

- The H_{BRS} is the minimal altitude of BRS full effective usage, i.e. 250 ft (76m) AGL; eVTOL would cruise above this altitude.
- The H_{rBRS} serves as an indicator of diminished BRS efficacy. Within the span of 150 feet (45 meters) to 250 feet (76 meters), the effectiveness of BRS protection experiences attenuation, during which the degree of severity can be alleviated to a lower threshold through the utilization of the BRS.
- The $H_{vertiport}$ indicates the safe area and altitude provided by the vertiport safety mitigation during the takeoff and landing periods of the eVTOL operation.
- The H_{hover} is the safe altitude of crashworthiness, namely 32 ft (10m) AGL, indicated and derived from the crashworthiness regulations. It's also the maximum altitude for performing the health check during the takeoff.
- Currently, there's no effective mitigation approach from occupant safety point of view at the height between 32 ft and 150 ft.

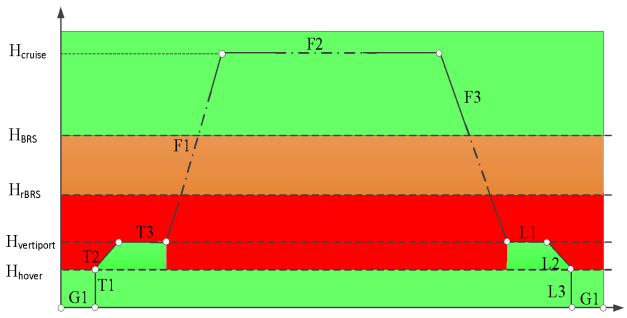

Fig. 3: eVTOL flight profile with safety mitigation

By aligning the Uber flight profile to the see VTOL altitude definitions, Fig. 3 shows the severity classification for the flight of an eVTOL with the BRS and crashworthiness mitigation designs. After aircraft level safety mitigations, the red area means no effective means to control and complement the safety impacts when failure happens, which also concludes that the top-level safety objective for eVTOL aircraft is catastrophic. The notional flight phase definition for eVTOL aircraft based on the refined flight profile and safety consideration is presented in the following table:

Table I: Flight Phase Definition for UAM

Seg	Flight phase	Safety consideration
G1	Ground Taxi	no safety impacts
T1	Hover climb	Crashworthiness implementation
T2	Transition +climb	Ground facilities(e.g. Vertiport) ensure the departure safety
T3	Departure terminal procedure	Ground facilities(e.g. Vertiport) provide the departure safety mitigation (to ensure the H_{hover} is satisfied during the departure phase)
F1	Accelerate+ climb	No safety mitigation under 150 ft which could lead to catastrophic, half efficiency at 150 ft & 250ft
F2	Cruise	BRS provides safety mitigation
F3	Decelerate + descend	No safety mitigation under 150 ft which could lead to catastrophic, half efficiency at 150 ft & 250ft
L1	Arrival terminal procedure	Ground facilities (e.g. Vertiport) provide the arrival safety mitigation
L2	Transition + descend	Ground facilities (e.g. Vertiport) provide the arrival safety mitigation
L3	Hover descend	Crashworthiness implementation
G1	Ground taxi	no safety impacts

Note: the collision and avoidance during flight related to ATM (Air Traffic Management) was not considered in this paper since it more focused on the battery management system additional to the traditional fossil energy aircraft.

IV. AIRCRAFT LEVEL FHA

At the aircraft level, the FHA examines comprehensively how the function can fail without regards to any specific implementation and/or interface.

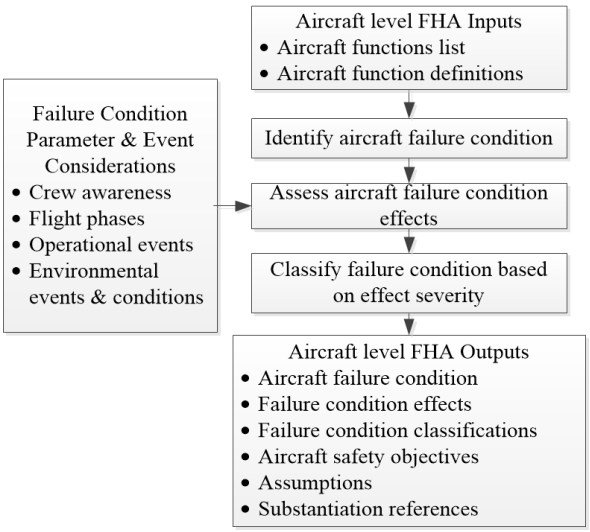

Fig. 4: AHF activities

In the realm of civil aircraft and system development, Aircraft level HFA is performed early in the development process, and to be reevaluated anytime significant changes are made to aircraft functionality. It is used to establish the safety objectives for the functions of the aircraft to achieve a safe design. The FHA process is a top-down method for examining the function list and flight phases definition, identifying failure conditions and assessing the severity of failure condition effects. A typical FHA work process is shown in Fig. 4 The assessment process consists of the following activities:

- Gather aircraft level FHA inputs.
- Review and confirm the aircraft level functions are complete.
- Determine the failure conditions associated with the aircraft functions.
- Determine the effects of each failure condition considering flight phases (elaborated in Table 1), operational and environmental conditions and events, and crew awareness.
- Assess and classify the severity of each failure condition's effects.
- Capture and confirm aircraft level FHA assumptions.

When performing the aircraft level FHA, failure conditions are analyzed for their effect on the aircraft, crew and occupants to determine the associated severity classification. Flight phase, environmental and operational conditions should be also considered during the assessment.

3.1 Aircraft Level function list

The aircraft level FHA commences with a function list at aircraft level. Much discussion has focused on how to define an appropriate list of aircraft functions for UAM. Difficulties stem from aircraft novelty, new kinds of automation, and misunderstanding of function lists. A function list focuses on what a thing (aircraft or system) must do, not what it has. This is because you cannot know how a thing may fail unless you know what it is supposed to do.

It is recognized that there is considerable variation among eVTOL aircrafts. However, a core set of functionalities that most aircraft will need to operate routinely and safely within the national airspace system are identified based on the industry standards and latest research from:

★ Conventional function definition for commercial aircraft based on the Specification for Manufacturers' Technical Data published by Air Transport Association (ATA) [26],
★ Function definition for traditional Unmanned Aircraft Systems with power battery system [27],
★ Reference studies for innovative features and relevant functions dedicated to eVTOL [28].

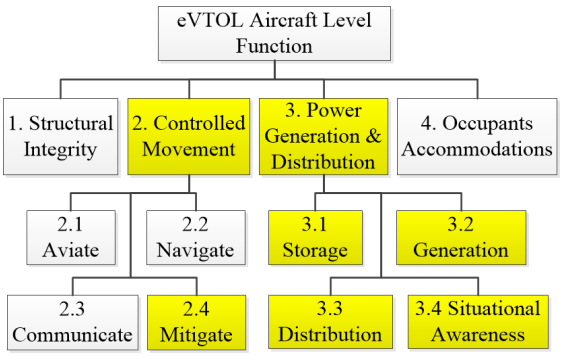

Fig. 5: eVTOL Function Decomposition at Aircraft Level

The functionality hierarchy presented herein is one of the many possible valid hierarchies. At the eVTOL aircraft level, the functionality includes providing:

1) Structural integrity.
2) Controlled movement.
3) Power generation and distribution.
4) Occupants' accommodations.

The aircraft level functions will be further broken-down into the next level as shown in Fig. 5. The "new" functionality introduced, or conventional functions impacted by the electric features of an eVTOL are highlighted in yellow in the diagram.

The core set of functions of "controlled movement" is to address the fundamental tenets of piloting; namely, to fly the plane (aviate), fly it in the right direction (navigate), and to state your condition or intentions to people inside and outside the vehicle (communicate). Finally, regarding for the operational concept of eVTOL, e.g. air mobility traffic management, detect and avoidance and the simplified vehicle operations (SVO) with artificial intelligence supports, as well as the aircraft level safety mitigation design, a fourth fundamental function was added as mitigate (as in mitigation of hazards).This function is intended to capture those actions necessary to (1)mitigate the occupant's safety by crashworthiness design and BRS design;(2) detection and avoidance; (3) provide SVO with artificial intelligence supports; (4) manage contingency situations that may arise.

Under the branch of "power generation and distribution" function, the decomposition is based on the combination of the functional definitions for Electric Vehicle power system [29] and conventional aircraft power system function definition. The aircraft level power battery system functionality consists of:

1) Storage of electric power, including battery pack for power storage; power storage interfaces, e.g. interfaces for battery charge and discharge; high-voltage protection interface against current leakage; structural protection for battery cell isolation and structural damage.
2) Generation of electric power, including the interface for transferring the electric energy to power battery storage, balancing power storage among battery cells, and protection against current leakage during the charging phase.
3) Electric power distribution provides power to the movement functions (i.e. propulsion, lift and control etc.), power discharge, balancing and protection.
4) Situational awareness provides flight crews and passengers with the indication and announcement relevant to electric power supply for normal flight operation and safety mitigation and provides the thermal management and maintains the battery health and capacity status.

The breakdowns of the functions of "provide controlled movement" and "provide power generation and distribution" are shown in the following Fig. 6 and Fig. 7.

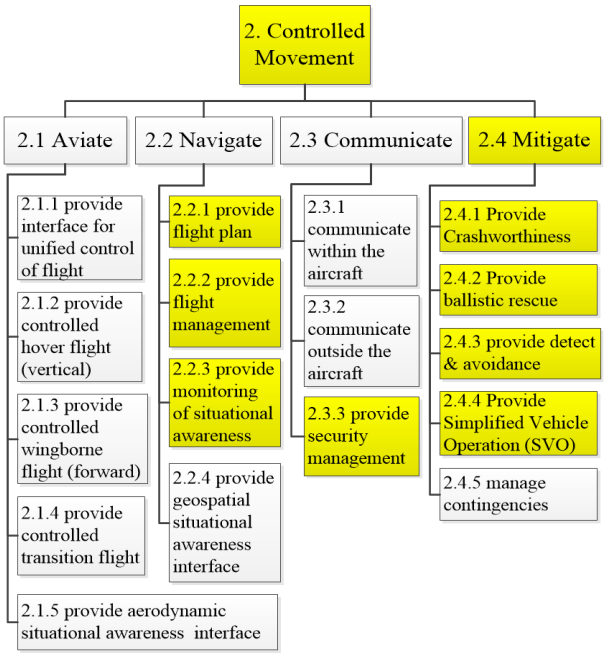

Fig. 6: eVTOL Function Decomposition for "Controlled Movement"

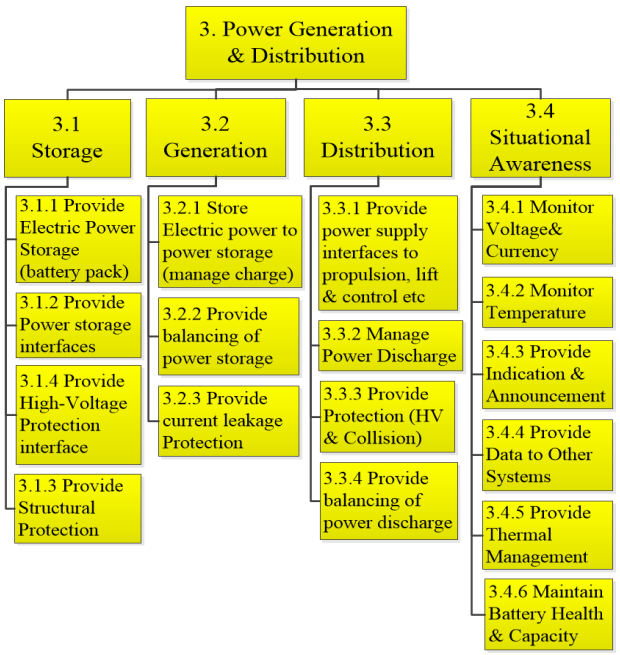

Fig. 7: eVTOL Function Decomposition for "Power Generation & Distribution"

4.2 aircraft level failure conditions

Failure conditions describe a failed state of the aircraft function including the amount and type of impairment. Knowledge of each function is necessary to properly define failure conditions which are correct in the context of the aircraft function, operation, and environment. Failure conditions in the FHA are broadly stated to provide a scope which encompasses all detailed failure scenarios that can lead to the top-level functional effect.

A failure condition is described by a statement that characterizes an abnormal state of a function. Failure conditions can be broadly categorized as the loss of a function or as a malfunction. Each function should be assessed and the potential for loss of the function and malfunction considered. In general, each aircraft function will have at least one loss of function and one malfunction of interest. Basic categories of function failure include:

4.2.1 Loss of the Function

Loss of function may be total or partial. Total loss of function is a condition where the function cannot be performed by any means. Partial losses of function are conditions where the function can still be performed but only at reduced effectiveness, with increased difficulty or by means other than the normal means used to accomplish it.

4.2.2 Malfunction

Malfunction is a condition where the operation of a function is different than intended excluding function loss. The aspect of the function which is incorrectly performed is described in the failure condition (e. g., erroneous, un-commanded/ inadvertent action, misleading).

As an example of the deployment of the function failure condition analysis, the failure condition for the innovative eVTOL functions under "Provide Communication" are listed in the following table.

Table 2: Aircraft Level Function Failure Condition Matrix (Example)

ID#	Aircraft Function	Total loss	Partial loss	Mal-function
2 Provide Controlled Movement				
2.3 Provide Communication				
2.3.1	Provide Security Management	2.3.1. TL Loss of the ability for security protection	2.3.1. PL Partial loss of the ability for security protection	2.3.1. MF1 Overprotection or mistakes during security protection
2.4 Provide Mitigation of Hazards				
2.4.1	Provide Crashworthiness	2.4.1. TL Loss of the ability for occupant protect	2.4.1. PL Partial Loss of the ability for occupant protect	NA
2.4.2	Provide Ballistic Recue	2.4.1. TL Loss of the ability for occupant protect	2.4.1. PL Partial Loss of the ability for occupant protect	2.4.1. MF1 un-commanded deployment of parachute 2.4.1. MF2 fail to deploy parachute (contribute to Loss)
2.4.3	Provide detect and avoidance	2.4.3. TL Loss of the ability for detection and avoidance	2.4.3. TL Partial Loss of the ability for detection and avoidance	2.4.3. MF1 fail to detect & report dangers. 2.4.3. MF2 report dangers by mistake
3 Provide Power Generation & Distribution				
3.1 Provide Power Storage				
3.2 Provide Power Generation				
3.3 Provide Power Distribution				
3.4 Provide Situational Awareness				

The same approach applies to the "Power Generation & Distribution" function, and the relevant failure conditions identified under total loss, partial loss and malfunction are summarized as following:

- Total loss
  - 3.1. TL1 Total loss of power
  - 3.2. TL Thermal runaway
  - 3.1. TL2 Current leakage
  - 3.4. TL Total loss of power information
- Partial loss
  - 3.1. PL Asymmetric loss of power
  - 3.2. PL Thermal runaway
  - 3.3. PL Current leakage
  - 3.4. PL Partial loss of power information
- Malfunction
  - 3.3. MF1 Inadvertent power off
  - 3.3. MF2 Un-commended power supply
  - 3.2. MF1 Current leakage
  - 3.2. MF2 Thermal runaway
  - 3.4. MF1 Erroneous power supply information without announcement to the flight crew

4.3 Aircraft Level FHA

The effects are captured based on their immediate effect on aircraft, flight crew and occupants during the phase of flight being analyzed. The qualitative classification of the failure conditions is listed in the following table 3.

Table 3: Failure Condition Classifications of eVTOL

Class	Aircraft	Crew	Occupants
CAT	Normally with hull loss	Fatal injury or incapacitation	Multiple fatalities
HAZ	Large reduction in functional capabilities or safety margins	Physical distress or excessive workload impairs ability to perform tasks	Serious or fatal injury to an occupant
MAJ	Significant reduction in functional capabilities or safety margins	Physical discomfort or a significant increase in workload	Physical distress to passengers, possibly including injuries
MIN	Slight reduction in functional capabilities or safety margins	Slight increase in workload or use of emergency procedures	No effect on flight crew
No-Effect	Inconvenience for passengers	No effect on flight crew	No effect on operational capabilities or safety

The allowable quantitative probability requirement for each of the classification are identified in the ASTM document (F3230-17 [30],Table 5).The quantitative objective for each classification is listed as following:

★ CAT (Catastrophic),$<10^{-7}$ per flight hour;
★ HAZ (Hazardous),$<10^{-6}$ per flight hour;
★ MAJ (Major),$<10^{-5}$ per flight hour;
★ MIN (Minor),$<10^{-3}$ per flight hour;
★ No-Effect, No Probability Requirement

It is recognized that when designing civil aircraft systems, the manufacturers should prevent any single failure that leads to a catastrophic failure condition in air transportation, General Aviation and eVTOL aircraft.

The detailed aircraft level FHA for battery system is in Table 4.

Table 4: Aircraft FHA for Electric Power Generation & Production

FC. No.	FC Description	Flight Phase	Effect of FC on: A. Aircraft B. Crew C. Occupants	FC Class.	Remarks/Justification
3.1.TL1	Total loss of power	F1, F3	A. Airplane unable to provide continued safe flight along desired flight path. Airplane impact with ground or surroundings resulting in significant airplane damage or hull loss. B. Flight crew unable to maintain desired flight path. Flight Crew fatalities. C. Passenger fatalities.	CAT	During the flight phase of F1 and F3 between the H_{hover} and H_{rBRS}, BRS and crashworthiness cannot provide effective safety mitigations
3.2.TL 3.2.PL 3.2.ML2	Thermal runaway	all phase	A. Aircraft burst into fire. Airplane unable to provide continued safe operation. Airplane impact with ground or surroundings resulting in	CAT	Battery thermal runaway causes fire or even explosion at any flight phase, leaving little time to respond

			significant airplane damage or hull loss. B. Flight crew unable to control aircraft. Flight Crew fatalities. C. Passenger fatalities.		
3.1.TL2 3.2.PL 3.2.ML1	Current leakage of high-voltage battery	all phase	A. Airplane unable to provide operation. Large reduction in safety margin. B. Crew experiences excessive workload to control direction resulting inability to perform required tasks. C. Potential injury or death to some of the passengers.	CAT	Current leakage from high-voltage causes crew to lose consciousness
3.4.TL 3.4.PL	Total loss of power information	T1, T2, T3, F1, F3, L1, L2 ,L3	A. Airplane unable to provide power information. Large reduction in safety margin. B. Crew experiences excessive workload to compensate. C. No effect	MAJ	Trigger emergency landing procedure when crew identify the total loss of power information
3.1.PL	Asymmetric loss of power (partial loss)	T2, T3, F1, F3, L1, L2	A. Airplane unable to provide continued safe flight along desired flight path. Airplane impact with ground or surroundings resulting in significant airplane damage or hull loss. B. Flight crew unable to maintain desired flight path. Flight Crew fatalities. C. Passenger fatalities.	CAT	
3.3.ML1	Inadvertent power off	F1, F3	A. Airplane unable to provide continued safe flight along desired flight path. Airplane impact with ground or surroundings resulting in significant airplane damage or hull loss. B. Flight crew unable to maintain desired flight path. Flight Crew fatalities.	CAT	

			C. Passenger fatalities.		
3.3.ML2	Un-commended/uncontrolled power supply	T2, T3, F1, F3, L1, L2	A. Airplane unstable along desired flight path. Excessive power supply causes unstable flight. B. Pilot able to maintain control using reduce electric motor rpms on failed wingtip. Pilot adjusts lift on other rotors for immediate landing. C. Passenger experience discomfort	HAZ	Assumption: that this level of manual control is available to the pilot, and they are sufficiently trained to detect and respond to this hazard.
3.4.ML1	Erroneous power supply information without announcement to the flight crew	T2, T3, F1, F3, L1, L2	A. Airplane unable to provide continued safe flight along desired flight path. Airplane impact with ground or surroundings resulting in significant airplane damage or hull loss. B. Flight crew unable to maintain desired flight path. Flight Crew fatalities. C. Passenger fatalities.	CAT	Misleading to the flight crew

The function of electric power storage, generation, distribution and situational awareness functions under "power generation and distribution" are identified to be of CAT class according to the failure conditions, including:

1) Total loss of power when flying across the height of without effective BRS and crashworthiness mitigations.
2) Thermal runaway through all flight phases (even on ground) especially without warning information as undetected failures.
3) Current leakage of high-voltage battery causes crew to lose consciousness.
4) Asymmetric loss of power causes uncontrollable movements due to partial loss of power supply.
5) Inadvertent power off during flight due to un-commended action or data error on the data bus;
6) Erroneous power supply information without announcement to the flight crew (misleading)

3.4 Allocate Aircraft Functions to Systems

The system architecture establishes the structure and boundaries within which specific item designs are implemented to meet the functional requirements and safety objectives. More than one candidate system architecture may be considered for implementation. These candidate system architectures may be evaluated using such factors as technology readiness, implementation schedules, producibility, contractual obligations, economics, prior experience and industry precedence. Aiming to a LPC eVTOL configuration and architecture, the function allocation is conducted as shown in Fig. 8.

The highlighted boxes in yellow are those impacted by the innovative feature, power battery system.

★ The power storage, generation, distribution and situational awareness function are allocated to the "aircraft battery system" and "flight and propulsion control electronics".

★ The innovative functionality of eVTOL, including SVO and security protection, is implemented by flight deck and annunciations / function controls as hosted applications.
★ Detection & avoidance, BRS and crashworthiness protection are allocated to standalone systems additional to traditional GA avionics system.

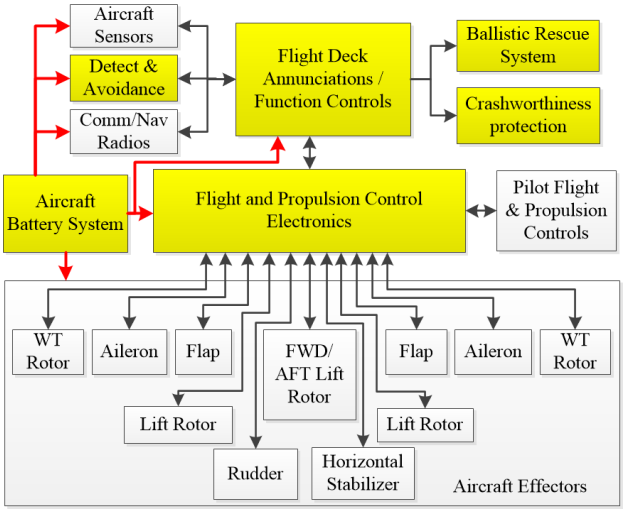

Fig. 8: eVTOL Aircraft Level Architecture

During the function allocation process, the independence among systems should be considered to ensure a fail-safe design. The fail-safe concept and techniques are discussed in the AMJ/AC 25.1309-1A to support this approach. ASTM F3230 [30] section 4.2.4.3 prescribes that "no catastrophic failure condition should result from failure of a single component, part or element of a system." Even for eVTOL, the common-mode failure analysis should be performed to ensure that failures of the low-confidence function do not result in failures of the overall protected function.

V. PRELIMINARY SAFETY CONSIDERATIONS FOR ONBOARD POWER BATTERY SYSTEM

After the identification of system functionality and boundary, the system requirements will be further allocated to items within the system. In practice, system architecture development and the allocation of system requirements to item requirements are tightly coupled, iterative processes. The process is complete when all requirements can be accommodated within the final architecture. The decomposition and allocation of requirements to items should also ensure that the item can be shown to fully implement the allocated requirements. When comes to the VTOL power battery system, the pragmatic candidate architecture design and items implementation is from the extant EV battery solution.

While it is evident that there is room for further enhancement in the performance of EV battery systems for eVTOL usage, particularly in aspects such as energy density, it remains unquestionable that the current EV battery systems unequivocally offer capabilities encompassing electric power storage, generation, distribution, and situational awareness, thereby supporting the operational requirements of eVTOL aircraft for commercial purposes in the future.

5.1 Battery System Architecture Context

The Fig. 9 presents a typical electric powertrain structure for a eVTOL aircraft. The primary origin of propulsion for lift and cruise is the traction propellers, which derives its power from an electric battery. This battery system operates in two fundamental modes: charging and discharging. During the discharge phase, it transforms electrical energy into propulsive force through the electric motor and gearbox assembly. The mechanical transmission subsequently conveys this rotational energy to the aircraft's propeller with support from flight and propulsion control electronics, flight deck annunciation and function controls, as well as other aircraft systems. All these systems and interfaces establishes the context of the onboard power battery system highlighted in yellow.

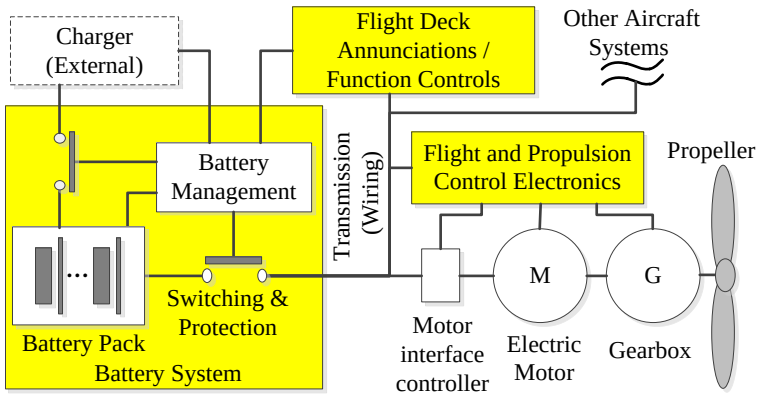

Fig. 9: Airplane Level Basic Function

The eVTOL battery system predominantly relies upon an established EV battery solution. The EV battery system attains automotive-grade performance and reliability through the incorporation of a laminated structure that enhances cooling efficiency and a robust battery management system that ensures consistent performance. Moreover, the design of the battery system, encompassing battery packs, modules, and cells, is strategically engineered to serve as protective safeguards against potential hazards from mechanical, electrical, and thermal perspectives [31].

The typical EV battery system consists of 3 major subsystems, including Battery Pack, Battery Management and Switching & Protection described as following:

5.1.1 BP - Battery Pack

Battery pack contains the battery modules and cells, provides the electrical energy storage capability with stable performance and reliable service. The battery pack also satisfies the remaining onboard requirements, such as environment, vibration and shock, etc.

5.1.2 SP - Switching & Protection

Switching & Protection consists of the relays, fuses for high voltage protection and the high-strength framing and packaging structure for installation and protection. The cockpit and cabin are structurally separated from high-voltage electric system during physical and electrical interface design.

The battery system case is made from steel to create a sealed structure, and the battery pack uses a robust interior of metal fixtures to secure components, which helps maintain the pack structure in case of accident or fire.

The main relay initially keeps high voltage circuit open and is activated only when control system is correct. The main relay is cut off when detecting vehicle crash. The relays work collaboratively "switching" from charging mode to discharging mode.

Fuses are deployed in the battery pack and modules to prevent high-voltage electric leakage.

5.1.3 BMS - Battery Management System

BMS performs continuous self-diagnostics by monitoring individual cell voltage, state of charge, battery temperature, battery pack hardware conditions etc. BMS optimizes conditions to provide power on demand. BMS responds to unexpected conditions by going to failsafe mode or complete shutdown depending on the circumstances; e.g. overcharging, over-temp, cell failure and crash.

5.2 Battery System FDAL allocation

The Functional Development Assurance Level (FDAL) for each of the battery system functionality are listed in the following Table 5, including the results for mapping of the function into the existing EV battery subsystems.

Table 5: FDAL for eVTOL battery System Functions

ID#	Function	FDAL	BP	BMS	SP
3.1	Storage				
3.1.1	Power Storage	B[1]	X		
3.1.2	storage interfaces	B	X		
3.1.3	high-voltage Protection interface	B			X
3.1.4	Structural Protection	B	X		
3.2	Generation				
3.2.1	manage charge	B		X	
3.2.2	Balancing charge	A		X	
3.2.3	leakage Protection management	A		X	
3.3.	Distribution				
3.3.1	power supply interfaces	A		X[2]	X[2]
3.3.2	manage discharge	A		X	
3.3.3	provide protection	B		X	
3.3.4	balancing discharge	A		X	
3.4	Situational Awareness				
3.4.1	monitor voltage & current	A		X	
3.4.2	monitor temperature	A	X[3]		
3.4.3	provide indication & announcement	A		X	
3.4.4	provide data to other systems	A		X	
3.4.5	provide thermal management	A		X	
3.4.6	Maintain battery health & capacity	B		X	

Notes: *1: the loss of power storage itself will not cause CAT, unless combined with undetected error before the flight which is misleading to the flight crew.
*2: allocate to both subsystems to ensure an independent functional design to prevent the "inadvertent power off" event.
*3: if the temperature monitor (including both software and hardware) is allocated to be part of the battery package, so all the BP will have to be developed to a DALA compliance system, which brings unnecessary cost and complexity of the BP design. It would be recommended that keep the temperature sensor simple and allocate it to the BP, while reallocate the temperature monitor related software and hardware items to BM

According to the FDAL allocation, most of the FDAL A functions are allocated to Battery Management System, other than "provide monitor temperature" and "provide power supply interfaces to propulsion". The temperature monitor sensors and interfaces are implemented within the battery pack according to the current EV design, and the power supply interface is implemented by switching relays. The safety considerations and mitigation are as following:

1. Electric power supply interface could lead to an inadvertent power off without independent monitoring function to oversight the validation of a "power off" switch command. The "monitor" to validate the power off command for power supply interface could be implemented as part of the battery management subsystem. According to the rational for FDAL allocation in ARP 4754A, Since the BMS is a DAL A function, the DAL level of "switching & protection" function to remain as a DAL-B (and even lower) function.
2. The temperature sensors and interfaces could cause both loss and misleading for the temperature monitor function, and subsequently toa thermal runaway event. It

would be recommended to keep the temperature sensor simple and, in the BP, while reallocate the temperature monitoring and processing software and hardware function into BMS.

3. Further safety mitigation approach could be performed to review and update the design of the battery management function and subsystem to mitigate the safety impact at the system design level.

If the temperature processing hardware and software are implemented by BMS, both the battery pack and switching & protection consists of only simple electric and mechanical parts, which can be recognized as non-complex system. According to the pragmatic practices from civil aircraft and system development, the non-complex items may be considered as meeting IDAL A rigor when they are fully assured by a combination of testing and analysis, however requirements for these items should be validated with the rigor corresponding to the FDAL of the function [4].

BMS is a typical complex system embracing both electronic hardware and embedded software. It is definitely subjected to the development assurance process with the appropriated confident level of rigor to identify and correct development errors.

5.3 Development Rigor

Due to the highly complex and integrated nature of modern aircraft systems, the regulatory and industry standards have highlighted concerns about the possibility of development errors causing or contributing to aircraft Failure Conditions. Briefly speaking, a developer might introduce development errors (mistakes in requirements determination, design or implementation) which potentially cause a fault that might result in a failure. It is required to have the planned and systematic tasks used to substantiate, to an adequate level of confidence, that development errors have been identified and corrected such that the items satisfy a defined set of requirements. Therefore, a process is needed, which establishes levels of confidence that development errors that can cause or contribute to identified Failure Conditions have been minimized with an appropriate level of rigor.

The aeronautic standard ARP 4754A[4] on the other hand is highly regulated, compliance depends on government or surrogate approval, must be uniform for a class of equipment and is effectively mandatory. The automotive standard (ISO 26262) [32] is industry-driven, compliance depends on 3rd party accreditation through the supply chain, allows for different level of compliance depending on context and compliance is voluntary, at least in principle. The ISO 26262 series of standards is the adaptation of IEC 61508 [33] series of standards to address the sector specific needs of electrical and/or electronic (E/E) systems within road vehicles, and it is intended to ensure the absence of unreasonable risk due to hazards caused by malfunctioning behavior of E/E systems. The only comparable artefact of ARP 4754A to IEC 61508 / ISO 26262 Systematic Capability is the concept of Item Development Assurance Level (IDAL).

Both aviation best practice recommendation and automobile standards have the similar definition and rational to address the development error with the level of rigor that the development assurance tasks performed to.

5.3.1 Rigor Modulation Definitions

a) Civil aviation definition in ARP 4754A [4]

Error: An omitted or incorrect action by a crewmember or maintenance person, or a mistake in requirements, design, or implementation (derived from AMC 25.1309).

Development Error: A mistake in requirements determination, design or implementation.

Development Assurance: All of those planned and systematic actions used to substantiate, at an adequate level of confidence, that errors in requirements, design and implementation have been identified and corrected such that the system satisfies the applicable certification basis.

Function Development Assurance Level (FDAL): The level of rigor of development assurance tasks performed to Functions. [Note: The FDAL is used to identify the ARP4754 /ED-79 objectives that need to be satisfied for the aircraft/system functions].

Item Development Assurance Level (IDAL): The level of rigor of development assurance tasks performed on Item(s). [e.g. IDAL is the appropriate Software Level in DO-178B/ED-12B, and design assurance level in DO-254/ED-80 objectives that need to be satisfied for an item].

Fault: A manifestation of an error in an item or system that may lead to a failure.

Failure: An occurrence which affects the operation of a component, part or element such that it can no longer function as intended, (this includes both loss of function and malfunction). Note: errors may cause Failures but are not considered to be Failures.

b) Automobile definition in ISO26262 [32]

Error: discrepancy between a computed, observed or measured value or condition, and the true, specified or theoretically correct value or condition. Note: An error can arise because of a fault within the system or component being considered.

Automotive Safety Integrity Level (ASIL): one of four levels to specify the item's or element's necessary ISO 26262 requirements and safety measures to apply for avoiding an unreasonable risk, with D representing the most stringent and A the least stringent level.

Fault: abnormal condition that can cause an element or an item to fail.
Failure: termination of an intended behavior of an element or an item due to a fault manifestation.

At the system level, the FDAL concept in ARP 4754A addresses the management of systematic faults (development errors). From the FDAL, it is possible to define the requirements that will build the requested confidence level. In civil aviation, the Functional Development Assurance Level (FDAL) and Item Development Assurance Level is assigned to systems and items through Level A ~ E, in which level A means rigorist level. The development assurance level is purely subjected to the severity as a quantitative analysis result.

In the automobile, Automotive System Integrity Level (ASIL) is identified by Level A ~ D, in which Level D indicates the most serious development assurance confidence. The process for ASIL generation is presented in Fig. 10, which is a subjected to quantified Risk, the production of Severity, Exposure (probability)and Controllability. The controllability factor to be considered during functional safety assessment is additional to ARP 4754A approaches.

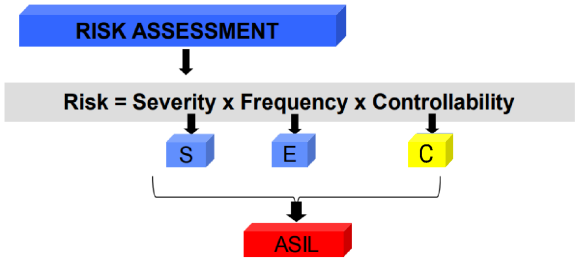

Fig. 10: ASIL, Automotive Safety Integrity Level

It includes only the satisfaction of generic objectives on the development processes. Compared to Systematic Capability, the IDAL lists few aspects of the item which could be interpreted as technical or functional requirements [35].

5.3.2 Hardware Development Rigor

Regarding for the electronic hardware development assurance indicated from IDAL defined in DO-254, there are differences in terminology which can be confusing, particularly with respect to safety levels. There are also differences in scope (ISO 26262 is primarily about safety whereas DO-254 covers a broader range of requirements), how reliability is treated (the ISO standard is more explicit here), handling validation out of context (again ISO is better here) and personnel requirements (ISO requires identified staff with training/certification) [36].

5.3.3 Software Development Rigor

When mapping the automobile software development processes defined in ISO26262 to the software certification objectives defined in DO-178B/C, a lot of gaps are identified for the integral process and certification liaison besides the basic software development activities, e.g. architecture design, coding and test etc. Detailed comparison is exhibited in Fig. 11 in the sequences of Planning, Requirements, Design, Coding, Integration and Test etc., and gaps are highlighted in yellow and red, including:

1) All Stage of Involvement (SOI) reviews and certification liaison are missed, which are mandatory for airworthiness audits and approvals.
2) Lack of the airworthiness certification plans, including certification and processes assurance plans which is required for mitigating development errors during software development.
3) The safety related requirements validation and safety assessments for derived software requirements are not required in automobile industry.
4) Lack of one level of requirements. Besides the High-Level Requirements (HLR), the Low-Level Requirements (LLR) is required for DO-178B compliance while automobile have only 1 level of the requirements.
5) The ISO26262 software development could partially match,
   a) Plans for development, configuration managements, verification.
   b) Standards for requirements, coding and design.
   c) HLR development and attributes, coverage and traceability

It can be concluded from the process gap case study, that the existing software product developed compliance to the ISO26262 will not satisfy the rigor required by DO-178B/C is applicable to civil aviation airborne software development.

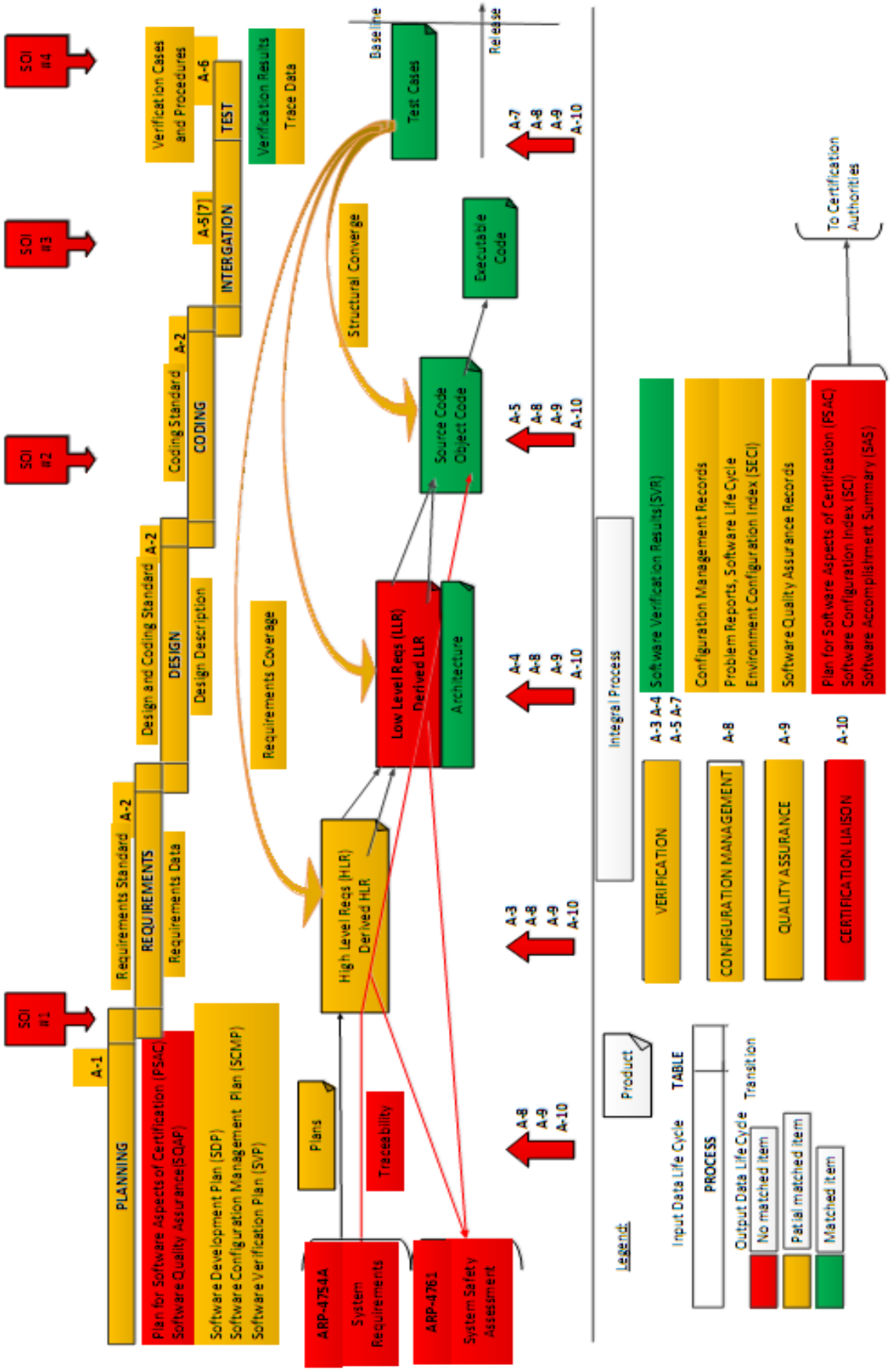

Fig. 11: Process Gap Case Study: Software Development Processes defined in DO-178 and ISO2626

IV. CONCLUSION

Even with the incorporation of well-established safety mitigation measures, specifically crashworthiness and BRS mitigations, into eVTOL aircraft, complete elimination of catastrophic failure conditions remains unattainable. Nevertheless, the analysis of safety measures at the aircraft level aids in the identification and refinement of overarching safety objectives and operational preferences.

A completeness and correctness oriented functional hierarchy of eVTOL is proposed as the foundation to proceed the FHA assessment process and the function allocation during the aircraft design phase. Leveraging the existing EV battery solutions, the aircraft power battery functionality is further decomposed and allocated into the battery systems, thereby establishing the severity classifications that defines the safety objectives for eVTOL.

To ensure compliance with airworthiness regulations, it is essential to acknowledge that no single failure or software/AEH error should lead to a Catastrophic Failure Condition. This mandate necessitates a fail-safe design for all eVTOL aircraft systems. Potential vulnerabilities and gaps associated with the application of the EV battery solution in eVTOLs encompass total power loss, thermal runaway, asymmetric power loss (partial loss), inadvertent power off, high-voltage current leakage, and the potential for misleading power supply information.

Aviation industry standards were established earlier and independently from the safety considerations for Electronics/Electric systems and programmatic components IEC 61508, leading to ISO 26262 norms as a specific instance in automobile industry. The only comparable artefact of ARP 4754A to IEC 61508 / ISO 26262 Systematic Capability is the concept of Item Development Assurance Level (IDAL). It is imperative to underscore that aviation places a significantly greater and more intricate emphasis on safety considerations, encompassing software development and hardware integrity, when compared to the automotive domain. Additional attention should be paid to the FDAL allocation, system level development and safety assess process to be able to show compliance to the certification regulatory when adapting the EV battery products into eVTOL application.

The revolutionary potential of eVTOL technology to reshape our lives may remain dormant until we conquer all technical barriers and effectively address safety concerns and risks to gain public acceptance. From a business and program perspective, the strategic reuse of EV battery products during eVTOL development stands to offer substantial advantages in terms of cost and scheduling. However, it may inadvertently deviate from the fail-safe design objective, especially regarding preventing single failures or errors from triggering catastrophic failure conditions. Such deviations have the potential to introduce significant alterations and delays in the quest for airworthiness certification approvals.

Designers of eVTOL aircraft should maintain a heightened awareness of the pronounced disparities not only in functionality, interface, and performance but also in the development rigor between the aviation and automotive sectors. These disparities can have significant repercussions on both design and supply chain management. Consequently, during the development of an eVTOL aircraft, a system engineering approach and a top-down design process should be rigorously adhered to, with the aim of capturing every opportunity to leverage and improve the contemporary power battery products.

ACKNOWLEDGMENT

The research presented in this work has been supported by AVIAGE SYSTEMS. At the core of its civil avionic system solutions, AVIAGE SYSTEMS' industry leading IMA (Integrated Modular Avionics) technology provides an expandable, easily configurable, digital open-architecture computing platform, capable of hosting more functions, improving integration ability, and effectively saving operation cost. A professional chief engineering team, covering safety & RMT (Reliability, Maintainability, Testability), airworthiness certification, design quality assurance and system engineering, were

established during the C919 IMA complex system design, development and certification process, expending the expertise to serve for other domains. A shorter version of this work was presented as invited keynote speech during AOPA (Aircraft Owners and Pilots Association) 1st International Forum on UAM and eVTOL (Changsha, Hunan, China, Sep 2022), SAE (Society of Automotive Engineers) Intelligent Urban Air Mobility Symposium (Shanghai, China, Oct 2022).

Nomenclature

ATA	Air Transport Association
AEH	Airborne Electronic Hardware
AGL	Above Ground Level
ASIL	Automotive Safety Integrity Level
ATM	Air Traffic Management
BMS	Battery Management Systems
BRS	Ballistic Rescue System
CAT	Catastrophic
ConOps	Concept of Operation
DAL	Development Assurance Level
EASA	European Union Aviation Safety Agency
E/E	Electrical and/or Electronic
EV	Electric Vehicle
eVTOL	electric Vertical Take Off and Landing
FDAL	Functional Development Assurance Level
FAA	Federal Aviation Administration
FC	Failure Condition
FC&C	Failure Condition & Classification
FHA	Functional Hazard Assessment
HAZ	Hazardous
HLR	High-Level Requirements
IDAL	Item Development Assurance Level
LLR	Low-Level Requirements
LPC	Lift Plus Cruise
LSA	Light Sport Aircraft
MAJ	Major
MF	Mal-Function
MIN	Minor
PL	Partial Loss
RTO	Rejected Take-Off
STPA	Systems Theoretic Process Analysis
SVO	Simplified vehicle operations
TL	Total Loss
UAM	Urban Air Mobility

REFERENCE

1. UmutDurak, Jürgen Becker, Sven Hartmann, Nikolaos S. Voros. Advances in Aeronautical Informatics [B]. ISBN 978-3-319-75057-6, Springer, Switzerland. 2018.
2. SAE. ARP 4754 - Certification Considerations for Highly Integrated or Complex Aircraft Systems. (1996).
3. AC 25.1309-1, System Safety Analysis and Assessment for Part 25 Airplanes. FAA, 1982
4. SAE ARP 4754A, Guidelines for Development of Civil Aircraft and Systems, December 2010.
5. SAE ARP 4761, Guidelines and Methods for Conducting the Safety Assessment Process on Civil Airborne Systems and Equipment, December 1996.
6. Federal Aviation Administration. Airworthiness Criteria: Special Class Airworthiness Criteria for the Joby Aero, Inc. Model JAS4-1 Powered-Lift. 11/08/2022. https://www.federalregister.gov/documents/2022/11/08/2022-23962/airworthiness-criteria-special-class-airworthiness-criteria-for-the-joby-aero-inc-model-jas4-1, accessed by 2023/4/23.
7. Civil Aviation Administration of China. Special conditions for the EH216-S unmanned aerial vehicle system. 2022-02-09. http://www.caac.gov.cn/XXGK/XXGK/BZGF/ZYTJHHM/202202/t20220222_211914.html, accessed by 2023/4/23.
8. Tran, M.-K.; Fowler, M. A Review of Lithium-Ion Battery Fault Diagnostic Algorithms: Current Progress and Future Challenges. Algorithms 2020, 13, 62. https://doi.org/10.3390/a13030062.
9. Marcos, D.; Garmendia, M.; Crego, J.; Cortajarena, J.A. Functional Safety BMS Design Methodology for Automotive Lithium-Based Batteries. Energies 2021, 14, 6942. https://doi.org/10.3390/en14216942
10. Mallory S. Graydon, Natasha A. Neogi. Guidance for Designing Safety into Urban AirMobility: Hazard Analysis Techniques. AIAA Scitech 2020 Forum, Orlando, FL, 5 Jan 2020.
11. Intan Novhela. The Mitigation Design of Failure Conditions Level System with System Functional Hazard Assessment (SFHA) on Unmanned Aircraft MALE Class [J]. Scientific Research Journal (SCIRJ), Volume VIII, Issue XII, December 2020.
12. Hayhurst KJ, Maddalon JM, Miner PS, Szatkowski GN, Ulrey ML, Dewalt MP, Spitzer CR (2007). Preliminary considerations for classifying hazards of unmanned aircraft

systems. Tech. Rep. NASA TM-2007-214539, National Aeronautics and Space Administration, Langley Research Center, Hampton, Virginia.
13. Holden, Jeff and Nikhil Goel. Fast-Forwarding to a Future of On-Demand Urban Air Transportation. UBER. October 27, 2016. https:// www.uber.com/elevate.pdf, accessed July 22, 2020.
14. Federal Aviation Administration. (2020). Urban Air Mobility (UAM) Concept of Operations v1.0.Washington, DC: Federal Aviation Administration
15. EUROCAE. ED-278 - Concept of Operations for VTOL Aircraf. September 1, 2020
16. NASA. UAM Vision Concept of Operations (ConOps) UAM Maturity Level (UML) 4 Version 1.0. 2021-2-22. UAM conops v1.0
17. HIGH-DENSITY AUTOMATED VERTIPORT CONCEPT OF OPERATIONS. Northeast UAS Airspace Integration Research Alliance, Inc. (NUAIR), Newyork, USA. 2021.
18. Concept of Operations: Autonomous UAM Aircraft Operations and Vertiport Integration. Wisk Aero co., (CA, USA) & Skyport (London, UK). 2022-4-12.
19. W. Johnson and C. Silva. NASA concept vehicles and the engineering of advanced air mobility aircraft[J]. The Aeronautical Journal (2021).
20. Jacob Putnam, Justin Littell. Crashworthiness of a Lift plus Cruise eVTOL Vehicle Design within Dynamic Loading Environments. Vertical Flight Society's 76th Annual Forum & Technology Display, Montreal, Quebec, Canada, May 19-21, 2020.
21. Justin Littell. Challenges in Vehicle Safety and Occupant Protection for Autonomous electric Vertical Take-off and Landing (eVTOL) Vehicles. AIAA/IEEE Electric Aircraft Technologies Symposium, Indianapolis, IN, August 22, 2019.
22. Cirrus Aircraft. Guide to the Cirrus Airframe Parachute System (CAPS). https:// cirrusaircraft.com/wp-content/uploads/2014/12/CAPS_Guide.pdf. Accessed April 19, 2019.
23. Galaxy GRS. Instruction Manual for Assembly and Use of Ballistic Parachute Rescue System. Liberec, Czech Republic, 04/2016
24. Gerardo Olivares. Integrated Safety for eVTOL Crashworthiness: From Conceptual Design to Certification. NASA-FAA eVTOL Crashworthiness Workshop #4, April 13, 2021.
25. Mackenzie Krumme. Oshkosh lands nation's first flying car terminal. https://www.wpr.org/oshkosh-lands-nations-first-flying-car-terminal. Accessed by May 18, 2022.
26. Scott Jackson. System Engineering for Commercial Aircraft. INCOSE International Symposium. 1997.
27. Kelly J. Hayhurst, Jeffrey M. Maddalon, Paul S. Miner. Preliminary Considerations for Classifying Hazards of Unmanned Aircraft Systems. National Aeronautics andSpace Administration. 2007, 2.
28. Michael DeVore, Jared Cooper, Andy Wallington, Robert Crouse, Gust Tsikalas, Komal Verma etc. Run Time Assurance for Electric Vertical Takeoff and Landing Aircraft. NASA/CR-20210026909, March 2022.
29. Gabbar,H.A.;Othman, A.M.; Abdussami, M.R. Review of Battery Management Systems (BMS) Development and Industrial Standards. Technologies 2021, 9, 28. https://doi.org/10.3390/ technologies9020028.
30. ASTM F3230-17 Standard Practice for Safety Assessment of Systems and Equipment in Small Aircraft, March 2017
31. NISSAN MOTOR Co., ltd. EV/HEV Safety. [EB]. https://www.nhtsa.gov/sites/nhtsa.gov/files/nissan_presentation-bob_yakushi.pptx, accessed by 2023/9/3.
32. INTERNATIONAL ISO STANDARD 26262-1. Road vehicles — Functional safety — Part 1: Vocabulary. Second edition 2018-12.
33. 2010, IEC, IEC 61508 "Functional safety of electrical/electronic/ programmable electronic safety- related systems, edition 2.
34. Bertrand Ricque, Philippe Baufreton, Jean-Paul Blanquart, Jean-Louis Boulanger. A cross-domain comparison of systematic errors control strategies. hal-02066561, HAL. https://hal.science/hal-02066561/document, accessed by 2023/9/11.
35. Bernard Murphy. Conflating ISO 26262 and DO-254[EB]. https://semiwiki.com/eda/aldec/7262-conflating-iso-26262-and-do-254/, accessed by 2023/9/11.

Hydromorphological Modeling of Vertical Grain Sorting Process. Insights from the Günter Experiment 6 using TELEMAC & SISYPHE

Subik Shrestha

Technical University of Munich

ABSTRACT

The vertical grain sorting is associated with the deposition and transport process's energy, rate, and duration. In a model where no incoming flux is used, erosion occurs until a static armor layer is formed on the surface of the active layer. A numerical model based on the Günter experiment was built on TELEMAC coupled with SISYPHE to analyze such a phenomenon. Then, the sensitivity of the model's parameters was analyzed, and the relevant combination of parameters was selected for model calibration. After that, the model was calibrated by using water depth and percentage of shorted grains, and the grain sorting, bed level change, and water level were observed and analyzed at different timesteps. The model result showed that Hunziker's bed load transport formula, in combination with Strickler's bed roughness of 61, gave the simulation results closer to the Günters' measurements. The model also showed that the static armor layer started forming on the surface of the active layer after 12 days with the maximum bed shear stress of 1.98 N/m2. For the reliability analysis of these results, this model's result should be compared with the results of other models. As an option, the Artificial Neural Network model could be used.

Keywords: TELEMAC; SISYPHE; bed roughness; Shield coefficient; bed load transport formulas; Gain Size; hydromorphological modeling; sediment transport; numerical simulation; river engineering.

Classification: LCC Code: TC530-665

Language: English

Great Britain Journals Press

LJP Copyright ID: 392922
Print ISSN: 2631-8474
Online ISSN: 2631-8482

London Journal of Engineering Research

Volume 24 | Issue 1 | Compilation 1.0

Hydromorphological Modeling of Vertical Grain Sorting Process. Insights from the Günter Experiment 6 using TELEMAC & SISYPHE

Subik Shrestha

ABSTRACT

The vertical grain sorting is associated with the deposition and transport process's energy, rate, and duration. In a model where no incoming flux is used, erosion occurs until a static armor layer is formed on the surface of the active layer. A numerical model based on the Günter experiment was built on TELEMAC coupled with SISYPHE to analyze such a phenomenon. Then, the sensitivity of the model's parameters was analyzed, and the relevant combination of parameters was selected for model calibration. After that, the model was calibrated by using water depth and percentage of shorted grains, and the grain sorting, bed level change, and water level were observed and analyzed at different timesteps. The model result showed that Hunziker's bed load transport formula, in combination with Strickler's bed roughness of 61, gave the simulation results closer to the Günters' measurements. The model also showed that the static armor layer started forming on the surface of the active layer after 12 days with the maximum bed shear stress of 1.98 N/m². For the reliability analysis of these results, this model's result should be compared with the results of other models. As an option, the Artificial Neural Network model could be used.

Keywords: TELEMAC; SISYPHE; bed roughness; Shield coefficient; bed load transport formulas; Gain Size; hydromorphological modeling; sediment transport; numerical simulation; river engineering.

Author: Technical University of Munich, Germany; Water Resources and Irrigation Development Division Office, Doti, Nepal.

I. INTRODUCTION

The main objective of river engineering is to predict river hydrodynamics and bed-level changes. The principal parameters of this field are discharge, cross-sectional area, water depth, roughness, and grain size. These parameters used in the hydrodynamic model predict the dynamics of rivers. Such river dynamics are generally characterized by roughness and grain size. To understand a complete hydromorphological process, the hydrodynamic models are coupled with the sediment flux and relative bed level changes [1].

Generally, sediment transport relation is described as the transport capacity of a river cross-section at a specific discharge. Hence, a well-calibrated hydromorphological model with particular geometry and bed grain size describes the river location and whether it is aggrading or degrading. A river at its origin has abundantly graveled size bed materials, and in the transport processes, the bedload is a dominant transport mode. As the river follows the valley's slope, the bed grain size decreases to clayey. At this location, suspended load is a dominant transport mode [2].

The study on river transport capacity started 70 years ago when Meyer-Peter and Mueller 1948 published a paper. They considered a uniform sediment model with one mean grain size [3].

However, the bed loads are widely graded, and Mueller already in 1943 noticed grain sorting effects. The Meyer-Peter and Mueller formula was still adopted as there was no other study on these effects [1].

Soon, the study on sediments and river engineering boomed with Harrison's study in

1950, which clearly showed the grain sorting effects. He described a static and mobile armor layer forming under different flow conditions. Both armors were the outcomes of bed level change. The static armor prevented the bed degradation, and there was a low sediment supply [4]. After Harrison, Gessler 1968 studied the static armor closely and developed an algorithm that could predict the armor layer's grain-size distribution. For this, he used the bed shear stress of the original bed material [5], and in 1971, he published a stability criterion for the armor layer [6]. After him, Günter 1971 performed a series of experiments and typically focused on stability criteria to define a threshold value for bed erosion [7], which raised questions on motion threshold and grain sorting processes. However, Einstein in 1950 had already elaborated the hiding and exposure function of mixed grain size [8], and Egiazaroff in 1971 formulated the hiding and exposure function of mixed grains on a hydrodynamic model [9], which simplified and answered the threshold of motion and transport rate. After that, Parker in 1990 and Sutherland in 1992 studied the hiding and exposure functions [10, 11]. Similarly, in 1998, Powell studied the patterns and process of sediment sorting in the graveled riverbed and reviewed the linkages between the pattern and sediment transport process [12]. In 2014, Jia and Zhong used the weighted implicit discretization method to simulate scouring and armoring in alluvial rivers [13]. Zhang et.al., 2020 used Laboratory method with two sets of flumes to analyze the armor layer and found out that statistics on bed armoring are cannot completely define erosions of the riverbed, however, recommended that other flow parameters must be simulated to completely understand the fluctuation in the bedload transport rate [17].

Like others, Gergely et. al., in 2017 used the 3D numerical flow model software called 'BASEGRAIN' coupled with combined application of two bedload transport (Wilcock and Crowe, Van Rijn) formulas and validated their model with the laboratory experiment. They argued that the numerical flow model coupled with combined application of bedload transport formulas improved the results of the numerical simulations [18]. Similarly, Lee and Ahn in 2023 used HEC-RAS 1D to analyze the bed sorting process of the Geum River, Korea in two and three layers. They stated that their model performance on two layers of bed was reliable whereas for the higher layer the model was very unreliable and recommended sufficient investigations on the model [19].

Grain Sorting Process: the grain size distribution in the unconsolidated riverbed, which indicates the energy, rate, and duration of the deposition and transport process [14, 15]. Sediment transport theories state that critical shear stress for incipient motion depends on grain size, which applies only to uniform-sized materials. However, a riverbed contains a wide range of mixture classes where smaller particles hide under the larger particles, severely affecting transport processes. The studies on armoring tests suggest different grain mobilities. Günter, in his experiments, never used sediments as incoming flux. They instead started with conditions that resulted in erosion. This results in erosion upstream while maintaining a constant water level downstream. The result showed the sorted gain size, which implied that the ratio of smaller grains to larger grains was significantly high. So, a sorting process can be described as the variation of the coarsening of the bed surface.

Static Armor: Like in Günter's experiments, if sediments are not supplied at the inlet, a stable armor may form at the bed layer, which does not allow the erosion of the riverbed [5]. If the grain size is finer than the bed materials supplied, all the incoming materials will pass out without affecting the bed level. This does not allow the coarsening of the bed surface. Hence, a static armor layer formed on the surface of the bed layer prevents erosion and thus stops the bed level change.

Mobile Armor: A static armor layer cannot form when shear stress is very high. In such a case, the grain sorting process makes the top layer coarser, the bottom layer finer, and the layer is formed by the mobile armor layer [16]. With this new layer, riverbeds can only be stabilized with the supply of

sediments. Hence, a constant supply of sediment flux is required at the inlet.

Günter Experiments: Günter, in 1971, performed a series of experiments to define bed stability without supplying loads at the inlet and constant water at the outlet. The length of the rectangular flume was 40 meters, and the breath was 1 meter. He performed ten different experiments with varying discharge and bed slopes. As the slope was steep and there was no sediment flux at the inlet, the bed materials were eroded, and the bed level changed. Since constant water depth at the outlet was performed, no erosion occurred at the outlet, and most of the erosion took around the inlet.

When the slope was reduced, the bed shear stress was also reduced, and after many days of observations, the final stage was obtained as the threshold for the shear stress and the stability of the static armor layer. In his experiments, vertical grain shorting was observed. The sorted bed layers were described by the final coarser material at the top layer, which was originally finer where the erosion had flushed the smaller grain-sized material from the reach.

In this way, Günter used the physical model and measured the outcomes thoroughly. Meanwhile many researchers have tried to explain the vertical grain sorting process using numerical models. Some used 1D models and concluded that their model was not sufficient to define the vertical grain sorting process whereas some used 3D flow model coupled with combined bedload formulas which is usually time consuming.

So, this study tries to use a 2D numerical model based on the Günter experiment 6 to see how the parameters behave numerically. For that a Numerical Hydromorphological Model (NHM) was developed in TELEMAC coupled with SISYPHE. Then, a series of tests were conducted to find the effects of numerical parameters on transport processes. The model was then calibrated, and the armor layer was analyzed.

II. MATERIALS AND METHODS

Günter Experiment number 6 is formed in TELEMAC-2D coupled with SISYPHE. The length of the study domain is 40 meters, and breadth is 1 meter. The initial slope of the bed is 0.225% with 7-grain classes of bed materials. The discharge at the inlet is 48 lps, and the constant water level at the outlet is 0.0913 meters. The total simulation time is 691 hours [7].

The National Hydraulics and Environment Laboratory of the French Electricity Board developed TELEMAC-2D. It simulates surface flow in two dimensions using finite volume or finite element method in unstructured mesh. To simulate the flow and transport processes, a steering file containing the configuration of computation, a geometry file of geometrical mesh, a boundary conditions file describing the type of boundaries, an initial state file of computation, a bottom topography file describing the elevation of the riverbed, and the FORTRAN file which contains the specific programming are compiled in one folder.

Bluekenue is used to arrange all required files in a folder. Bluekenue is one of the many processors associated with TELEMAC. The experiment setup and mesh were generated in Bluekenue at a 0.35-meter nodal distance with some added hard points. Then, the slope was added to the mesh. A 2-D interpolation was used to interpolate the applied slope to each mesh node, and the default 'maximum distance' interpolator was used. The geometry file must be a SELAFIN object with a variable as the bottom slope so the TELEMAC recognizes it as the bathymetry for the project.

After this, the boundary conditions file is created in ASCII format. Bluekenue makes all boundaries solid, and to define an open boundary, discharge and water level data are required at the inlet and outlet, respectively. At the inlet, the 'open boundary with prescribed Q' and at the outlet, 'Open boundary with prescribed H' is used with the tracer code 'open boundary with prescribed tracer' applied to both ends. The boundary code for 'prescribed Q' is 455, and for 'prescribed H' is 544.

In addition, the number of grain classes, including their portion, were added in the FORTRAN file, and the simulation variables were described in the steering file. This file couples TELEMAC -2D with other files like FORTRAN, SISYPHE, etc. The other files, like boundary conditions files and geometry files, are also defined in the steering file. To generate the initial flow condition, the time step and the number of time steps were initially adopted 0.5 and 1000. Then the initial flow conditions were added to the initial condition file. From the experiment 6, the prescribed flow rate at the outlet and inlet of 0 m^3/s and 0.048 m^3/s, were adopted with the specified elevations at the outlet and inlet being 0.0813 and 0, respectively. Strickler's roughness coefficients are defined at bed and banks 50 and 100.

$$\text{Strickler's coefficient} = \frac{1}{n} = \frac{26}{d_m^{\frac{1}{6}}}$$

Where n is Manning's roughness, and dm is the mean grain size.

TELEMAC-2D is then simulated on the Leibniz-Rechenzentrum der Bayerischen Akademie der Wissenschaften (LRZ) supercomputing computer at the Technical University of Munich, Germany. A short simulation was made to generate the initial condition file. Then, output SELAFIN files were animated on Bluekenue, and the stability of the model was checked. The stable output file is then used as an initial conditions file with the command "COMPUTATION CONTINUED = TRUE," previously applied initial conditions were commented out. Considering the stability of the numerical model, the time step of 0.5 seconds is used for the whole simulation period.

On the other hand, sediment data were defined on the SISYPHE file. The mean diameter of grain classes 1-7 sediments are 0.00102 m, 0.0020 m, 0.0031 m, 0.0041 m, 0.0052 m, 0.006 m, and 0.3 m respectively [10]. The active layer thickness is 0.06 m, and the number of bed layers is 3. Hunziker's bed load transport formula adapts the Meyer-Peter and Muller formula. The same friction coefficient is used on both steering files. The shield parameter for each grain class used is 0.047.

Hunziker's volumetric sediment transport per sediment class is:

$$\emptyset_{bi} = 5 * \pi * [\omega_i * (\theta_i^{'} - \theta_{cm})]^{\frac{3}{2}}$$

This formula is only valid when $\theta_i^{'} > \theta_{cm}$. $\theta_i^{'}$ Is Shields parameter and θ_{cm} is corrected Shields parameter. TELEMAC computes θ_{cm} using the Critical Shields parameter, mean grain size of the surface layer, and the underlying layer. The formula also adopts a hiding function and is defined by ω_i. The volumetric sediment transport is computed for each grain class 'i'.

Finally, the SISYPHE file is coupled with the TELEMAC file for the first run. The desired simulation output can be achieved by changing the printout period. For the simulation, 12 hours as a printout period, which is 86400 timestep, is used. The output files are animated in Bluekenue, and the corresponding final water level, grain size, and slopes are compared to the original document of Günter's experiment. Shields coefficients and bed roughness are adjusted to calibrate the model, and the output data are compared with experimental data.

III. RESULTS

There are many parameters associated with hydromorphological modeling, and to find an exact relation between measured and simulated data, each parameter must be analyzed. Hunzikers' sediment transport model was initially analyzed at a separate Shield's coefficient, keeping bed roughness constant at Strickler's 50. The change in grain sorting and water depth is shown in Figure 1.

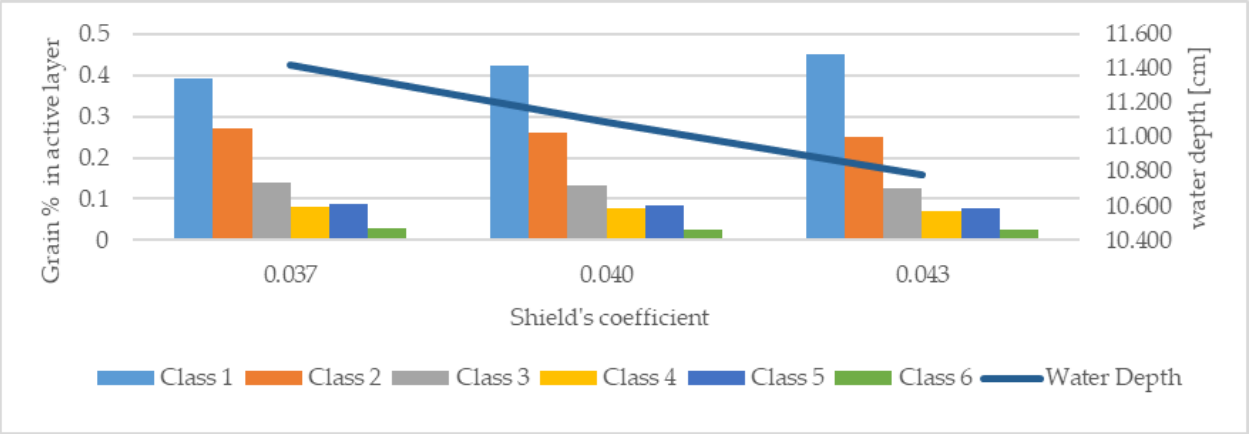

Figure 1: This is a Plot of the Final Percentage of Grain Class in the Active Layer of the Riverbed and Corresponding Water Depth at Constant Strickler's 50 and Shield's coefficients of 0.037, 0.04, and 0.043

After that, the reverse of the previous was analyzed. Shield's coefficient is kept constant at 0.040, and three analyses on Strickler's coefficients of 30, 40, and 50 were made. The plot of grain sorting and water depth is shown in Figure 2.

Observing the sensitivity of both Shields' and Strickler's coefficient,, both parameters are modified simultaneously to observe the effect on the river morphology. The impact on grain sorting and water depth is shown in Figure 3.

The thickness of the active layer was not completely defined in Günter's experiment, and as an initial guess, a thickness of 0.06 meters was adopted. Then, the different values of active layer thickness were analyzed at varying Shield's and Strickler's coefficients. The plot is shown in Figure 4.

Figure 2: This Is a Plot of the Final Percentage of Grain Class in the Active Layer of the Riverbed and Corresponding Water Depth at Constant Shield's coefficient of 0.040 and Strickler's coefficientsat 30, 40, and 50

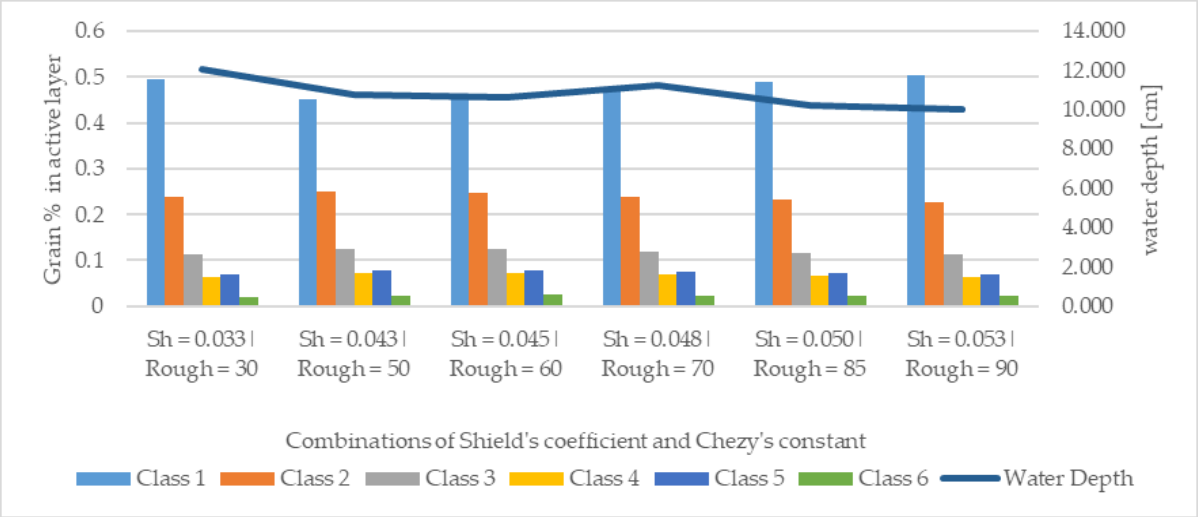

Figure 3: This Is a Plot of the Final Percentage of Grain Class in the Active Layer of the Riverbed and Corresponding Water Depth at Different Combinations of Shield's coefficient and Strickler's coefficients

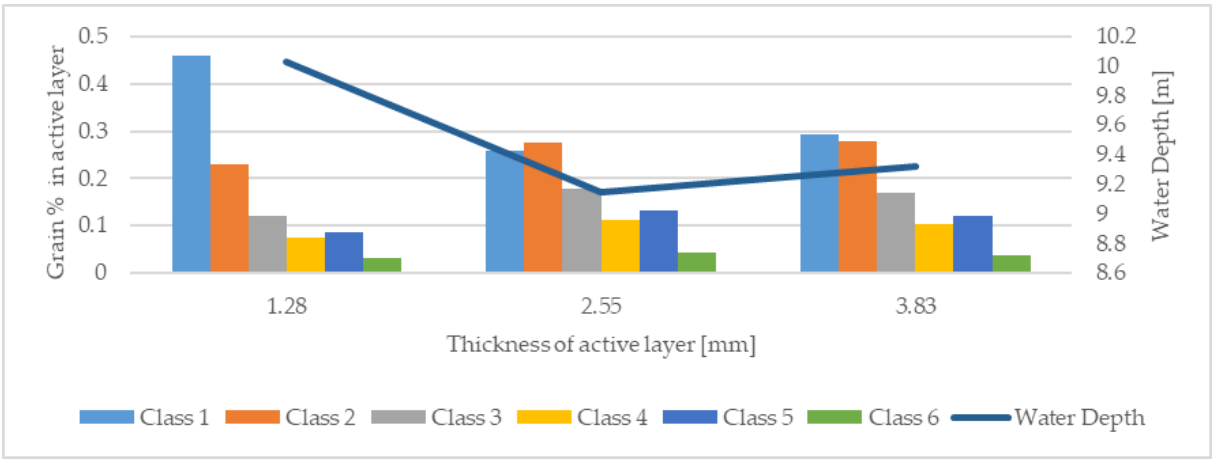

Figure 4: This Is a Plot of the Final Percentage of Grain Class in Different Thicknesses of the Active Layer of the Riverbed and the Corresponding Water Depth

Even after analyzing different parameters, some hidden parameters, like hiding function coefficients, could significantly impact sediment transport. So, a study on default value and one higher value was carried out, keeping other parameters constant. The plot of the analysis is shown in Figure 5.

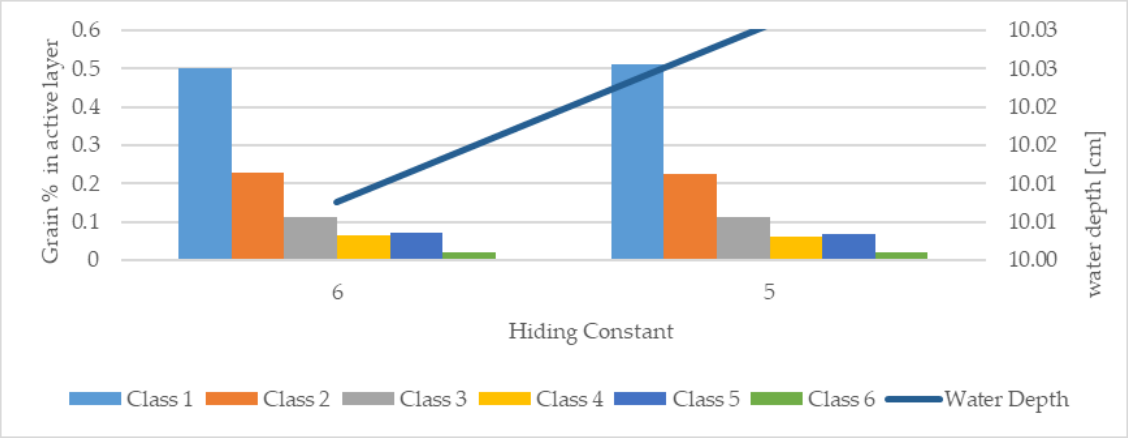

Figure 5: This Is a Plot of the Final Percentage of Grain Class in the Active Layer of the Riverbed and Corresponding Water Depth at Two Different Hiding Function Constants of 6 and 5. 5 Is a Default Value

Besides, there are many transport formulas associated with TELEMAC and SISYPHE. Various simulations were conducted to analyze them at constant Shield's and Strickler's coefficients. The result of the analysis on grain sorting and water level change is shown in Figure 6.

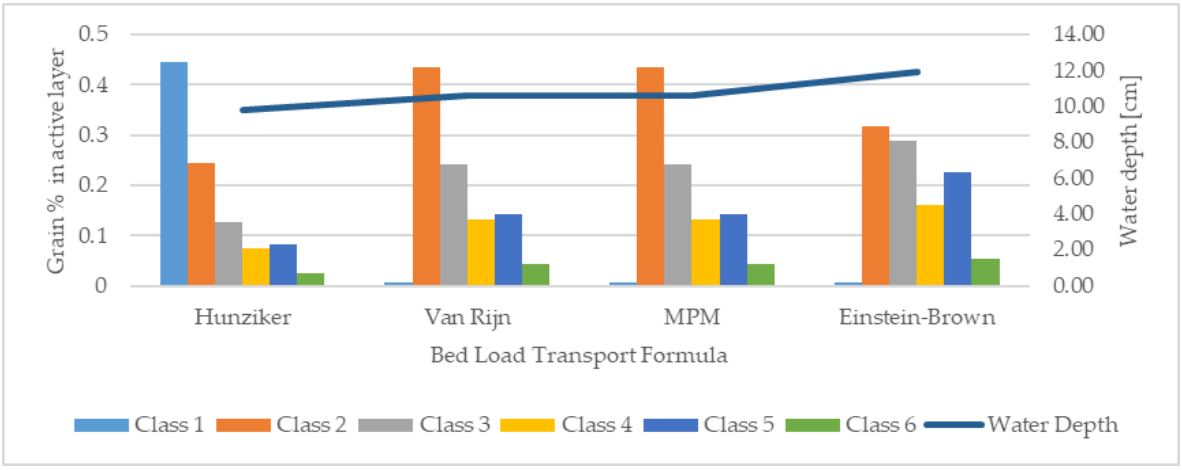

Figure 6: This Is a Plot of the Final Percentage of Grain Class in the Active Layer of the Riverbed and Corresponding Water Depth at Different Bed Load Transport Formulae

To achieve the water level as measured by Günter in his physical model, it is also necessary to analyze the model with different initial water levels. To do so, two water levels were analyzed, i.e., 8.13 cm and 7.13 cm. The results are plotted and shown in Figure 7.

Finding a perfect agreement between measured and simulated data is always tricky. The required water depth was achieved using Hunziker's bedload transport formula at Shield's coefficient of 0.047 and Strickler's roughness coefficient of 61 in thickness of active layer 2.5 mm. Still, the grain sorting did not match the physical measurements made by Günter. The evolution of bed grain, slope, and water depth is shown in Figure 8.

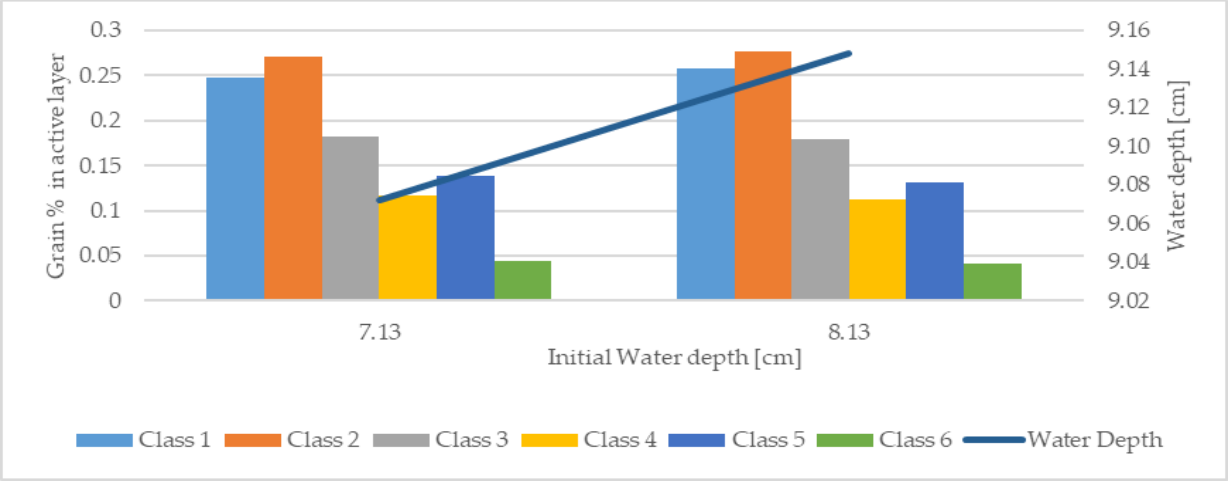

Figure 7: This Is a Plot of the Final Percentage of Grain Class in the Active Layer of the Riverbed and the Corresponding Water Depth at Two Different Initial Water Level Conditions. 9.13 Cm Is the Last Water Level Measured Experimentally by Günter

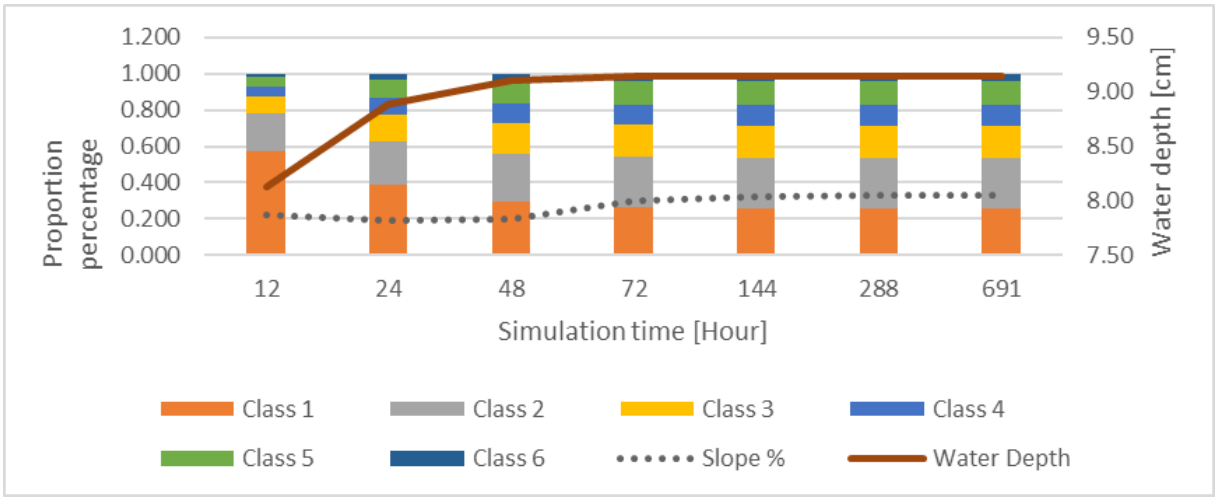

Figure 8: This is a Plot of the Final Percentage of Grain Class in the Active Layer of the Riverbed and the Corresponding Bed Slope and Water Depth at Different Time Steps. A Dotted Line With Levels at the Primary Axis Shows the Slope in Percentage. The Primary Axis Also Represents the Total Portion of Grain Classes.

VI. DISCUSSION

Bed roughness is one of the sensitive parameters in river hydrodynamics, and Shield's coefficient is another sensitive parameter in riverbed transport processes. These two parameters are essential to developing a hydromorphological model. To understand their behavior on the grain sorting and water depth, both were analyzed separately and jointly.

At a higher Shield's coefficient, keeping the Strickler's coefficient constant at 50, a portion of the class 1 grains increases while the portion of the other classes decreases. This showed that with an increase in 'θcr,' the portion of the fine grain class increases, while the coarser grain class decreases in the active layer. The water level also decreases from 11.40 cm to 10.70 cm (see Figure 1), which implies that higher bed shear stress leads to increased sediment transport, resulting in a lower water level.

Similarly, at a higher Strickler's coefficient, keeping Shield's coefficient constant at 0.040, a portion of class 1 grain decreases, and a portion of the other classes increases. This showed that, with the increase of roughness, the portion of the finer grain class decreases, and the amount of coarser grain class increases, while the water depth also decreases with increased bed roughness. This implies that higher bed roughness affects sediment transport and reduces water depth (see Figure 2).

However, varying results were obtained when both coefficients were analyzed simultaneously (see Figure 3). This might be the combined effect of changes in bed shear stress and bed roughness, which leads to complex and non-linear interactions, resulting in outcomes that are not directly predictable based on individual variations in each coefficient.

The result above implied that, by increasing both the bed roughness and the Shield's coefficient, the development of numerical simulations could get closer to the measured results. Combinations of various increasing values of both parameters were analyzed. The plotted story (see Figure 3) showed that Strickler's coefficient between 60 - 70 and Shield's coefficient between 0.045 – 0.048 could give better results. After that, increasing values of both parameters showed fluctuation in grain sorting and water level.

The joint analysis on Shield's coefficient and Strickler's coefficient showed an excellent progression in the calibration of the model; however, the measured results were still far from the simulations' results. So, the thickness of the active layer was analyzed (see Figure 4). The plotted results showed that by decreasing the thickness of the active layer up to 2.55 mm, the finer grain class and the water level decrease, and a portion of the coarser grain class increases. But if the coating is further decreased, the opposite phenomenon occurs where the water level and a bit of fine grain class rise rapidly. Figure 4 also showed that the thickness of the active layer is the most sensitive parameter in this study.

Besides, other parameters like the hiding function's constant could change the grain sorting process. For this, a default value was analyzed with a higher value (see Figure 5), and the result was almost the same. With higher values, the water level and portion of finer grain decreased but not significantly.

In addition to these, many available bed load transport formulae are analyzed separately (see Figure 6). The result showed that the portion of finer grain was higher, and the water level was lower in Hunziker than in others. The result also showed that Van Rijn, MPM, and Einstein-Brown formulas allocated the maximum portion for grain class 2 in active layers. It is also seen that Van Rijn, MPM, and Einstein-Brown recipes gave higher bits for coarser grain class, e.g., class 5 and 6, than Hunziker.

After that, the initial water level applied to the model was also analyzed and plotted (see Figure 7). The plot showed that the final water level also increased, and the finer grain class 1 portion increased with the increasing water level.

Finally, analyzing all the parameters, formulas, and initial conditions, two combinations were implemented. First, the Van Rijn formula with Shield's coefficient of 0.06, Strickler's coefficient of 117, 25 mm thick active layer, and 8.13 cm initial water level. Second, the Hunziker formula with Shield's coefficient of 0.047, Strickler's constant of 61, 2.55 mm thick active layer, and 8.13 cm initial water level. The latter was more appropriate, and the complete grain sorting process result, water level, and bed slope change were plotted at different time steps (see Figure 8).

In 12 hours of simulations, the portion of grain class 1 is more than 50%; the slope is 0.225%, and the water level is 8.13 cm. This is closer to the initial condition; this implied that nothing special was observed within the first 12 hours. After a day, the portion of grain class 1 significantly decreased to 38% while the portion of the other class increased. The water level also increased to 8.9 cm, but the slope decreased to 0.19 %. The maximum bed shear stress was 1.89 N/m^2. After two days of simulations, a portion of grain class 1

further reduced to 29% while the water level was observed at level 9.1 cm, and the maximum bed shear stress increased to 1.97 N/m².

Similarly, at the end of 3rd day, the grain sorting process continued by decreasing the portion of grain class 1 and increasing others. The water level also increased to 9.14 cm and the slope to 0.3 %. Then after the grain sorting and bed level change process retarded and can be seen on the plot at time step 144 hours. At the end of 288 hours, the change in grain sorting, water level, and bed slope is insignificant compared to the previous time step, and if compared to the last time step, the grain distributions, water level, and slope are constants. The maximum bed shear stress after 12 days was 1.98 N/m². This implied that after 288 hours or 12 days, the static armor layer was formed at the active layer's surface, protecting the grain from erosion. These 12 days can also be considered a threshold for creating a static armor layer.

However, the simulation results are still far from Günter's measurements, and the water level only comes closer to experimental data. Many parameters are associated with model calibration, and not every parameter is defined numerically in reality. A few were studied, and researchers have applied them as a numerical reference for numerical modeling. Those studies were a simplified prototype version, and many assumptions were made to find a relation. Those assumptions may not work for every scenario. So, other numerical parameters that could define the transport behavior better are required. An artificial neural network (ANN) can be used as an option. But it's always better to use two or more numerical models to see how the models represent reality. Also, there could be human errors in measuring the experimental model. A good model calibration is impossible due to the lack of numerical parameters and measurement errors. For this, updated parameters and precisely taken measurements will be required.

V. CONCLUSIONS

There are many formulas and parameters associated with them in numerical hydromorphological modeling. Choosing the best combination among them is one of the main tasks in the model calibrations. It was observed that local sensitivity analysis is not enough to calibrate a model, so a global sensitivity analysis was required. After performing the simulations out of best combinations, i.e., Hunziker formula with Shield's coefficient 0.047, Strickler's coefficient of 61, 2.55 mm thick active layer, and 8.13 cm initial water level gave a better output. It was seen that it took some time to form a static armor layer on the surface of the active layer, and in this model, it took 12 days. After the armor layer was created, the riverbed erosion completely stopped, and so did the grain sorting process, where the maximum bed shear stress was 1.98 N/m². The final portion of grain class from 1 to 6 is 26%, 28%, 18%, 11%, 13%, and 4%, respectively; the bed slope is 0.33%, and the water depth is 9.15 cm. However, these results are still far from experimental results. So, using two or more numerical models for the analysis would be better. To find a good relation between them, updated parameters, their range, and precisely taken measurements will be required.

ACKNOWLEDGEMENT

I would like to acknowledge Dr. Markus Reisenbüchler for his invaluable guidance, Shubhechha Paudyal for her unwavering support, and the Technical University of Munich, Germany, for providing access to their resources.

REFERENCES

1. Hunziker, R.P. and M.N.R. Jaeggi, Grain Sorting Processes. Journal of Hydraulic Engineering, 2002. 128(12): p. 1060-1068.
2. Vercruysse, K., et al., Linking temporal scales of suspended sediment transport in rivers: towards improving transferability of prediction. Journal of Soils and Sediments, 2020. 20(12): p. 4144-4159.
3. Meyer-Peter, E.a.M., R. Formulas for Bed Load Transport. in Proceedings of 2nd meeting of the International Association for Hydraulic Structures Research. 1948. Delf.
4. Harrison, A.S., Report on special investigation of bed sediment segregation in a degrading

bed, in Sediment Series, U.A.C.o. Engineers, Editor. 1950, Missouri River Division: USAMIssouri.
5. Gessler, J., The Beginning of Bedload Movement of Mixtures Investigated as Natural Armoring in Channels., in W. M. Keck Laboratory of Hydraulics and Water Resources Report, T-5. 1965, California Institute of Technology: Pasadena, CA. 1965.
6. Gessler, J., Beginning and ceasing of sediment motion. River Mechanics. 1970, Fort Collins, CO: Colorado State University.
7. Günter, A., Die kritische mittlere Sohlenschubspannung bei Geschiebe mischungen unter berücksichtigung der Dechschichtbildung und der turbulenzbedingten Sohlenschubspannungs schwankungen. 1971, ETH Zuerich (CH).
8. Einstein, H., The bed load function for sediment transportation in open channel flows. Techncial Bulletin 1950. 1026.
9. Egiazar off, J. La non-uniformite´ des sédiments et son influence sur le débit solide pour lit affouillable et pour lit fixe. Méthodes de calcu. in 14th Congress, Int. Association for Hydraulic Research ~IAHR! 1971. Paris: Int. Association for Hydraulic Research ~IAHR!
10. Parker, G., Surface-based bedload transport relation for gravel rivers. Journal of Hydraulic Research, 1990. 28(4): p. 417-436.
11. Sutherland, A.J., Hiding function to predict self armoring, E. Zuerich, Editor. 1992, Inst. of Hydraul., Hydrol. and Glaciol.
12. Powell, D.M., Patterns and processes of sediment sorting in gravel-bed rivers. Progress in Physical Geography: Earth and Environment, 1998. 22(1): p. 1-32.
13. Jia, B.a.Z., D, D. Scouring and Armoring in Alluvial Rivers. ICHE Hamburg - Lehfeldt & Kopmann, 2014.
14. Compton, R.R., Manual of field geology. 1962: John Wiley & Sons,. 378.
15. Tucker, M.E., Sedimentary rocks in the field. 1996, Chichester: John Wiley & Sons.
16. Parker, G. Some random notes on grain sorting. in Int. Seminar on Grain Sorting, Ascona, Mitteilungen Nr. 117 der Versuchsanstalt für Wasserbau, Hydrologie und Glaziologie. 1992. ETH Zuerich: ETH Zuerich.
17. Zhang, S., et al., Laboratory study on the evolution of gravel-bed surfaces in bed armoring processes. Journal of Hydrology, 2021. 597: p. 125751.
18. Török, G.T., S. Baranya, and N. Rüther, 3D CFD Modeling of Local Scouring, Bed Armoring and Sediment Deposition. Water, 2017. 9(1): p. 56.
19. Lee, J. and J. Ahn, Analysis of Bed Sorting Methods for One Dimensional Sediment Transport Model. Sustainability, 2023. 15(3): p. 2269.

This page is intentionally left blank

Concrete Beam Reinforced by Steel Fiber (Review)

Sally Jalil

ABSTRACT

Many literature reviews dealt with the effect of fibers on concrete performance by using different types of fibers. This study introduces some literatures related to using fibers in reinforced concrete beams for the period (2004-2021). The following section presents the previous studies of the flexural behavior of fiber reinforced concrete (FRC) beams for steel type of fiber especially. Next, the points of agreement and disagreements between studies are demonstrated briefly. Moreover, comments on previous studies are inserted. Then, a section covers the benefits of previous studies. Finally, the knowledge gap is clarified by recognizing this study's differences.

Keywords: RC beams, flexural strength, SFRC, steel fiber, fiber content, volume fraction.

Classification: LCC Code: TA401-492

Language: English

Great Britain Journals Press

LJP Copyright ID: 392923
Print ISSN: 2631-8474
Online ISSN: 2631-8482

London Journal of Engineering Research

Volume 24 | Issue 1 | Compilation 1.0

Concrete Beam Reinforced by Steel Fiber (Review)

SallyJalil

ABSTRACT

Many literature reviews dealt with the effect of fibers on concrete performance by using different types of fibers. This study introduces some literatures related to using fibers in reinforced concrete beams for the period (2004-2021). The following section presents the previous studies of the flexural behavior of fiber reinforced concrete (FRC) beams for steel type of fiber especially. Next, the points of agreement and disagreements between studies are demonstrated briefly. Moreover, comments on previous studies are inserted. Then, a section covers the benefits of previous studies. Finally, the knowledge gap is clarified by recognizing this study's differences.

Keywords: RC beams, flexural strength, SFRC, steel fiber, fiber content, volume fraction.

Author: Civil Engineer, Governmental Company of Thi-Qar Oil, Thi-Qar, Iraq.

I. INTRODUCTION

During the last few decades, the possibility of enhancing the properties of concrete by employing fibrous materials such as steel fibers in concrete mixes has been extensively investigated. Many research articles have studied the effect of fibers on concrete performance by using steel type of fibers.

Fibers are in the form of small pieces that are added to the cement materials randomly and discontinuously that reduces the numbers of micro-cracking then improve the toughness, ductility, and cracking tensile strength of concrete members. The following literature reviews focus on steel type of fiber specially to support the scientific background on the effect of this type on the flexural strength of RC beams.

II. THE PREVIOUS STUDIES OF THE FRC PROPERTIES BY USING STEEL FIBER

Song and Hwang, 2004 [1] studied the effect of steel fiber's addition on the mechanical properties of high strength concrete (HSC) of 85 MPa when the volume fraction of fiber was applied in a range from 0% to 2% with 0.5% interval. The steel fiber used has a geometry of Hooked-Ends which are available in bundles with 30 fibers. The average length of fibers used was 35 mm with 0.55 of nominal diameter. This study has been considered four properties of SFRC; included compressive and tensile strengths (by casting standard cylindrical concrete specimens), toughness, and modulus of rupture (by casting prism concrete specimens).

Tests results showed that steel fiber with a 1.5% of volume fraction recorded the best compressive strength of SFRC that reached 15.3% over the HSC. While the distinct enhancing has been resulted in splitting tensile strength and modulus of rupture which they achieved 98.3% and 126.6% increasing, respectively, by adding steel fiber with max volume fraction (2% in this study). Moreover, the increasing steel fiber content has been obtained more toughness index as compared with HSC.

Altun et al., 2005 [2] studied the effect of SF addition on the mechanical properties of RC beams. RC beams with C20 and C30 have been fabricated with addition SF at dosages 30 and 60 kg/m3 for each compressive strength. The steel fibers type used in the study were hooked ends (Dramix RC-80/0.6-Bn) as shown in with 0.75 mm diameter and 60 mm total length. Nine RC beams with cross-section dimensions of 300 x 300 mm and 2000 mm in length were investigated. All beams were tested under the third-point bending scheme. The study concluded

that doubling the SF's mass from 30 to 60 kg/m3 resulted in a trivial enhance in both ultimate load and toughness. Where a 166% increasing in toughness occurred for SFRC beams with 30 kg/m3 as compared with RC beams (no fiber). But, SFRC beams with 60 kg/m3 resulted in toughness only 17% greater than the toughness of SFRC beams with 30 kg/m3. As the same behavior, the ultimate load relatively developed with little increase for a twofold increase in fiber's mass. Therefore, the study stated that the SF dosage of 30 kg/m3 is the best considering the economical side of the strengthening option.

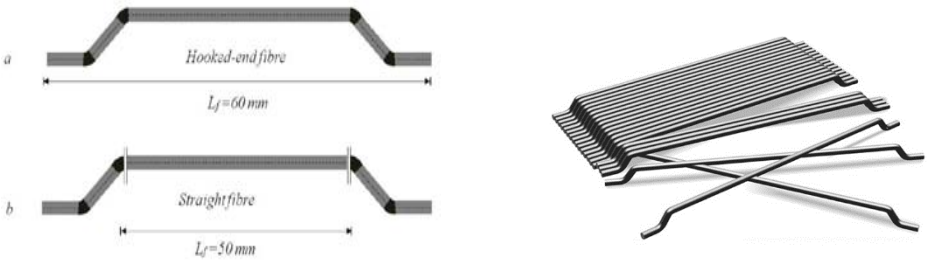

Figure 1: Dramix type of Steel Fiber

Thomas and Ramaswamy, 2007 [3] presented an analytical and experimental program of the mechanical properties of steel fiber reinforced concrete based on an analysis of 60 standard test specimens data. The concrete grades were 35, 65, and 85 MPa with variable volume fractions of steel fiber of 0.0, 0.5, 1.0, and 1.5%. The fibers applied were hooked-end type (glued in bundles) and the dimensions as displayed in Figure 2. The obtained results showed that the maximum increase in the splitting tensile strength has been increased to about 40% as compared to the traditional concrete. However, the compressive strength has only increased by 10% in almost all concrete grades studied. On the other hand, the fiber dosage had to increase up to 1.5% (about 120Kg/m^3) to obtain a sufficient improvement in the toughness. Based on the analysis of results data, empirical models proposed in the study for predicting the strength properties of SFRC based on the concrete grade and reinforcing index of fiber (RI).

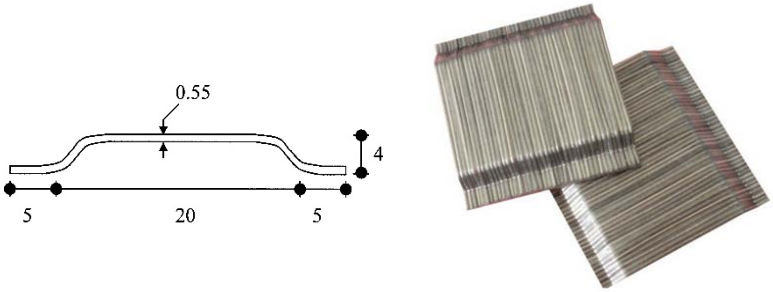

Figure 2: Steel Fiber Hooked-End Type Glued in Bundles

Bencardino et al., 2008 [4] used the standard experimental procedures of cylindrical specimens test to obtain the compressive strength of steel fiber reinforced concrete (SFRC) to study the effect of addition steel fiber to the compressive strength of plain concrete. In addition, a theoretical model was proposed to realize the stress-strain reliability in compression. Hooked-end steel fiber with 22 mm length was applied in three percentages of volume fraction including: 1%, 1.6%, and 3%. Results showed that while there was no increase in compressive strength as a result of adding the fibers, the stiffness and brittleness of SFRC were observed due to the fiber content increasing. So that, higher fiber contents (Vf = 1.6% and 3 %) showed values of ultimate strain about five times over the ultimate strain of concrete with no fiber and the softened branch of SFRC became more extended.

Uygunoğlu, 2008 [5] studied the flexural behavior of SFRC by using two different lengths of

Hooked-end steel fiber (30 and 60 mm) which was available in bundles form of about 30 pieces. The steel fiber inclusion in the concrete mix by a ratio of concrete volume ranged from 0% to 0.8% with 0.2%. The researcher was prepared nine concrete prisms of 100×100×350 mm and tested by the midpoint loading at age of 7, 28, 56, 180, and 360 days, in addition to scanning electron and optical microscopy of specimens at 180 days of curing age to investigate the bond characteristic between fibers and concrete mixture. In this study, polarizing microscopy observed good bonds in the interface zone of hybrid concrete mixture where the cementitious materials were densely covered the fiber surface that led to a stronger connection of concrete matrix. Besides, as long as fiber content increased, there was an increase in flexural strength of SFRC whereas the growth of the first crack reduced significantly.

Xu and Shi, 2009[6] aimed to assess the satisfaction of empirical relations among the mechanical properties of hybrid concrete to SFRC by depending on experimental data collected from previous literature then analyzed their correlations also. In that empirical relations depended, the hybrid concrete obtained by adding either glass or polypropylene fiber in addition to relations with normal concrete. Researchers collected a large number of tests results from many published studies that deal with the main topic of this study to investigate the applicability of empirical relations. Generally, the experimental data collected were limited of parameters with volume fraction of steel fiber ranged from 0.5% to 2%, water to binder ratio (w/b) ranged from 0.25 to 0.5, an aspect ratio of steel fiber ranged from 55 to 80 and the specimens were cylinder and prism. The evaluation results found that it is not possible to carry out the empirical relationships to SFRC, and this led to the necessity of analyzing the collected results to obtain a correlation of the mechanical properties of concrete. As a result, the study concluded that the mechanical properties of SFRC are affected by many factors, such as curing, an aspect ratio of fiber, the geometry of fibers used, w/b ratio, and fiber dosage. Therefore, a large number of parameters can be applied to benefit in subsequent studies. Exclusively, this study presented a strong factor to determine the relationship between compression and tensile strengths of SFRC, which is Regression encoded R^2 as observed in Equation 1. Where R^2 has the magnitude of 0.94% for compressive strength and 0.90% for tensile strength. Moreover, another strong factor of Integral Absolute Error (encoded IAE) produced by investigations, which it represents the relationship between tensile and flexural strengths of SFRC. The relation of IAE as displayed in Equation 2; the values of the IAE factor are 8.17% for tensile strength and 15.86% for flexural strength.

$$f_{ts}{}^{*} = A(f_{cs})^{B} \quad (1)$$

$$IAE^{**} = \sum \frac{\sqrt{(Q_i - P_i)^2}}{\sum Q_i} \times 100 \quad (2)$$

Where:

** fi_{ts} is either tensile or flexural strength MPa; A and B is Regression factors*
*** Qi: experimental result; Pi: prediction result*

Marar et al., 2011[7] study the toughness of specific compression of SFRC depending on the effect of the Fiber Reinforcement Index (FRI). Equation 3 explains how to calculate the FRI of steel fiber used.

$$FRI = volume\ fraction \times (\frac{length}{diameter}) \quad (3)$$

Two mixes of SFRC create to fabricate cylindrical specimens; normal mix (NSFRC) with 0.55 w/c ratio and high strength (HSSFRC) with 0.31 of w/c. The geometry of steel fiber used was Hooked-ends with three variable aspect ratios of 60, 75, and 83. Moreover, six percentages of

volume fraction of steel fiber utilized; 0.5%, 1.0%, 1.25%, 1.5%, 1.75%, and 2.0%. Therefore, thirty-eight cylinder specimens have been fabricated and tested under compression toughness tests. Generally, all tests results recorded a regular increase in toughness attributed to fiber inclusion in the concrete mix at 2% volume fraction that indicated in *Figure 3*. By analyzing the experimental results, this study proposed four categories equations of correlations among the compression toughness of SFRC. These categories included:

1. Depending on the FRI, in the first category, the researchers proposed equations to determine the influence of compression toughness ratio by adding fiber to plain concrete.
2. To evaluate the compression toughness specific of both NSFRC and HSFRC, equations deals with both FRI and compression toughness of ordinary concrete have been exhibited in the second category.
3. For both NSFRC and HSFRC, the equations of the third category are linked between FRI and compression toughness index.
4. The final category proposed equations to specify the values of the relationship obtained in the previous category (No.3).

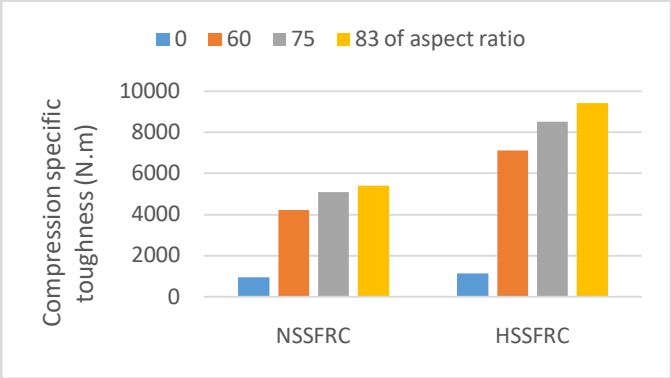

Figure 3: Compression Specific Toughness Results of Concrete Versus Aspect Ratio of Fiber

Pouliot et al., 2011[8] investigated the effect of geometry and volume fraction of steel fiber on the flexural behavior of SFRC. Two geometries of steel fiber were used: the first type was waved steel fiber with 0.75 mm diameter and 25 mm length. The other was hooked ends steel fiber with 0.75 mm diameter and 31 mm length. The two types of steel fiber are illustrated in Figure 3. The study applied four-volume fractions of steel fiber ranged from 0.0 to 1.5% with 0.5% interval. Generally, the experimental results indicated that fiber plays an important role in enhancing the mechanical properties of concrete, especially with high fiber volume fractions. However, it has been stated that as the fiber quantity increased in the concrete mix, the workability decreases significantly, and therefore, the consolidation process of FRC would be very difficult which results in more air content in the mixture. In addition, analysis of compressive strength results indicated that fiber had little effect on the compressive strength of concrete. Some experimental work and results have been reported by Sasikala & Vimala, 2013[9].

a) Waved b) Hooked ends

Figure 4: Types of steel fiber used

Vairagade and Kene, 2012 [10] collected and investigated some highlights for the performance of SFRC by some previous studies that deal with it. The researchers came to the fact by depending on published works of literature that, in any design of concrete mix, the workability decrease in the hardened state, due to properly bonding of steel fiber addition because that fiber arrangement in form of networks structure inside the concrete led to inhibit the flow and segregations of fresh concrete. For that reason, superplasticizers may introduce that does not affect of mechanical properties under study. Furthermore, the study indicated that the usage of steel fiber improved the tensile strength, flexural strength, and toughness of concrete matrix especially with high volume fractions of fiber. Besides, the enhancement in compressive strength of concrete stabled at a low level.

Deluce and Vecchio, 2013[11] studied the behavior of cracking and stiffness of SFRC. Many parameters applied in this study, included fiber volumetric content ranged from 0% to 1.5% with 0.5% interval, fiber length of 30 mm, aspect ratio of 48,55 and 79, six conventional reinforcement ratio and steel reinforcing bar diameter ranged from 10M to 30M (by using Canadian size of bars). So that, 12 RC specimens and 48 SFRC specimens were tested under uniaxial tension tests. Test results showed that the conventional reinforcement affected the performance of the crack were using a large size of bars and a high ratio of conventional reinforcement leads to a positive effect on the width and distribution of cracks. The same influence was observed with a diversity of steel fiber by volume fraction and aspect ratio where the post-yield capacity of RC increased. By contrast, the post-cracking capacity was independent of the length of steel fiber.

Rizzuti & Bencardino, 2014[12] analyzed the effect of steel fiber on the mechanical properties (compressive and flexural behavior) with fiber volume fractions of 1.0, 1.6, 3.0, and 5.0%. The steel fiber used has hooked ends and a total length of 22 mm. Fifteen standard cylinder samples for compression test and fifteen prisms for four-point load test carried out of plain concrete and SFRC. The concrete grade was 60 MPa. The results indicated that fiber has not affected the compressive strength as opposed to the positive effect of the flexural strength. It has been also stated in that study that higher steel fiber content has considerably enhanced the fracture strength and the post-peak behavior. But, at a very high volume fraction of steel fiber (1.5%) the samples needed a longer vibration period during the casting process to ensure that the fibers are homogeneously distributed within the mixture to avoid the appearance of the fibers on the casting surface layer as shown in Figure 4.

Figure 5: Appearance of the Fibers on the Casting Concrete Surface

Yoo et al., 2016[13] investigated the effect of size specimens on the flexural performance of concrete reinforced with hooked-end steel fiber. Three different geometries of concrete beams were presented of large, medium, and small size. The largest has dimensions of 150×150×550 mm while the medium and small sizes have 100×100×400 and 50×50×250 mm in dimensions, respectively. Figure 6 illustrated the sizes of specimens used.

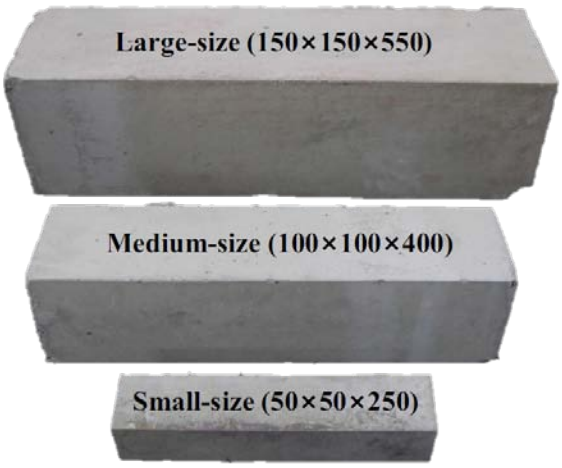

Figure 6: Geometry of Specimens Used (Units: Mm)

Eight uniform concrete mixes were applied for all beams. The parameters were: (a) The ratio of water-to-cement of 60 and 45 to study the flexural behavior in different compressive strengths of concrete. (b) Hooked-ends steel fibers (S) with 30 mm length and 0.75% of volume fraction were added to all concrete mixtures. (c) Another type of fiber was used of amorphous metallic fibers (AM) with 30 mm length and volume fractions of 0.5 and 0.75%. The data of experimental results were found that the increase in the size of the specimen adversely affects the flexural behavior of FRC but by increasing the fiber content so that it controls the improvement of flexural strength of beams that issue may be solved. The effect of specimens size was more evident at the high compressive strength of FRC due to the better bonding resulted from the hooked ends of the fiber.

D. A. Sinha & Verma, 2017 and 2018 [14] [15] investigated the effect of steel fiber with varying volume fraction of (0.0, 0.5, 0.75, 1.0, 1.25, 1.5, 1.75 and 2.0%) on the strength and workability properties of high–strength (M60 grade) concrete. The additional steel fibers have a crimped flat shape (as shown in Figure 5) of 35 mm total length and 0.7 mm thickness. The study was carried out on standard cubes (compression strength test), standard cylinders (tensile strength test), and standard prism (flexural strength test) of SFRC. Based on the experimental results, the authors concluded that the optimum percentage of SF is 1% by volume fraction, where adding more than this percentage has decreased the compressive and tensile strengths of concrete because of balling effect that can result in improper bonding between fiber and the constituents of the concrete mixture. As well as, by applying 1% of steel fiber the compression and tensile strength have increased by 3.7 %, 22% respectively. It is worth noting here that the flexural strength has been increased as the volume fraction of steel fiber increased since that fibers can act as bridging devices across the cracks during the loading state. Thus, adding 2% steel fiber enhanced the flexural strength by 18%.

Figure 7: Crimped Flat Shape of Steel Fiber

Abbass et al., 2018[16] investigated the mechanical properties of SFRC with three different compressive strengths of concrete. Three lengths 40 mm, 50 mm, and 60 mm of hooked ends steel fiber with two diameters of 0.62 mm and 0.75 mm were mixed with concrete as exposed in Figure 8. Also, 0.25, 0.35, and 0.45 of water/cement ratio and 0.5, 1,1.5% of volume fraction were used.

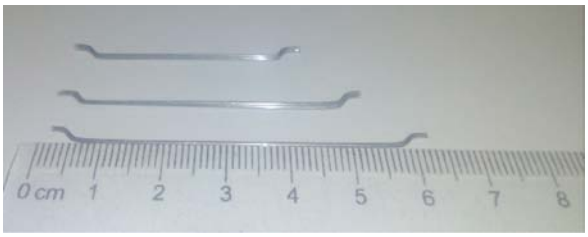

Figure 8: Hooked End Steel Fiber Used

For this, thirty mixes were prepared to fabricate two types of specimens of cylinders in addition to prisms. The test results observed that the mechanical properties of SFRC are affected by the parameters used in this study, as the compressive and tensile strengths improved about 10-25% and 31-47%, respectively. But the higher effect on the flexural strength of SFRC; especially the increase in the steel fiber content from 0.5% to 1.5% at 65 aspect ratio where an increase appeared about 3-124%, and also increased to 140% at 80 of aspect ratio (the highest) as compared to the ordinary concrete.

H. Yang et al., 2018[17] were experimentally comparative the flexural response of concrete between HSFRC and HSC that a series of mechanical properties were investigated. In this study straight steel fibers (as shown in Figure 9) were used which had a diameter and length of 0.2 and 19.5 mm, respectively that adding to the concrete mix by 1% of volume fraction. Three rebar ratios were prepared of 0.98, 1.47, and 1.97 to fabricate the beams. Test results showed that, Although the influence of the high rebar ratio was evident on the increase in mechanical properties of concrete, the cracks stiffness of HSFRC gave a much higher rate (almost doubled) compared to HSC that attributed to the fiber addition purely. The researchers calculated the cracks stiffness of concrete depending on the following equation (Equation 4):

$$\text{Crack Stiffness} = \frac{yield\ load\ (P_y) - cracking\ load(P_{cr})}{deflection\ coinciding\ to\ P_y\ -\ deflection\ coinciding\ to\ P_{cr}} \quad (4)$$

Figure 9: Straight Steel Fibers used

Avanaki et al., 2018[18] published a study that aimed to investigate the effect of different steel fiber content in addition to their aspect ratio to the hybrid FRC by compared the various engineering propertied experimentally. Two types of steel fiber were utilized: Hooked ends (Macro fibers) have 50 mm length and a diameter of 0.8 mm. Flattened ends (Microfibers) have 13 mm in length and a diameter of 0.17 mm. The used fibers are shown in Figure 10. Six hybrid concrete mixes

prepared by different volume fraction as a macro fiber/microfiber ratio of 0.5/0, 3/0.5, 0.3/0.3, 0.5/0.5, 0.5/0.3 and 0.3/0.5.

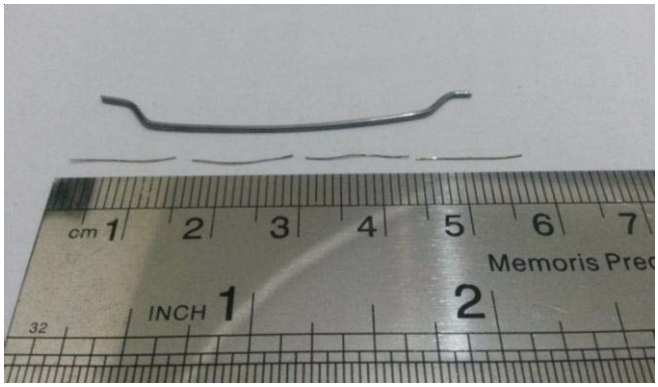

Figure 10: Micro and Macro Steel Fiber used

The tests results showed that both sizes of steel fibers supplied an increase of compressive strength and tensile strength of concrete with a greater positive effect of ultimate flexural load capacity and toughness due to making a better bridging technique in the concrete matrix.

Iqbal et al., 2019[19] investigate and compare the performance of concrete reinforced by different geometries of steel fiber where concrete properties were considered at fresh and hardened statuses. So that, two types of steel fiber were included in the concrete mix of straight steel fiber (SSF) and closed steel fiber (CSF). Due to the unavailability of both types of CSF and SSF in the market (according to the authors), they have been handmade in the laboratory by cutting a steel mesh 17×17 mm to get both steel fibers as displayed in. Based on the results that emerged from the tests, with the increase of fiber content the workability of concrete decreases wears no noticeable changes were recorded for the compressive resistance and modulus of elasticity. On the other hand, the addition of CSF supplied about 46% and 36% in tensile and flexural strengths, respectively, over the concrete reinforced by SSF.

Figure 11: Steel Fiber Used that Cut Manually

Gumus & Arslan, 2019[20] investigated the effect of fiber on the flexural behavior of high RC beams with low reinforced ratio experimentally. Steel fiber is incorporated into the concrete at a different volume fraction of 0.33, 0.66, and 0.99%. Hooked ends steel fibers were used (30 mm length and 0.55 mm diameter). Twelve rectangular RC beams of 150mm width; 200 mm high and 1200 mm span were tested under the four-point loading test. The results showed that

the yielding load has been increased when the steel fiber content increased and this improvement has been attributed to the better mechanical interlock between the fiber and concrete after the cracking stage. Figure 6 illustrated the mechanical interlock of SFRC.

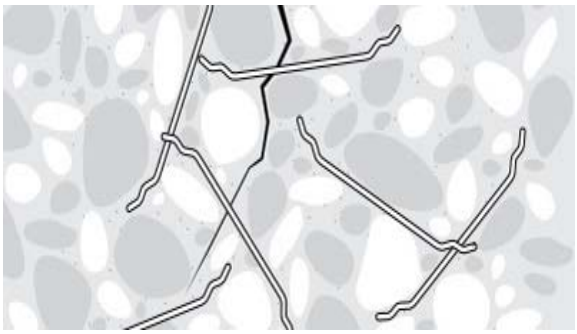

Figure 12: Mechanical Interlock of SFRC

Zhong et al., 2021[21] proposed a theoretical model to investigate the effect on flexural strength of replacement conventional steel reinforcement bars by steel fiber. The study had theoretical and laboratory methodologies. DRAMIX® 4D product of steel fiber was used in the study which has a total length of 60 mm and a diameter of 0.9 mm.

Three volume fractions of steel fiber were adopted of 0, 0.75, and 1.5%. The standard tests procedures have been applied to determine the mechanical properties of the concrete mix. The experimental results displayed that, as expected, the increase of steel fiber volumes observed a greater ductility behavior and toughness. In addition, the functions between fiber dosages and compressive strength of SFRC were inconsistent.

Otherwise, the ultimate strength improved proportionally to the steel fiber content. Where, for 0, 0.75 and 1.5% of steel fiber content the maximum loads recorded during the four-point loading test of specimens were 27.7, 49.9, and 65.2 kN respectively.

III. AGREEMENTS AND DISAGREEMENTS BETWEEN THE ABOVE PREVIOUS STUDIES

Some configurations crossed throughout the previous studies mentioned above. This section briefly reviews the similarities and differences between them, where:

- The above previous studies agreed to have a general topic, which was using an amount of fiber to have an improvement in the mechanical properties of concrete.
- Many previous studies unified by the parameters used, which were the fiber content (as either volume fraction or dosage) or the geometry of fiber and in some studies, the parameters included the concrete grade or w/c ratio.
- All of the previous studies applying an experimental program to obtain the results.
- Always, the previous study depended on the four-point load test to provide the experimentally results for obtaining the flexural behavior of FRC.
- Many previous studies have dealt with the effect of adding fiber on the compressive and tensile strength of concrete by using steel fiber.

IV. COMMENT ON PREVIOUS STUDIES

The previous studies investigated the effect of added fiber on the mechanical properties of RC beams; thus, the collected results are as following:

- *Compressive Strength*: Many studies agreed that no noticeable changes were revealed for the compressive strength of concrete as a result of adding steel fibers [4], [10], [12], [19], [21]. As well as, other studies concluded a slightly improving in the compressive strength of concrete less than 10% as compared with concrete with no fiber [3], [8], [16], [18],; expected of [1] about 15% and [16] about 10-25% depends on the parameters used. Whereas, some studies have proven that

adding fiber more than 1% of the volume fraction led to reducing the compressive strength of concrete gradually due to balling effect [14], [15].

- *Toughness:* A lot of previous research unified by the concept that using fiber with concrete mix improved the toughness of concrete matrix especially with high content and length of fiber attributed to making a better bridging technique inside the concrete at service state [1], [2], [7], [10], [21].
- *Splitting Tensile Strength*: Although, the addition of steel fibers have a clear effect in improving the splitting tensile strength as compared to the traditional concrete whenever the content of fiber increased [10], [18]. Meaning, by using steel fiber this improvement ranged from 40-98% [1], [3], [19].
- *Flexural behavior*: the flexural strength of FRC have been increase as the volume fraction of fiber increased due to the higher number of fiber in cross-section [5], [10], [12]–[14], [16], [19]. Where, it was possible to reach up about 140% [16].
- *Ductility:* The increase of steel fiber dosages resulted in a greater ductility behavior[21].
- *Workability*: At a fresh state, adding fiber at low levels provided better flowability with no bleeding or segregation. Meanwhile, the high fiber dosage observed a much lower value of slump. Thus, the workability decreased significantly due to more air content in the mixture by balling fiber [8].
- *Ultimate load:* The concrete performance was responded to a positive effect of ultimate flexural load capacity by including fibers proportionally to the volume fraction [2], [18], [21].

V. THE BENEFIT OF PREVIOUS STUDIES

Undoubtedly, this study has been benefited from the previous studies in several aspects. Therefore, it can employ many previous efforts to reach an accurate definition of the scientific gap and thus be addressed it comprehensively, including:

- Access to an exact formulation of the study title.
- Determine the suitable technique for a future study.
- Apply the suggestions and recommendations of the previous studies and use them to support a future study.
- Checking an experimental result of a future study recorded to be nearly the expected.
- Gaining a scientific background to knowledge the FRC performance.
- Specify the parameters for the conducted study then select the adequate one.
- Dependence the tests method of ASTM code that helps to select the dimensions of RC beams used in a future study.

VI. THE KNOWLEDGE GAPS

In the light of the brief review, it can be seen that:

- The previous effort has mainly focused on some important parameters such as volume fraction and geometry of fiber and concrete grade.
- In most of these studies, in addition, the common conclusion reached is that fiber can only enhance the tensile strength and has no, or tenuous, effect on the compressive strength of concrete.

This conclusion leads to an important question is that why fiber would be added to the parts of the structural member subjected to compressive stresses when it can be omitted in such parts, especially that implementing fiber is expensive, reduces the workability, and therefore, consumes more time and labor to produce concrete.

ACKNOWLEDGMENTS

The authors would like to acknowledge the contribution of Thi-Qar Oil Company (South of Iraq) for allowing the research team to perform the necessary search for this research.

REFERENCES

1. P. S. Song and S. Hwang, "Mechanical properties of high-strength steel fiber-reinforced concrete," *Constr. Build. Mater.*, vol. 18, no. 9, pp. 669–673, 2004, doi: 10.1016/j. conbuildmat.2004.04.027.

2. F. Altun, T. Haktanir, and K. Ari, "Effects of steel fiber addition on mechanical properties of concrete and RC beams," *Constr. Build. Mater.*, vol. 21, no. 3, pp. 654–661, 2005, doi: 10.1016/j.conbuildmat.2005.12.006.
3. J. Thomas and A. Ramaswamy, "Mechanical Properties of Steel Fiber-Reinforced Concrete," no. May, pp. 385–392, 2007.
4. F. Bencardino, L. Rizzuti, G. Spadea, and R. N. Swamy, "Stress-Strain Behavior of Steel Fiber-Reinforced Concrete in Compression," *J. Mater. Civ. Eng.*, vol. 20, no. 3, pp. 255–263, 2008, doi: 10.1061/(asce)0899-15 61(2008)20: 3(255).
5. T. Uygunoğlu, "Investigation of microstructure and flexural behavior of steel-fiber reinforced concrete," *Materials and Structures/Materiaux et Constructions*, vol. 41, no. 8. pp. 1441–1449, 2008, doi: 10.1617/s115 27-007-9341-y.
6. B. W. Xu and H. S. Shi, "Correlations among mechanical properties of steel fiber reinforced concrete," *Constr. Build. Mater.*, vol. 23, no. 12, pp. 3468–3474, 2009, doi: 10.1016/j. conbuildmat.2009.08.017.
7. K. Marar, Ö. Eren, and I. Yitmena, "Compression specific toughness of normal strength steel fiber reinforced concrete (NSSFRC) and high strength steel fiber reinforced concrete (HSSFRC)," *Mater. Res.*, vol. 14, no. 2, pp. 239–247, 2011, doi: 10.1590/S1516-14392011005000042.
8. D. V. Soulioti, N. M. Barkoula, A. Paipetis, and T. E. Matikas, "Effects of fibre geometry and volume fraction on the flexural behaviour of steel-fibre reinforced concrete," *Strain*, vol. 47, no. SUPPL. 1, pp. 535–541, 2011, doi: 10.1111/j.1475-1305.2009.00652.x.
9. K. Sasikala and D. S. Vimala, "A Comparative Study Of Polypropylene, Recron And Steel Fiber Reinforced Engineered Engineered Cementitious Composites," vol. 1, no. 10, pp. 46–54, 2013.
10. V. S. Vairagade and K. S. Kene, "Introduction To Steel Fiber Reinforced Concrete on Engineering Performance of Concrete," *Int. J. Sci. Technol. Res.*, vol. 1, no. 4, pp. 139–141, 2012.
11. J. R. Deluce and F. J. Vecchio, "Cracking behavior of steel fiber-reinforced concrete members containing conventional reinforcement," *ACI Struct. J.*, vol. 110, no. 3, pp. 481–490, 2013, doi: 10.14359/51685605.
12. L. Rizzuti and F. Bencardino, "Effects of fibre volume fraction on the compressive and flexural experimental behaviour of SFRC," *Contemp. Eng. Sci.*, vol. 7, no. 5–8, pp. 379–390, 2014, doi: 10.12988/ces.2014.4218.
13. D. Y. Yoo, N. Banthia, J. M. Yang, and Y. S. Yoon, "Size effect in normal- and high-strength amorphous metallic and steel fiber reinforced concrete beams," *Constr. Build. Mater.*, vol. 121, pp. 676–685, 2016, doi: 10.1016/j.conbuil- dmat.2016.06.040.
14. D. A. Sinha and A. K. Verma, "An Experimental Investigation on the Effect of Addition of Ternary Blend on the Mix Design Characteristics of High Strength Concrete using Steel Fibre," *IOP Conf. Ser. Mater. Sci. Eng.*, vol. 225, p. 012163, 2017, doi: 10.1088/1757- 899x/225/1/012163.
15. D. Sinha and A. Verma, "Investigation on the Effect of Varying Dosages of Steel Fibre on the Strength and Workability Properties Of High Strength Concrete," vol. 1, pp. 352–346, 2018, doi: 10.29007/rjbd.
16. W. Abbass, M. I. Khan, and S. Mourad, "Evaluation of mechanical properties of steel fiber reinforced concrete with different strengths of concrete," *Constr. Build. Mater.*, vol. 168, pp. 556–569, 2018, doi: 10.1016/j.conbuildmat.2018.02.164.
17. I. H. Yang, C. Joh, and K. C. Kim, "A Comparative Experimental Study on the Flexural Behavior of High-Strength Fiber-Reinforced Concrete and High-Strength Concrete Beams," *Adv. Mater. Sci. Eng.*, vol. 2018, 2018, doi: 10.1155/2018/7390798.
18. M. J. Avanaki, Im. Abed, A. Hoseini, and M. S. Maerefat, "Effects of Fiber Volume Fraction and Aspect Ratio on Mechanical Properties of Hybrid Steel Fiber Reinforced Concrete," *J. New Approaches Civ. Eng.*, vol. 2, no. 2588–6886, pp. 49–64, 2018.
19. S. Iqbal, I. Ali, S. Room, S. A. Khan, and A. Ali, "Enhanced mechanical properties of fiber reinforced concrete using closed steel fibers,"

Mater. Struct. Constr., vol. 52, no. 3, pp. 1–10, 2019, doi: 10.1617/s11527-019-1357-6.
20. M. Gumus and A. Arslan, "Fiber type and content vs flexural strength-Mohammed 2019. pdf." 2019.
21. A. Zhong, M. Sofi, E. Lumantarna, Z. Zhou, and P. Mendis, "Flexural Capacity Prediction Model For Steel Fibre-Reinforced Concrete Beams," *Int. J. Concr. Struct. Mater.*, vol. 15, no. 1, 2021, doi:10.1186/s40069-021-00461-0.

Reliability of the Bond Graph Approach for Robust Diagnosis of a Newborn Incubator System

Abderrahmene Sellami, Zermani Mohamed Aymen, Elyes. Feki & Abdelkarim. Mami

Université de Tunis

ABSTRACT

This article aims to solve a problem of research with a thermal system (incubator) to the graph of pseudo-connections. The method we develop is based on the determination of the resolution on the model ARR-BGM (Analytical Redundant Relationships Bond Graph). These relationships serve to detect and isolate faults in the various elements of the system, but also to locate the industrial system. We introduced defects in the heat source, leaks in the incubators and a leak in the incubator door; these defects were transferred by thermal transfer to negative values. The results of simulation, the effectiveness of proposed method to detect and locate defects, in addition, to analyze the robustness of the Incubator to defects, we imported the graphical link model as linear fractional transformations (BG-LFT). This makes it possible to verify the reliability of the approach of the link graphs in terms of sensitivity and detectability of defects that may appear in an industrial system.

Keywords: robust diagnosis, bond graph approach, linear fractional transformations, analytical redundancy relations, incubator.

Classification: LCC Code: T58.5

Language: English

Great Britain Journals Press

LJP Copyright ID: 392924
Print ISSN: 2631-8474
Online ISSN: 2631-8482

London Journal of Engineering Research

Volume 24 | Issue 1 | Compilation 1.0

Reliability of the Bond Graph Approach for Robust Diagnosis of a Newborn Incubator System

Abderrahmene Sellami[α], Zermani Mohamed Aymen[σ], Elyes. Feki[ρ] & Abdelkarim. Mami[Ↄ]

ABSTRACT

This article aims to solve a problem of research with a thermal system (incubator) to the graph of pseudo-connections. The method we develop is based on the determination of the resolution on the model ARR-BGM (Analytical Redundant Relationships Bond Graph). These relationships serve to detect and isolate faults in the various elements of the system, but also to locate the industrial system. We introduced defects in the heat source, leaks in the incubators and a leak in the incubator door; these defects were transferred by thermal transfer to negative values. The results of simulation, the effectiveness of proposed method to detect and locate defects, in addition, to analyze the robustness of the Incubator to defects, we imported the graphical link model as linear fractional transformations (BG-LFT). This makes it possible to verify the reliability of the approach of the link graphs in terms of sensitivity and detectability of defects that may appear in an industrial system.

Keywords: robust diagnosis, bond graph approach, linear fractional transformations, analytical redundancy relations, incubator.

Author α: Laboratoire d'Application de l'Efficacité Énergétique et des Énergies Renouvelables-LAPER, Faculté des Sciences de Tunis, Université de Tunis El Manar Campus Universitaire Farhat Hached, 1068 Tunis, Tunisie.

σ: Laboratoire d'Application de l'Efficacité Énergétique et des Énergies Renouvelables-LAPER, Faculté des Sciences de Tunis, Université de Tunis El Manar Campus Universitaire Farhat Hached, 1068 Tunis, Tunisie.

ρ: Laboratoire d'Application de l'Efficacité Énergétique et des Énergies Renouvelables-LAPER, Faculté des Sciences de Tunis, Université de Tunis El Manar Campus Universitaire Farhat Hached, 1068 Tunis, Tunisie.

Ↄ: Laboratoire d'application de l'efficacité énergétique et des énergies renouvelables, Faculté des Sciences de Tunis University of Tunis el Manar Campus Universitaire El Manar, 2092 Tunis, Tunisia.

I. INTRODUCTION

The main objective of the automation engineer is to determine control algorithms of physical systems that are often of different natures, electrical, mechanical, hydraulic, thermal, etc. This objective will not be obtained if the system modeling is not validated which is the first task. The model describing physical reality is usually obtained on the basis of an idealized description of the system and only dominant phenomena are often taken into account given the complexity and diversification of the system [1-4].

In this article we chose the incubator not only for the complexity of the system but also the importance of this system in the lives of human beings. An incubator is a protected heated place, which allows the development and monitoring of certain newborns. It is an apparatus intended to allow the normal development of children born before term (premature), or fragile newborns [5-10].

The incubators consist of an electrical part (electrical heating resistance) and a thermal part (enclosure receiving the child). Several elements of the incubator can be a source of contamination of the environment of the newborn. Indeed, each part constituting the incubator has specificities for cleaning, disinfection and maintenance. In addition, disinfection is a priority of neonatology

units [11], but maintenance (sealing problem, problem of thermal insufficiency or overheating) is a task for technicians [12-15]. To facilitate the task of the technicians, it is necessary to find a reliable and generous approach to model and analyze the defects that may appear during operation this incubator. This reliability and generosity can be found in several approaches such as Petri nets [16-24] and bond graph [25-30].

Most authors have limited their research to a mathematical model to simulate the different heat exchanges in the incubator or for control purposes..: Ultman [31] developed a simulator of neonatal energy transfer to provide a convenient yet precise comparison of sensible heat loss in incubators, Le BIanc [32] described the fundamental equations involved in thermal exchange between infants and their environment. Simon [33] developed a Theoretical Model of Infant Incubator Dynamics. Pauline Décima[34] developed a Mathematical modeling of thermoregulation processes for premature infants in closed convectively heated incubators and for calculating thermo neutrality in closed incubators for premature newborns, Zermani [35] developed a simulation model of infant-incubator system with decoupling predictive controller, Andrés Fraguela [36] Proposed a model of heat exchange and energy balance in premature newborns during the first hours of life in a closed incubator. In addition, a control problem was proposed and solved in order to maintain thermal stability of premature. Stéphane Delanaud [37] proposed a New Software for assessing the impact of humidity on the optimal incubator air temperature.

The bond graph approach is a very effective approach for this kind of system, since it is multidisciplinary and was initially used for modeling physical systems. The usual approach of the users of this approach is to consider the bond graph model as a knowledge model for the simulation of dynamic systems. The idea of using a single representation (the bond graph) for the modeling, analysis and synthesis of control laws by exploiting causality has been developed in this field [38, 40].

Engr Hassan Javed and Asif Mahmood Mughal [41] have developed a flow chart model for an incubator that only takes into account the heating part modeled as heating capacity, then the heat flux in the chamber is modeled as a flux source, but they neglected the thermal capacity of the external environment and the thermal capacity of the mattress. In this paper we propose a new approach of modeling by the bond graph approach of the incubator taking into account the thermal capacities of the environment as well as the mattress.

The purpose of this article is also to design a robust diagnostic system based on a model using a single tool: the link graph. Methodologically, the work consists of automating model generation and failure indicator procedures in the form of fractional linear transformations (LFTs) and interchangeably for integration into the supervisory system. At the industrial level, the results obtained were applied to real installations: incubator.

II. MATHEMATICAL MODEL OF THE INCUBATOR

The incubator can be described as a reaction system consisting of two large dynamic parts: the climate inside the lodge and the heating system. The heat, humidity and oxygen at the thermostat outlet are defined as input variables of the incubator and the climate parameters tested by the newborn are the output variables. The temperature of the box, the temperature of the walls and the windows intended for medical care, the incubator consists of three main parts:

- The ambient air in the lodge
- The mattress;
- The walls.

2.1 Modeling the Thermostat

To model this part of the incubator, consider the following simplifying measures:

- The thermostat is assumed to be homogeneous with constant characteristics such as specific heat
- The temperature distribution is uniform,
- The specific heat C_{pm} is equal to that of the normal air.

The temperature of the air coming from the thermostat can be written as follows:

$$\frac{dT_{ha}}{dt} = \frac{(T_{hai} - T_{ha})}{C.R_{pm}} \quad (1)$$

2.2 The Ambient Air in the Lodge

The ambient air of the incubator box exchanges heat with all the elements of the Child-incubator system mainly by convection, but also by mass transfer during the Breathing and also by evaporation. In our case we consider the incubator without baby. During a period dt, the thermal equilibrium of the ambient air of the box can be determined according to the following equation:

$$\frac{dT_a}{dt} = \frac{Q_{ht} - Q_{acv} - Q_{mat}}{M_a.C_{pa}} \quad (2)$$

Where M_a denotes the air mass in the box and C_{pa} its thermal capacity.

The ambient air of the box gives heat to the walls of the incubator by convection. This energy is determined by the following equation:

$$Q_{acv} = h_{acv}.A_w.(T_a - T_w) \quad (3)$$

Where A_w is the surface of the walls in contact with the air. The convective transfer coefficient h_{acv} depends mainly on the shape of the incubator, the ventilation in the box and the number of Nusselt and Reynold.

The mattress surface of the incubator not occupied by the child also exchanges the energy with the convective ambient air according to the following equation:

$$Q_{mat} = h_{acv}.A_{net}.(T_a - T_m) \quad (4)$$

Where A_{net} is the surface of the mattress in contact with the air.

2. 3 Thermal Balance of the Walls

The walls of the incubator, made of transparent Plexiglas, have six portholes and a window provided for care. The walls consist of a single homogeneous layer thw thickness equal to 6mm and the heat distribution is uniform on the inner surface and external.

The thermal equilibrium during a time dt can be written in the following way:

$$\frac{dT_w}{dt} = \frac{Q_{acv} - Q_{cv0} - Q_{r0}}{M_w.C_{pw}} \quad (5)$$

Where Mw the total mass of plexiglass walls and C_{pw} its thermal capacity.

The inner surface of the incubator wall receives convective heat loss from the ambient air in the incubator Qacv.

On the other hand, the walls of the incubator exchange with the neonatology room of radiation and convection energy. The convective heat transfer is determined by the equation below:

$$Q_{cv0} = h_{cv0}.A_{wt}.(T_w - T_e) \quad (6)$$

The heat transfer by radiation is calculated by the following relation:

$$Q_{r0} = A_{wt}.\delta.\xi_w[(T_w + 273.15)^4 - (T_e + 273.15)^4] \quad (7)$$

2. 4 Mattress Modeling

The mattress of the incubator exchanges heat by conduction of the ambient air and skin conduction. In the case of an empty incubator the thermal equilibrium of the mattress can then be written in the same way next:

$$\frac{dT_m}{dt} = \frac{Q_{mat} - Q_{ic}}{M_m.C_{pm}} \quad (8)$$

Knowing that the two plates of the support that carries the mattress are thin, and the surface of small contact, the transfer of heat by conduction

London Journal of Engineering Research

of the mattress to the incubator, Q_{ic}, is not considerable and can be ignored.

III. INDUSTRIAL SYSTEM BY BOND GRAPH MODELS

The bond graph formality was introduced by H. Paynter in 1961 [42] and formalized by Karnopp and Rosenberg in 1975 [43]. The bond graph tool is now used regularly in a few companies, particularly in the automotive industry (PSA, Renault, Ford, Toyota, General Motors, etc.). This method illustrates energy transfers in the system using power bonds. A power link is symbolized by a half arrow, whose orientation indicates the direction of power transfer. Thus, figure 1 shows the power transfer from subsystem S_1 to subsystem S_2 [44-46]. One of the fundamental characteristics of the bond graph formalism is its unifying aspect, whatever the physical domain of application (electrical, mechanical, hydraulic, chemical...). We can visualize energy transfers in multi-domain systems using the generalized variables presented in the next section. The notion of power is described by the following relation:

$$P(t) = \dot{e}(t).f(t) \quad (9)$$

This equation illustrates energy transfers in the system by using power bonds. A power link[4] is symbolized by a half arrow, whose orientation indicates the direction of power transfer. Thus, figure 1 shows the power transfer from subsystem S_1 to subsystem S_2.

Each power link carries two information's simultaneously: the effort and the flow (see figure 1). These are the generalized power variables (their product being the transferred power).

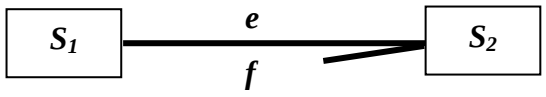

Figure 1: Power link

IV. ROBUST DIAGNOSIS OF INDUSTRIAL SYSTEM BY BOND GRAPH MODELS

Linear Fractional transformations (LFT) are generic objects widely used in the modeling of uncertain systems. The universality of fractional linear transformations is reached seen that any rational expression can be written in this form [47-54]. This form of representation is very used for the synthesis of control laws of uncertain systems using the principle of μ-analysis. It consists of separating the nominal part of a model from its uncertain part, as shown in figure 2.

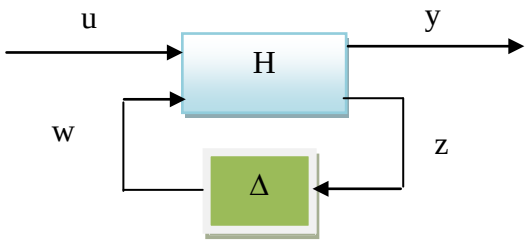

Figure 2: Representation of the Fractional Linear Transformations (LFT)

The nominal values are grouped together in an augmented matrix denoted H, supposed to be proper. The uncertainties whatever their types (structured and unstructured parametric uncertainties, modeling uncertainties, measurement noises, etc.) are combined in a matrix Δ of diagonal structure.
With:

$x \in R^n$: System state vector;
$u \in R^m$: Vector grouping system control inputs;
$y \in R^p$: Vector grouping the measured outputs of the system;
$w \in R^l$ *and* $z \in R^l$: Respectively include inputs and auxiliary outputs. n, m, l and p are positive integers.

4.1. Construction of a BG-LFT Model

All industrial systems can be modeled by BG model according to figure 3. Indeed, the input signal is modeled by an effort source (*Se*) or a flow source (*Sf*). The complete system is modeled by resistive elements (*R*) and storage elements (*I* or *C*), while the detectors are modeled by detector elements (*De* or *Df*).

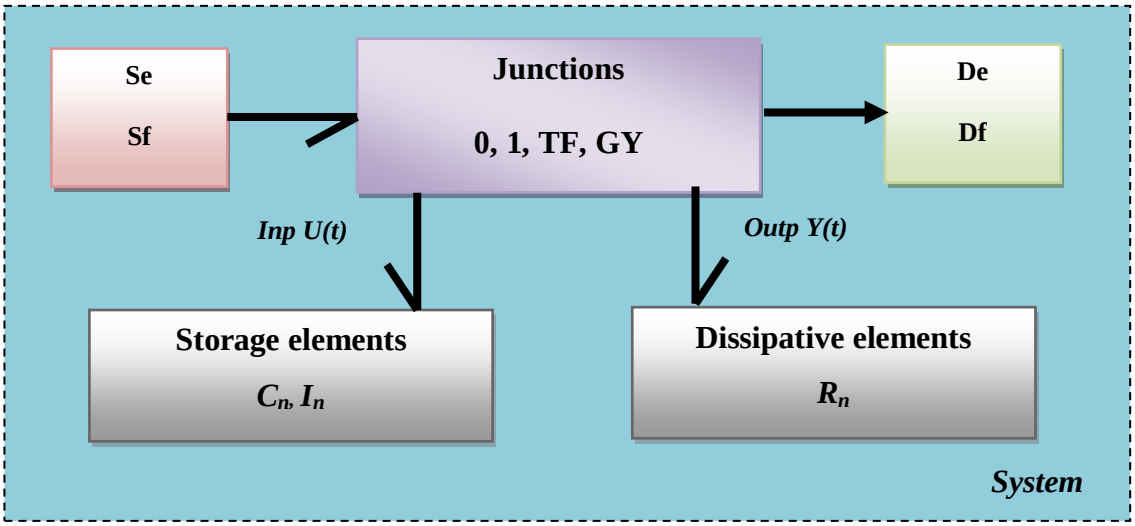

Figure 3: Industrial System Described by Bond Graphs

4.2. Bond Graph Element With Multiplicative Uncertainty

The introduction of a multiplicative uncertainty on e.g. element R in causality gives resistance:

$$e_R = R_n(1+\lambda_R)f_R = e_n + \lambda_R e_n = e_n + e_{inc} \tag{10}$$

With:

- R_n : The nominal value of the element R;
- λ_R: The multiplicative uncertainty parameter;
- e_R et f_R : Represent respectively the effort and the flow in the element R ;
- e_n et e_{inc} : Respectively represent the effort made by the nominal setting and effort introduced by the additive uncertainty.

Unlike the force introduced by an additive uncertainty with respect to the parameter (equation (1)), the force provided by a multiplicative uncertainty (equation (10)) is a function of the force provided by the nominal parameter. This is an important property for the parametric identification step and the supervision step.

4.3 Resistive Element With a Multiplicative Uncertainty

The bond graph model equivalent mathematical model of equation (2) is given in figure 4.

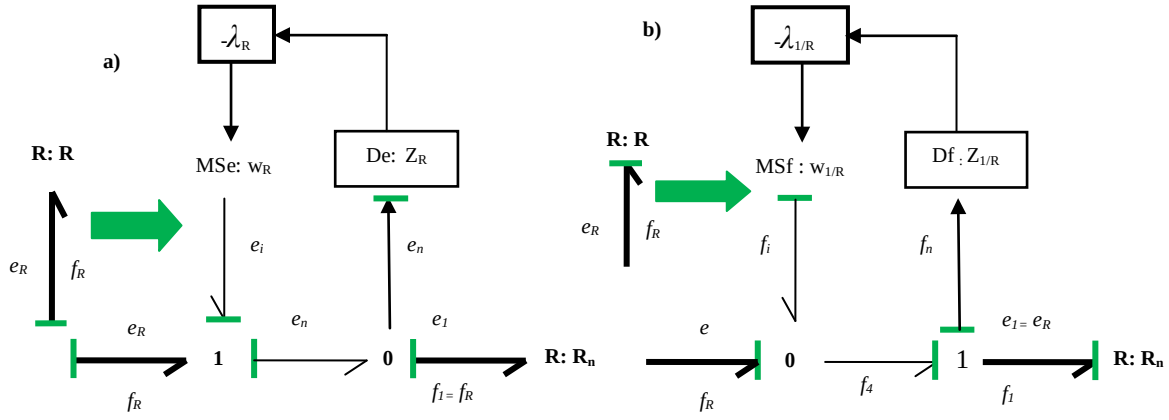

Figure 4: a) BG-LFT Model of an Element Resistance with Multiplicative Uncertainty, b) BG-LFT Model of an Element Conductance with Multiplicative Uncertainty

4.4 Storage Elements With a Multiplicative Uncertainty

- Parts C derived causality

The bond graph model equivalent mathematical model of equation (2) is given in figure 5.

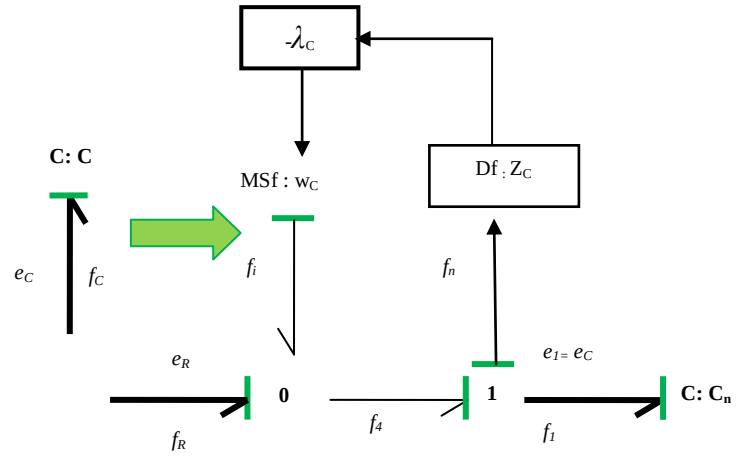

Figure 5: BG-LFT Model of an Element *C* in Derivative Causality With Uncertainty

- Parts C Integral Causality

The bond graph model equivalent mathematical model of equation (2) is given in figure 6.

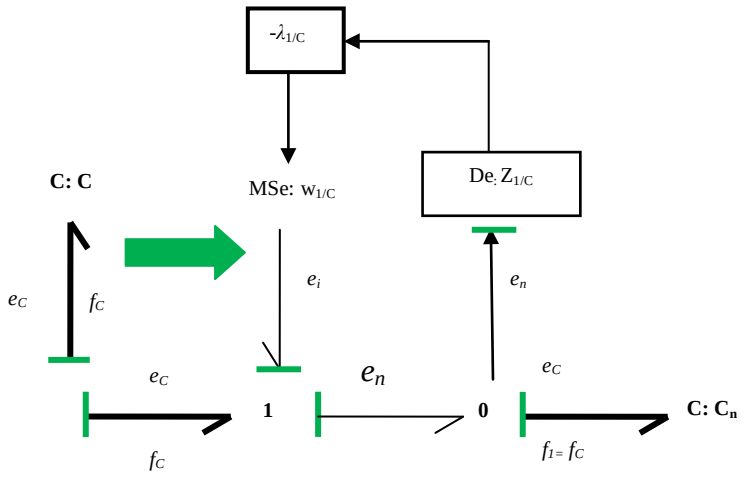

Figure 6: a) BG-LFT Model of an Element C in Integral Causality with Multiplicative Uncertainty

To determine the final model that fits the model of a physical system by the Bond Graph approach and the Linear Fractional transformations model, we must integrate according to the following figure 7.

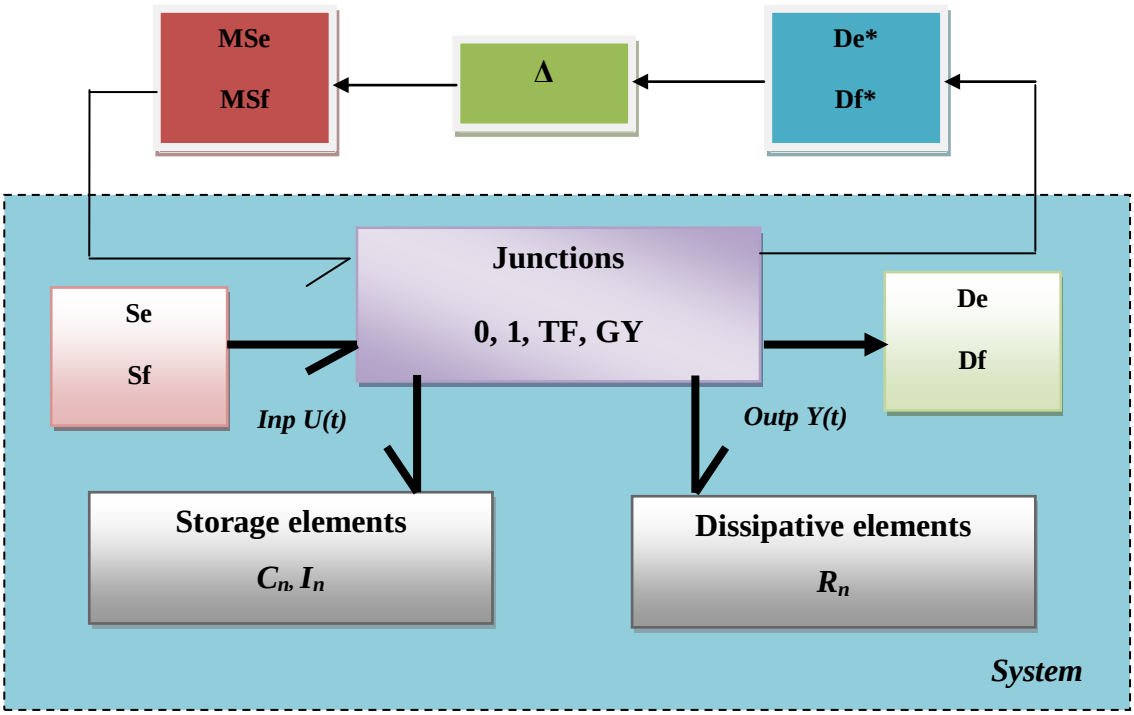

Figure 7: BG-LFT Model for Physical System

4. 5 Generation of Robust Residuals

To determine the residuals by the redundant analytical relationship (*ARR*), the following steps must be followed:

- *1st phase*: Determining the derivative model;
- *2nd phase:* Determining the graph model using the LFT transform;
- *3rd phase:* Determining the residual equations for the two junctions (0 and 1).

For a 0-junction:

$$\sum f_{inc} + \sum Sf + \sum w_i \qquad (11)$$

For a 1-junction:

$$\sum e_{inc} + \sum Se + \sum w_i \qquad (12)$$

With, e_{inc} and f_{inc} are unknown variables. Moreover, the sum of flow sources and the sum of the effort sources are respectively performed at the level of the 0-junction and the 1-junction.
then determine the residue equations at their junctions.

$$ARRs : \Phi(\sum Se, \sum Sf, De, Df, \sum w_i, R_n, I_n, C_n, TF_n, GY_n) \qquad (13)$$

where

TF_n and Gy_n are nominal elements *TF* and *GY*.
R_n, C_n, and I_n are nominal elements *R*, *C* and *I*.

$\sum w_i$ are uncertainties on the junction-related items.

V. ANALYSIS OF RESIDUALS SENSITIVITY

The methods of analysis of sensitivity to uncertainties and defects is proposed to improve diagnostic performance has been developed in recent years [68-70]. Indeed, these methods are unfortunately not effective for the generation of residues since they neglect the inter-parametric correlation (the thresholds are often overvalued and may differ). In addition, the Bond Graph tool provides an effective solution to the problem of parametric dependencies since the generation of bond graph using (BG-LFT) automatically separates the residuals and the adaptive thresholds, this separation clearly showing the energy contribution of the uncertainties to the indicators of defects and facilitating their assessments in the decision stage by calculating the adaptive thresholds of normal operation. The diagnostic performance is controlled by an analysis of the sensitivity of the residues to uncertainties and defects. To improve diagnostic performance, determine the indices performance (sensitivity index and detectability index) [55].

5.1 Sensitivity Index (SI)

The index of parametric standardized sensitivity explained the evaluation of the energy provided by the residue uncertainty on each parameter by comparing it with the total energy provided by all uncertainties.

$$SI_n = \frac{|w_i|}{d_n} \quad (14)$$

- d_i: Uncertainty on the parameters
- i : Basic element bond graph model (R, C, I, TF and GY)
- w_i: Modulated entry for Uncertainty in the *parameters*

5.2 Detectability Index (DI)

The detectability index represents the difference between the efforts (or streams) provided by defects in absolute terms and that granted by all the uncertainties in absolute value.

- Junction 1

$$DI = |Y_i \| e_{in}| + |Y_s| \quad d \quad (15)$$

- Junction 0

$$DI = |Y_i \| f_{in}| + |Y_s| \quad d \quad (16)$$

While defects detectability conditions will be:

- The defect is not detectable: $DI \leq 0$
- The defect is detectable: $DI \rangle 0$

VI. MODELING AND SIMULATION RESULTS OF INCUBATOR BY BOND GRAPH MODELS

6.1 Incubator System

In this subsection, a simulation model for an incubator was developed. Modeling relies mainly on the conservation of heat and mass. The proposed model is portioned into four distinct homogeneous compartments; incubator air space, heater, wall and mattress (Figure 8).

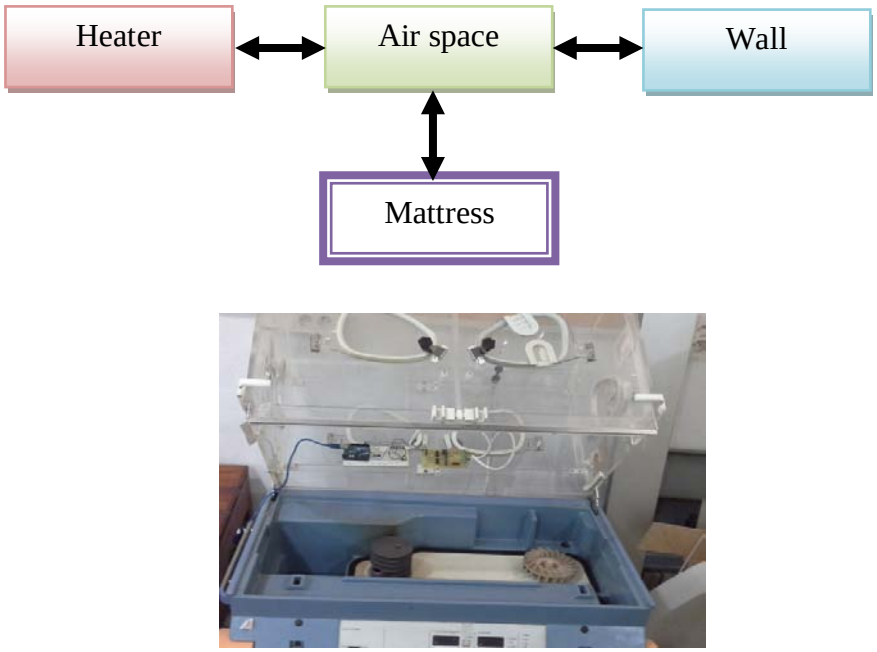

Figure 8: a) Compartments of the Closed Incubator System, b) Actual Image of the Incubator

6.2 Bond Graph Model

The incubator illustrated in figure 9 is modeled by the bond graph of figure 3 as follows:

- ★ The thermal capacity of an electrical resistor is modeled by a source of effort (Se: Te) with a capacitance (C: C_h) in series with a restriction (R_h);
- ★ The thermal capacity in the interior of the incubator by a capacitance (C: C_a) in series with a restriction (R_a);
- ★ The thermal capacity in the outside of the incubator by a capacitance (C: C_w) in series with a restriction (R_w);
- ★ The thermal capacity created by mattress by a capacitance (C: C_m) in series with a restriction (R_m);
- ★ The element (TF_1) represents the thermal transformation between the thermal source and the internal volume of the incubator.
- ★ The element (TF_2) represents the thermal transformation between the thermal source and the mattress.
- ★ The external environment is modeled by a source of effort (Se: T_{ex}) and restriction (R: Rex).

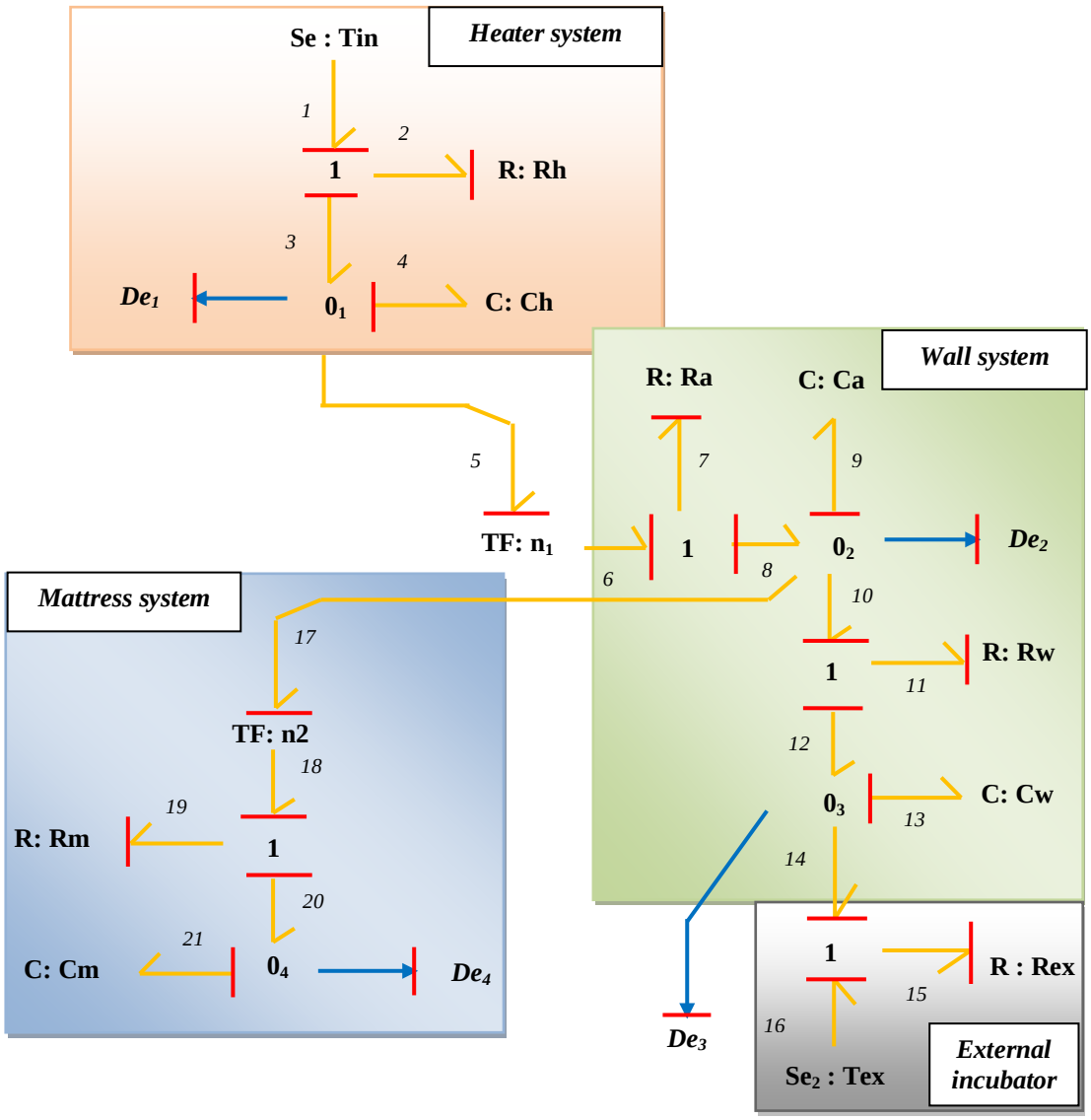

Figure 9: Bond Graph model of Incubator Technology

6. 3 Simulation Results of the Incubator

Figure 10 shows the evolution of temperature curves Th, Ta, Tw and Tm in the case of normal operation.

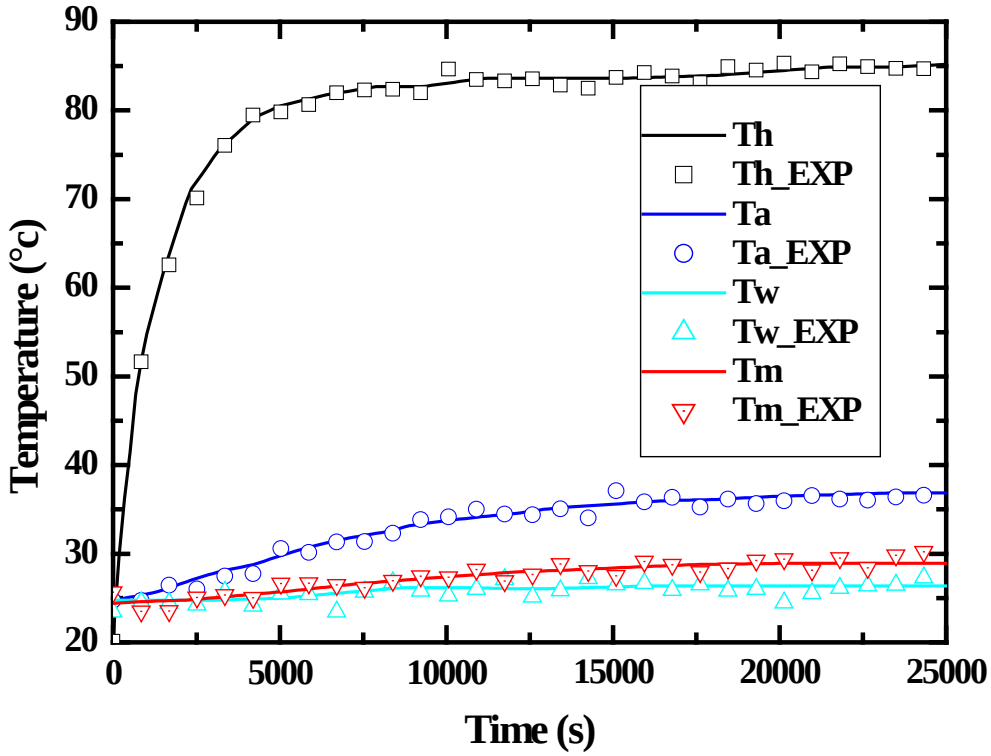

Fig. 10: Evolution of Temperature Curves Th, Ta, Tw and Tm in the Case of Normal Operation

- Determination of residue equations

❖ *The junction o_1 gives us as equation:*

$$r_1 = f_3 - f_4 - f_5$$

According to these relations, one can deduce the residual equation r_1:

$$r_1 = \frac{T_{inp} - De_1}{Rh} - Ch.\frac{dDe_1}{dt} - \frac{n_1.(n_1.De_1 - De_2)}{Ra} \quad (17)$$

❖ *The junction o_2 gives us as equation:*

$$r_2 = f_8 - f_9 - f_{10} - f_{17}$$

According to these relations, one can deduce the residual equation r_2:

$$r_2 = \frac{n_1.De_1 - De_2}{Ra} - Ca.\frac{dDe_2}{dt} - \frac{n_2.(n_2.De_2 - De_{''})}{Rw} - \frac{n_3.(n_3.De_2 - De_3)}{Rm} \quad (18)$$

❖ *The junction o_3 gives us as equation:*

$r_3 = f_{12} - f_{13} - f_{14}$

According to these relations, one can deduce the residual equation r_3:

$$r_3 = \frac{De_2 - De_3}{Rw} - Cw\frac{dDe_3}{dt} - \frac{De_3 - T_{ex}}{R_{ex}} \quad (19)$$

❖ *The junction o_4 gives us as equation:*

$$r_4 = f_{20} - f_{21}$$

According to these relations, one can deduce the residual equation r_4:

$$r_4 = \frac{n_3.(n_3.De_2 - De_4)}{Rm} - Cm\frac{dDe_4}{dt} \quad (20)$$

The default signature matrix is associated with the set of residues (r_1, r_2, ... r_n) with the elements associated with the system (F_1, F_2, ..., F_n). We denote the value M = 1 if the residual i is sensitive to this

element, the opposite case M = 0, in the end we obtain the following signatures the table represented below. In our case, we have (4) four residues (17) seventeen elements.

Table 1: Fault Signatures Matrix for the Incubator

	r_1	r_2	r_3	r_4
F_1: Tin	1	0	0	0
F_2: Tex	0	0	1	0
F_3: Ch	1	0	0	0
F_4: Ca	0	1	0	0
F_5: Cw	0	0	1	0
F_6: Cm	0	0	0	1
F_7: Rh	1	0	0	0
F_8: Ra	1	1	0	0
F_9: Rw	0	0	1	0
F_{10}: Rm	0	1	0	1
F_{11}: Rp	0	0	1	0
F_{12}: n_1	1	1	0	0
F_{13}: n_2	0	1	0	1
F_{14}: De_1	1	1	0	0
F_{15}: De_2	1	1	1	1
F_{16}: De_3	0	1	1	0
F_{17}: De_4	0	1	0	1

Figure 11 shows the evolution of residues r_1, r_2, r_3 *and* r_4 as a normal function. The pitches of the residues converge towards zero under normal operating conditions.

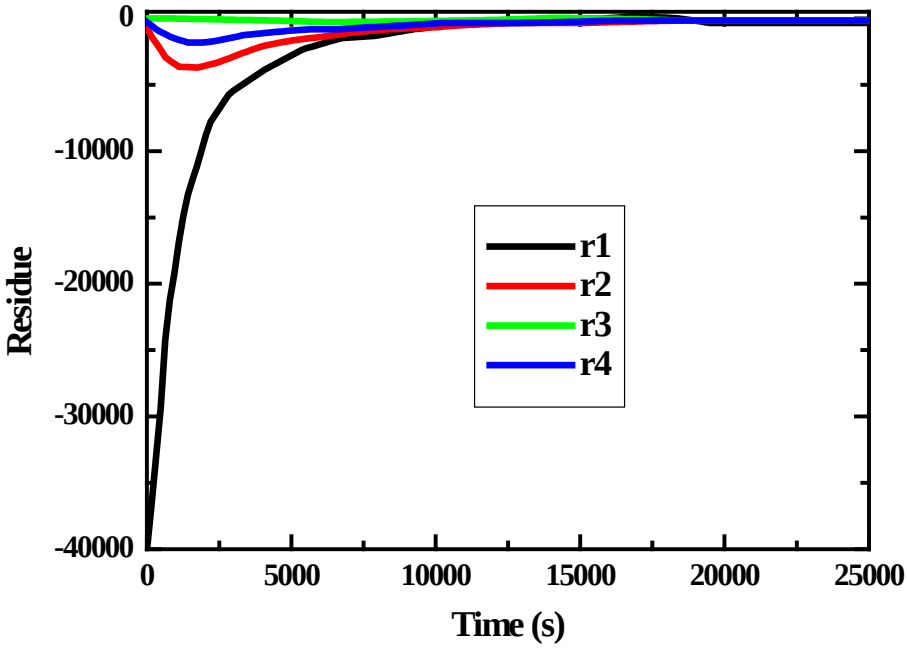

Fig. 11: Evolution of Residues r_1, r_2, r_3 *and* r_4 in the Case of Normal Operation

6. 4 Simulation Incubator With Faults

- *Fault on the Thermal Source*

When a fault occurs on the heat source (damage to the heating resistance of the incubator) at the time t = 12000s, we find that:

★ All the residues r_1, r_2, r_3 and r_4 have non-zero average values, these residues are therefore sensitive to this defect, which is confirmed, by the theoretical results presented in table 2 (see Figure 12).

★ Temperatures *Th, Ta, Tw* and Tm suffered declines in their speed at the moment of failure (see Figure 13).

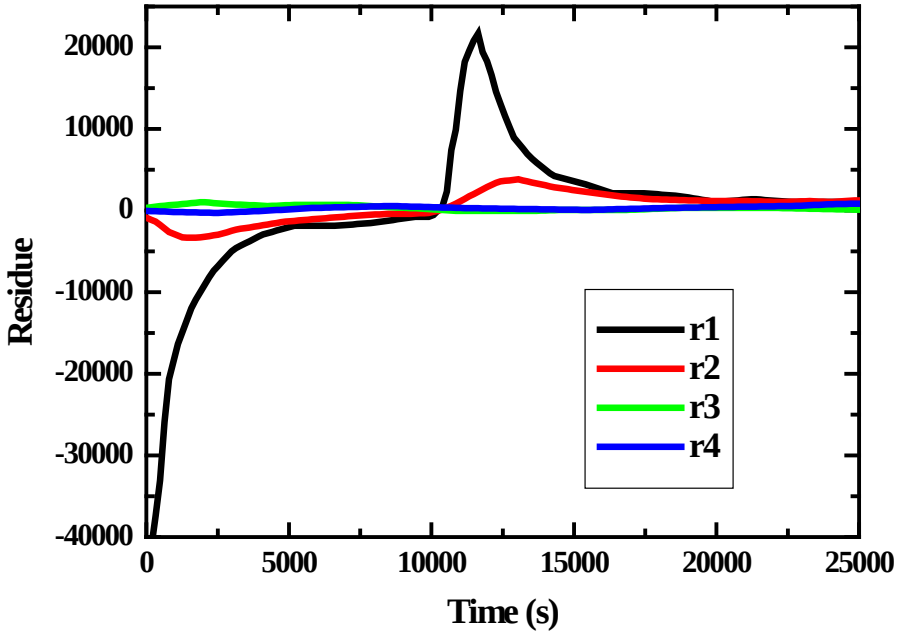

Fig. 12: Evaluation Of Residues r_1, r_2, r_3 and r_4 in the Case of a Fault on the Thermal Source

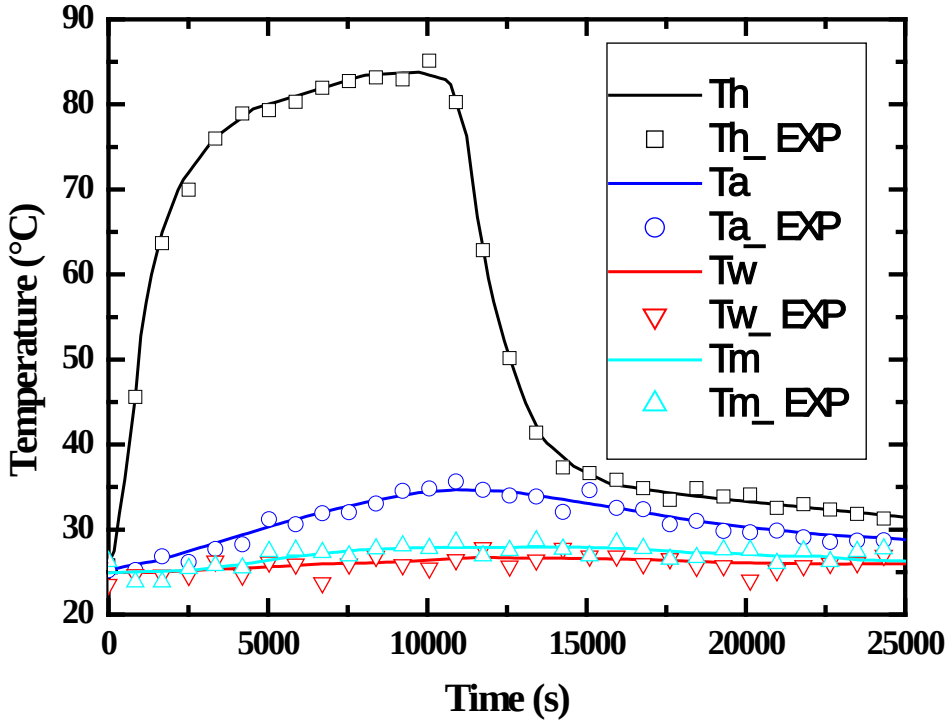

Fig. 13: Evaluation of temperatures *Th, Ta, Tw* and *Tm* in the case of a fault on the thermal source

- Fault inside the incubator

When a fault occurs on the incubator (open door of the incubator) at the time t = 17000s, we find that:

★ The residues r1, r2, r3 and r4 have non-zero average values, these residues are therefore sensitive to this defect, which is confirmed, by the theoretical results presented in table 2 (see Figure 14).

★ Temperatures Th, Ta, Tw and Tm suffered declines in their speed at the moment of failure (see Figure 15).

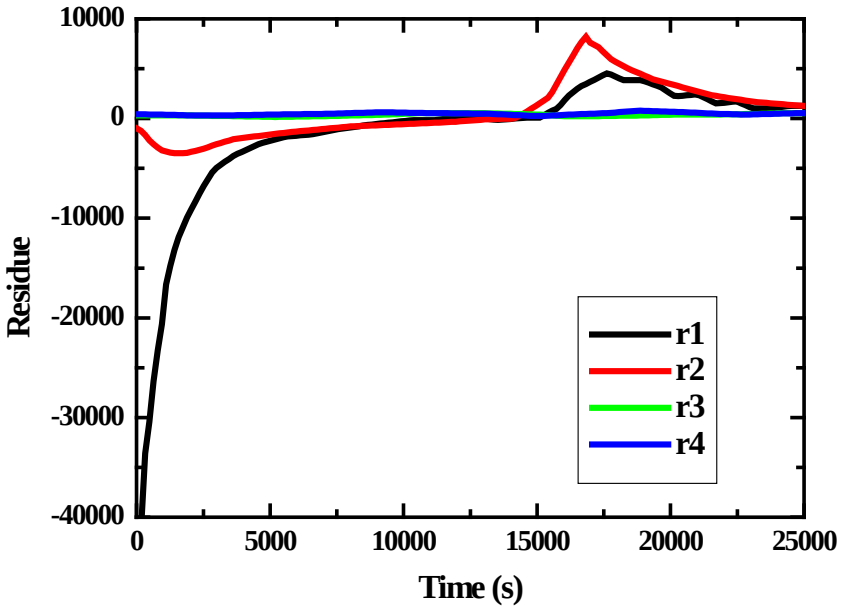

Fig. 14: Evaluation of Residues r_1, r_2, r_3 and r_4 in the Case of Default in Inside the Incubator

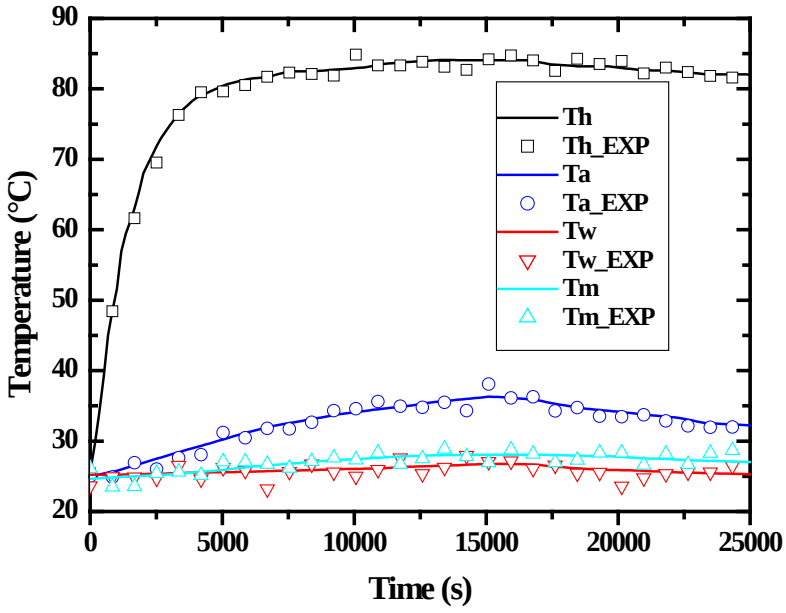

Fig. 14: Evaluation of Temperatures *Th, Ta, Tw* and *Tm* in the Case of Default in Inside the Incubator

VII. ROBUST DIAGNOSIS BY BOND GRAPHS

7.1 BG-LFT Model of the Incubator Flawless

Figure 16 shows the BG-LFT model of the incubator system flawless. To determine the residues, we must put the system in the form derivative and also put sensors under dialyzed.

- *Determination of residues flawless*

★ The junction 0_1 gives us as equation:

$$R_{d1} = f_3 - f_4 - f_5 + w_{Ch} + w_{1/Rh} + w_{1/Ra}$$

From this relation, we can deduce the residual equation Rd_1:

$$Rd_1 = \frac{T_{inp} - De_1}{Rh} - Ch.\frac{dDe_1}{dt} - \frac{n_1.(n_1.De_1 - De_2)}{Ra} + w_{Ch} + w_{\frac{1}{Rh}} + w_{\frac{1}{Ra}} \quad (21)$$

The equation consists of two parts: the first part is the normal evolution of the residual r_{1n} and the second part represents the residual uncertainty related to the evolution of the parameters d_1:

$$\begin{cases} Rd_1 = r_{1n} + d_1 \\ r_{1n} = \frac{T_{inp} - De_1}{Rh} - Ch.\frac{dDe_1}{dt} - \frac{n_1.(n_1.De_1 - De_2)}{Ra} \\ d_1 = w_{Ch} + w_{\frac{1}{Rh}} + w_{\frac{1}{Ra}} + w_{\frac{1}{Rw}} \end{cases}$$

★ The junction $\mathbf{0_2}$ gives us as equation:

$$Rd_2 = r_2 = f_8 - f_9 - f_{10} - f_{17} + w_{Ca} + w_{1/Ra} + w_{1/Rw}$$

From this relation, we can deduce the residual equation Rd_2:

$$Rd_2 = Ca.\frac{dDe_2}{dt} - \frac{De_1 - De_2}{Ra} - \frac{De_1 - De_3}{Rw} + w_{Ca} + w_{\frac{1}{Ra}} + w_{\frac{1}{Rw}} \quad (22)$$

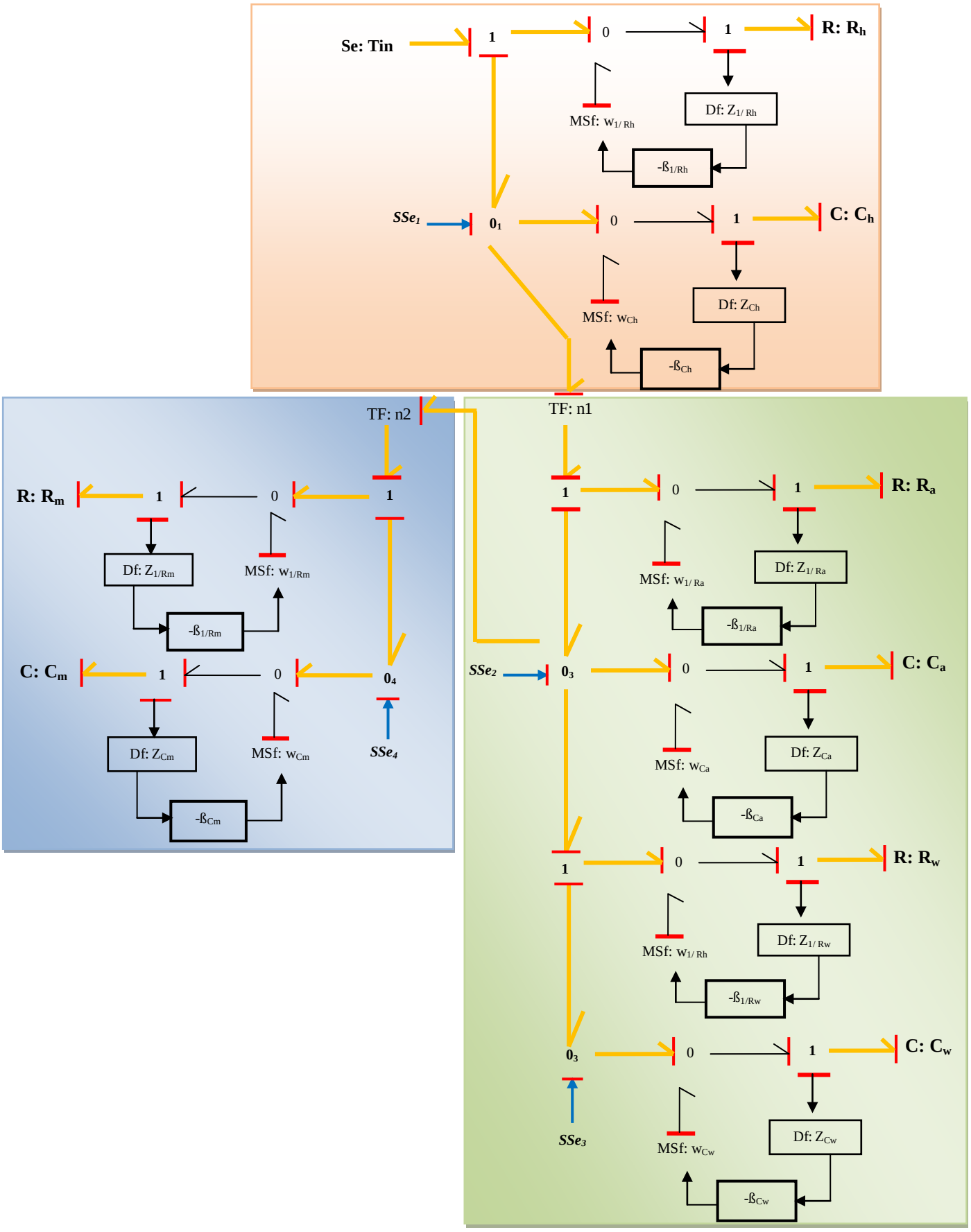

Fig. 16: GB-LFT Approach Incubator System with Derivative Mode

The equation consists of two parts: the first part is the normal evolution of the residual r_{1n} and the second part represents the residual uncertainty related to the evolution of the parameters d_1:

$$\begin{cases} Rd_1 = r_{1n} + d_1 \\ r_{1n} = \dfrac{T_{inp} - De_1}{Rh} - Ch.\dfrac{dDe_1}{dt} - \dfrac{n_1.(n_1.De_1 - De_2)}{Ra} \\ d_1 = w_{Ch} + w_{\frac{1}{Rh}} + w_{\frac{1}{Ra}} + w_{\frac{1}{Rw}} \end{cases}$$

★ The junction $\mathbf{o_2}$ gives us as equation:

$$Rd_2 = r_2 = f_8 - f_9 - f_{10} - f_{17} + w_{Ca} + w_{1/Ra} + w_{1/Rw}$$

From this relation, we can deduce the residual equation Rd_2:

$$Rd_2 = Ca.\frac{dDe_2}{dt} - \frac{De_1 - De_2}{Ra} - \frac{De_1 - De_3}{Rw} + w_{Ca} + w_{\frac{1}{Ra}} + w_{\frac{1}{Rw}} \quad (22)$$

The equation consists of two parts: the first part is the normal evolution of the residual r_{2n} and the second part represents the residual uncertainty related to the evolution of the parameters d_2:

$$\begin{cases} Rd_2 = r_{2n} + d_2 \\ r_{2n} = \dfrac{n_1.De_1 - De_2}{Ra} - Ca.\dfrac{dDe_2}{dt} - \dfrac{De_1 - De_3}{Rw} \\ - \dfrac{n_2.(n_2.De_2 - De_4)}{Rm} \\ d_2 = w_{Ca} + w_{\frac{1}{Ra}} + w_{\frac{1}{Rw}} + w_{\frac{1}{Rm}} \end{cases}$$

★ The junction $\mathbf{o_3}$ gives us as equation:

$$Rd_3 = f_{12} - f_{13} - f_{14} + w_{Cw} + w_{1/Rw} + w_{1/Rp}$$

From this relation, we can deduce the residual equation Rd_3:

$$Rd_3 = \frac{De_2 - De_3}{Rw} - Cw\frac{dDe_3}{dt} - \frac{De_3 - T_{ex}}{Rp} + w_{Cw} + w_{\frac{1}{Rw}} + w_{\frac{1}{Rp}} \quad (23)$$

The equation consists of two parts: the first part is the normal evolution of the residual r_{3n} and the second part represents the residual uncertainty related to the evolution of the parameters d_3:

$$\begin{cases} Rd_3 = r_{3n} + d_3 \\ r_{3n} = \dfrac{De_2 - De_3}{Rw} - Cw\dfrac{dDe_3}{dt} - \dfrac{De_3 - T_{ex}}{Rp} \\ d_3 = w_{Cw} + w_{\frac{1}{Rw}} + w_{\frac{1}{Rp}} \end{cases}$$

★ The junction $\mathbf{o_4}$ gives us as equation:

$$Rd_4 = f_{20} - f_{21} + w_{Cm} + w_{1/Rm}$$

According to these relations, one can deduce the residual equation Rd_4:

$$Rd_4 = \frac{n_2.(n_2.De_2 - De_4)}{Rm} - Cm\frac{dDe_4}{dt} + w_{Cm} + w_{1/Rm} \quad (24)$$

The equation consists of two parts: the first part is the normal evolution of the residual r_{4n} and the second part represents the residual uncertainty related to the evolution of the parameters d_4:

$$\begin{cases} Rd_4 = r_{4n} + d_4 \\ r_{4n} = \dfrac{n_2.(n_2.De_2 - De_4)}{Rm} - Cm\dfrac{dDe_4}{dt} \\ d_4 = w_{Cm} + w_{1/Rm} \end{cases}$$

7.2: BG-LFT Model of the Incubator with Faults

Figure 17 shows the BG-LFT model of incubator system with defaults. We have introduced seven faults, four parametric faults (Y_{Rh}, Y_{Ra},, Y_{Rw}, and Y_{Rm}) and two structural faults (Y_h *and* Y_a).

- *Determination of residues with faults*

★ The junction $\mathbf{0_1}$ gives us as equation:

$$R_{d1} = f_3 - f_4 - f_5 + w_1$$

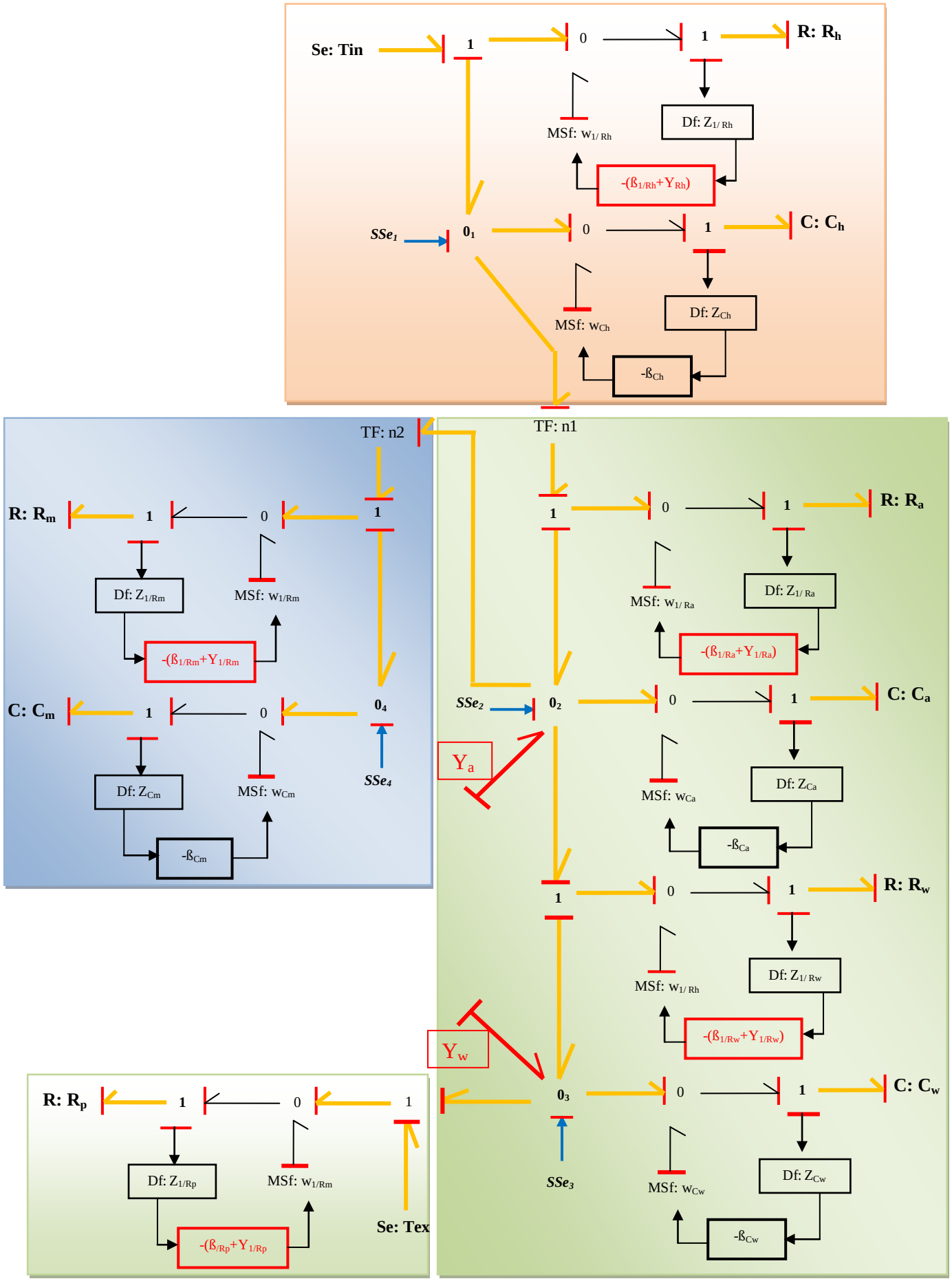

Fig. 17: BG-LFT Approach Incubator System With Derivative Mode and Four Parametric Faults (YRh, YRa,, YRw, and YRm) and Two Structural Faults (Ya and Yw)

According to these relations, one can deduce the residual equation Rd_1:

$$Rd_1 = \frac{T_{inp} - De_1}{Rh} - Ch.\frac{dDe_1}{dt} - \frac{n_1.(n_1.De_1 - De_2)}{Ra} + w_1 \quad (25)$$

With: $w_1 = w_{Ch} + w_{1/Rh} + w_{1/Ra} + Y_{1/Rh}.f_h + Y_{1/Ra}.f_a$

The equation consists of two parts: the first part is the normal evolution of the residual r_{1n} and the second part represents the residual uncertainty related to the evolution of the parameters d_1:

$$\begin{cases} Rd_1 = r_{1n} + d_1 \\ r_{1n} = \dfrac{T_{inp} - De_1}{Rh} - Ch.\dfrac{dDe_1}{dt} - \dfrac{n_1.(n_1.De_1 - De_2)}{Ra} \\ d_1 = w_1 \end{cases}$$

★ The junction $\mathbf{0_2}$ gives us as equation:

$$Rd_2 = f_8 - f_9 - f_{10} + w_2$$

According to these relations, one can deduce the residual equation Rd_2:

With: $w_2 = w_{1/Ra} + w_{1/Rw} + w_{Ca} + Y_{1/Ra}.f_a + Y_{1/Rw}.f_w + Y_a$

The equation consists of two parts: the first part is the normal evolution of the residual r_{2n} and the second part represents the residual uncertainty related to the evolution of the parameters d_2:

$$Rd_2 = Ca.\frac{dDe_2}{dt} - \frac{De_1 - De_2}{Ra} - \frac{De_1 - De_3}{Rw} + w_2 \quad (26)$$

$$\begin{cases} R_2 = r_{21n} + d_2 \\ r_{2n} = Ca.\dfrac{dDe_2}{dt} - \dfrac{De_1 - De_2}{Ra} - \dfrac{De_1 - De_3}{Rw} \\ d_2 = w_2 \end{cases}$$

★ The junction $\mathbf{0_3}$ gives us as equation:

$$Rd_3 = f_{12} - f_{13} + w_3$$

According to these relations, one can deduce the residual equation Rd_3:

$$Rd_3 = \frac{De_2 - De_3}{Rw} - Cw\frac{dDe_3}{dt} - \frac{De_3 - Tex}{Rp} + w_3 \quad (27)$$

With: $w_3 = w_{1/Rw} + w_{Cw} + Y_{1/Rw}.f_w + Y_w$

The equation consists of two parts: the first part is the normal evolution of the residual r_{3n} and the second part represents the residual uncertainty related to the evolution of the parameters d_3:

$$\begin{cases} Rd_3 = r_{3n} + d_3 \\ r_{3n} = \dfrac{De_2 - De_3}{Rw} - Cw\dfrac{dDe_3}{dt} - \dfrac{De_3 - Tex}{Rp} \\ d_3 = w_3 \end{cases}$$

★ The junction $\mathbf{0_4}$ gives us as equation:

$$Rd_4 = f_{20} - f_{21} + w_4$$

According to these relations, one can deduce the residual equation Rd_4:

$$Rd_4 = \frac{n_2.(n_2.De_2 - De_4)}{Rm} - Cm\frac{dDe_4}{dt} + w_4 \quad (28)$$

With: $w_3 = w_{1/Rw} + w_{Cw} + Y_{1/Rm}.f_m$

The equation consists of two parts: the first part is the normal evolution of the residual r_{4n} and the second part represents the residual uncertainty related to the evolution of the parameters d_4:

$$\begin{cases} Rd_4 = r_{4n} + d_4 \\ r_{4n} = \dfrac{De_1 - De_4}{Rm} - Cm\dfrac{dDe_4}{dt} \\ d_4 = w_4 \end{cases}$$

VIII. PERFORMANCE INDICES FOR INCUBATOR

8. 1: Sensitivity Index (SI)

Residue Rd_1*:*

$$\begin{cases} SI_1 = \dfrac{w_1}{d_1} \\ SI_1 = \dfrac{w_{\frac{1}{Rh}} + w_{\frac{1}{Ra}} + w_{Ch} + Y_{\frac{1}{Rh}}.f_h + Y_{\frac{1}{Ra}}.f_a}{d_1} \end{cases} \quad (29)$$

Residue Rd_2*:*

$$\begin{cases} SI_2 = \dfrac{w_2}{d_2} \\ SI_2 = \dfrac{w_{\frac{1}{Ra}} + w_{\frac{1}{Rw}} + w_{\frac{1}{Rm}} + w_{Ca} + Y_{\frac{1}{Ra}}.f_a + Y_{\frac{1}{Rw}}.f_w + Y_{\frac{1}{Rm}}.f_m + Y_a}{d_2} \end{cases} \quad (30)$$

Residue Rd_3*:*

$$\begin{cases} SI_3 = \dfrac{w_3}{d_3} \\ SI_3 = \dfrac{w_{\frac{1}{Rw}} + w_{\frac{1}{Rp}} + w_{Cw} + Y_{\frac{1}{Rw}}.f_w + Y_{\frac{1}{Rw}}.f_w + Y_w}{\blacksquare \text{ Residue } Rd_4\text{: } d_3} \end{cases} \quad (31)$$

Residue Rd_4*:*

$$\begin{cases} SI_4 = \dfrac{w_4}{d_4} \\ SI_4 = \dfrac{w_{\frac{1}{Rm}} + w_{Cm} + Y_{\frac{1}{Rm}}.f_m}{d_1} \end{cases} \quad (32)$$

8.2. Detectability index (DI)

Residue Rd_1 :
In this way, the defect detectability index of the residue Rd_1 is obtained:

$$DI_1 = w_1 - d_1$$

If $DI_1 \rangle 0$ then (37)

$$\begin{cases} w_1 \rangle d_1 \\ w_{\frac{1}{Rh}} + w_{\frac{1}{Ra}} + w_{Ch} + Y_{\frac{1}{Rh}} . f_h + Y_{\frac{1}{Ra}} . f_a \rangle d_1 \end{cases}$$

- The detectable rate $Y_{1/Rh}$ of a defect on the element R_h is calculated by supposing $Y_{1/Ra} = 0$

$Y_{1/Ra} = 0$

$$Y_{\frac{1}{Rh}} \rangle \frac{d_1 - (w_{\frac{1}{Rh}} + w_{\frac{1}{Ra}} + w_{Ch})}{f_h}$$

- The detectable rate $Y_{1/Ra}$ of a defect on the element R_a is calculated by supposing $Y_{1/Rh} = 0$

$Y_{1/Rh} = 0$

$$Y_{\frac{1}{Ra}} \rangle \frac{d_1 - (w_{\frac{1}{Rh}} + w_{\frac{1}{Ra}} + w_{Ch})}{f_a}$$

Residue Rd_2 :
In this way, the defect detectability index of the residue Rd_2 is obtained:

$$DI_2 = w_2 - d_2$$

If $DI_2 \rangle 0$ then

$$\begin{cases} w_2 \rangle d_2 \\ w_{\frac{1}{Ra}} + w_{\frac{1}{Rw}} + w_{\frac{1}{Rm}} + w_{Ca} + Y_{\frac{1}{Ra}} . f_a + Y_{\frac{1}{Rw}} . f_w \\ + Y_{\frac{1}{Rm}} . f_m + Y_a . f_{Ya} \rangle d_2 \end{cases} \quad (38)$$

- The detectable rate $Y_{1/Ra}$ of a defect on the element R_a is calculated by supposing $Y_{1/Rw} = Y_{1/Rm} = Y_a = 0$

$Y_{1/Rw} = Y_{1/Rm} = Y_a = 0$

$$Y_{\frac{1}{Ra}} \rangle \frac{d_2 - (w_{\frac{1}{Ra}} + w_{\frac{1}{Rw}} + w_{\frac{1}{Rm}} + w_{Ca})}{f_a}$$

- The detectable value $Y_{1/Rw}$ of a defect on the element R_w is calculated assuming $Y_{1/Ra} = Y_{1/Rm} = Y_a = 0$

$Y_{1/Ra} = Y_{1/Rm} = Y_a = 0$

$$Y_{\frac{1}{Rw}} \rangle \frac{d_2 - (w_{\frac{1}{Ra}} + w_{\frac{1}{Rw}} + w_{\frac{1}{Rm}} + w_{Ca})}{f_w}$$

- The detectable value $Y_{1/Rm}$ of a defect on the element R_m is calculated assuming $Y_{1/Ra} = Y_{1/Rw} = Y_a = 0$

$$Y_{1/Ra} = Y_{1/Rw} = Y_a = 0$$

$$Y_{\frac{1}{Rm}} \rangle \frac{d_2 - (w_{\frac{1}{Ra}} + w_{\frac{1}{Rw}} + w_{\frac{1}{Rm}} + w_{Ca})}{f_m}$$

- The detectable value Y_a of the structural defect is calculated assuming $Y_{1/Ra} = Y_{1/Rw} = Y_{1/Rm} = 0$

$$Y_{1/Rm} = 0$$

$$Y_a \rangle \frac{d_2 - w_{\frac{1}{Ra}} + w_{\frac{1}{Rw}} + w_{\frac{1}{Rm}} + w_{Ca}}{f_{Ya}}$$

Residue Rd_3 :
In this way, the defect detectability index of the residue Rd_3 is obtained:

$$DI_3 = w_3 - d_3 \tag{34}$$

If $DI_3 \rangle 0$ then

$$\begin{cases} w_3 \rangle d_3 \\ w_{\frac{1}{Rw}} + w_{\frac{1}{Rp}} + w_{Cw} + Y_{\frac{1}{Rw}} . f_w + Y_{\frac{1}{Rp}} . f_p + Y_w . f_{Yw} \rangle d_3 \end{cases}$$

- The detectable rate $Y_{1/Rw}$ of a defect on the element R_w is calculated by supposing $Y_{1/Rp} = Y_w = 0$

$$Y_{1/Rp} = Y_w = 0$$

$$Y_{\frac{1}{Rw}} \rangle \frac{d_3 - (w_{\frac{1}{Rw}} + w_{\frac{1}{Rp}} + w_{Cw})}{f_w}$$

- The detectable rate $Y_{1/Rp}$ of a defect on the element R_p is calculated by supposing $Y_{1/Rw} = Y_w = 0$

$$Y_{1/Rw} = Y_w = 0$$

$$Y_{\frac{1}{Rp}} \rangle \frac{d_3 - (w_{\frac{1}{Rw}} + w_{\frac{1}{Rp}} + w_{Cw})}{f_p}$$

- The detectable value Y_w of the structural defect is calculated assuming $Y_{1/Rw} = 0$

$$Y_w \rangle \frac{d_3 - (w_{\frac{1}{Rw}} + w_{\frac{1}{Rp}} + w_{Cw})}{f_{Yw}}$$

Residue Rd_4 :
In this way, the defect detectability index of the residue Rd_3 is obtained:

$$DI_4 = w_4 - d_4 \tag{40}$$

If $DI_4 \rangle 0$ then

$$\begin{cases} w_4 \rangle d_4 \\ w_{\frac{1}{Rm}} + w_{Cm} + Y_{\frac{1}{Rm}} . f_m \rangle d_4 \end{cases}$$

- The detectable rate $Y_{1/Rm}$ of a defect on the element R_w is calculated by the equation:

$$Y_{\frac{1}{Rm}} \rangle \frac{d_4 - (w_{\frac{1}{Rm}} + w_{Cm})}{f_m}$$

IX. CONCLUSION

In this paper, we presented diagnostic methods using the Bond Graph approach. The analytical redundancy relationships generated using the parity space method depends on the knowledge of the degree of derivations to be applied. The advantages of using the last method are: simplicity of understanding (*ARRs*) since they correspond to relationships and variables that are displayed by the leap graph model, and then the transition to the *LFT* form made by a simple addition of modulated sources of effort and flow on the model, image of the physical process, *ARRs* are deduced directly from the graphical representation, they can be generated in symbolic form and therefore adapted to a computer implementation.

ACKNOWLEDGEMENTS

We thank the National School of Engineers of Tunis, University of Tunis El Manar to support our work.

REFERENCES

1. Valentin Gies and Thierry Soriano. *Modeling and Optimization of an Indirect Coil Gun for Launching Non-Magnetic Projectiles*. Journal Actuators, pp: 8-39, 2019.
2. Tho N.H.T. Tran, Lawrence H. Le, Vu-Hieu Nguyen, Kim-Cuong T. Nguyen, Mauricio D. Sacchi. *Sensitivity analysis of leaky Lamb modes to the thickness and material properties of cortical bone with soft tissue: A semi-analytical finite element based simulation study*. IEEE International Ultrasonics Symposium (IUS), pp: 1-4, 2015.
3. Tai Le, Hervé Colin, Franck Al Shakarchi, Tuan Tran Quoc. *Improved Matlab Simulink Two-diode Model of PV Module and Method of Fast Large-Scale PV* System Simulation. 7th International Conference on Renewable Energy Research and Applications (ICRERA). pp: 982 - 985, 2018.
4. Naima Sakami, Lahcen Boukhattem , Hassan Hamdi. *Dynamic modelisation of heat transfer between the ground and shallow basment of a villa in Marrakesh area*. International Renewable and Sustainable Energy Conference (IRSEC). pp 867 – 871, 2016.
5. M. Shaib, M. Rashid, L. Hamawy, M. Arnout, I. El Majzoub, A. J. Zaylaa. *Advanced portable preterm baby incubator*. Fourth International Conference on Advances in Biomedical Engineering (ICABME), pp 1-4,2017.
6. Rebecca Hirte, Jürgen Münch, Laura Drost. *Incubators in Multinational Corporation's development of a corporate incubator operator model*. International Conference on Engineering, Technology and Innovation (ICE/ITMC), pp : 195 – 202, 2017
7. Gamze Tilbe Sen ; Mehmet Yüksekkaya. *Desing and Test of an Incubator Analyzer*. 2018 2nd International Symposium on Multidisciplinary Studies and Innovative Technologies (ISMSIT) , pp: 1-5, 2018.
8. B. Ashish. *Temperature monitored IoT based smart incubator*. 2017 International Conference on I-SMAC (IoT in Social, Mobile, Analytics and Cloud) (I-SMAC), pp: 497 – 501, 2017.
9. Muslim Ali, Murtada Abdelwahab, Sally Awadekreim, Suliman Abdalla. *Development of a Monitoring and Control System of Infant Incubator*. 2018 International Conference on Computer, Control, Electrical, and Electronics Engineering (ICCCEEE), pp : 1-4, 2018.
10. Bibo Dai, Hongting Wang. *Operation Efficiency Evaluation of Science and Technology Enterprise Incubator*. 2017 10th International Symposium on Computational Intelligence and Design (ISCID), pp : 38 – 42, Volume: 2, 2017.

11. Arif Widianto, M. Raditya Gumelar, Pradipta Mahatidana, Rizky Ramadian Wijaya; Intan Nurfitri, Kresna Devara, Retno Wigajatri Purnamaningsih. *The effect of moving load on remote weight monitoring system for simple infant incubator*. 2017 International Conference on Broadband Communication, Wireless Sensors and Powering (BCWSP), pp: 1-4, 2017.
12. Dhanesh Kattipparambil Rajan, Jarmo Verho, Joose Kreutzer, Hannu Välimäki, Heimo Ihalainen, Jukka Lekkal, Mimmi Patrikoski, Susanna Miettinen. Monitoring pH, temperature and humidity in long-term stem cell culture in CO2 incubator. 2017 IEEE International Symposium on Medical Measurements and Applications (MeMeA), pp: 470 – 474, 2017.
13. Nor Asmidar, Natasha Binti, Mohd Fudzi, Nurmiza Binti. *Development of infant incubator for clinic in the rural area of Malaysia*. 2016 IEEE EMBS Conference on Biomedical Engineering and Sciences (IECBES), pp : 331'334, 2016.
14. Kubilay Tan ; Ahmet Reşit Kavsaoğlu ; Onur Koçak ; Cansu Akbay. *Remote Monitoring System For Incubator Data*. 2018 Medical Technologies National Congress (TIPT EKNO), pp : 1-4, 2018.
15. Megha Koli ; Purvi Ladge ; Bhavpriya Prasad ; Ronak Boria ; Prof. Nazahat J. Balur. *Intelligent Baby Incubator*. 2018 Second International Conference on Electronics, Communication and Aerospace Technology (ICECA), pp: 1036 – 1042, 2018.
16. B. Li, B. Liu, and A. Toguyéni. *On-the-fly Diagnosability Analysis of Labeled Petri Nets Using Minimal Explanations*. In 9th IFAC Symposium on Fault Detection, Supervision and Safety for Technical Processes - SAFEPROCESS' 2015, 2015.
17. Estrada-Vargas A.-P., Lesage J.-J et Lopez-Mellado E. *Identification of Partially Observable Discrete Event Manufacturing Systems*. IEEE 18th Conference on Emerging Technologies and Factory Automation, ETFA, Cagliari, Italy, 2013.
18. Tapia-Flores T., Lopez-Mellado E., Estrada-Vargas A.-P. et Lesage J.-J. *Petri Net Discovery of Discrete Event processes by Computing T-invariants*. IEEE 19th Conference on Emerging Technologies and Factory Automation, ETFA, Barcelona, Spain, 2014.
19. H. Leroux, D. Andreu, and K. Godary-Dejean. *Handling exceptions in petri net-based digital architecture: from formalism to implementation on fpgas*. IEEE Transactions on Industrial Informatics, 11(4):897–906, 2015.
20. H. Leroux, K. Godary-Dejean, and D. Andreu. *Complex digital system design: A methodology and its application to medical implants*. In International Workshop on Formal Methods for Industrial Critical Systems, pages 94–107. Springer, 2013.
21. B. Li, A. Toguyéni, and M. Khlif-bouassida. *On-the-fly Diagnosability Analysis of Labeled Petri Nets Using T-invariants*. In 5th International Workshop on Dependable Control of Discrete Systems - DCDS'2015, 2015.
22. Sankaranarayanan S., Sipma H. B., Manna Z., *Petri Net Analysis Using Invariant Generation*, Verification : Theory and Practice (Essays Dedicated to Zohar Manna on the Occasion of His 64th Birthday), n° 2772 in LNCS, Springer, p. 682-701, 2004.
23. Geeraerts G., Raskin J.-F., Van Begin L., *On the efficient Computation of the Minimal Coverability set of Petri nets*, ATVA '07 : Proc. of 5th Int. Symp. on Automated Technology for Verification and Analysis, vol. 4762 of LNCS, Springer, p. 98-113, 2007.
24. Ju Biao Yao, Zhu Ming Cao and Jia Tian Guo, *The Research of Hybrid Bond Graph Modeling* . IOP Conf. Series: Journal of Physics: Conf. Series 1087 (2018) 052013 doi :10.1088/1742-6596/1087/5/052013.
25. Belkacem Ould Bouamama, Ibrahim Abdalah and Anne-Lise Gehin. *Bond Graphs as Mechatronic Approach for Supervision Design of Multisource Renewable Energy System*. IOP Conference Series: Materials Science and Engineering, Volume 417, 5th International Conference on Mechanics and Mechatronics Research (ICMMR 2018)19–21 July 2018, Tokyo, Japan

26. S. Samaddar, P. Kushwaha and S. K. Ghoshal, *Bond graph modelling and simulation of a variable inertia flywheel.* IOP Conf. Series: Materials Science and Engineering 377 (2018) 012206 doi:10.1088/1757-899X/377/1/012206.
27. Borutzky W. Bond graphs for modelling, control and fault diagnosis of engineering systems. New York: Springer Science & Business Media, 2017.
28. M. Bendaoud, H.Hihi,b and K. Faitah. Structural Controllability of Switched Linear Singular Systems Modelled by Bond Graph. International Journal of Engineering Research in Africa. Vol. 38, pp 26-45, 2018.
29. Abdallah I, Gehin A-L, Bouamama BO. Functional hybrid bond graph for operating mode management. IFACPapersOnLine 2016;49:327e32.
30. Gawthrop PJ, Bevan GP. Bond-graph modeling. IEEE control Syst 2007;27:24e45.
31. Simon BN Jr, Reddy NP, Kantak A, A theoretical model of infant incubator dynamics, J Biomech Eng. 1994 Aug;116 (3):263-9.
32. Pauline Décima, Loïc Dégrugilliers, Stéphane Delanaud, Erwan Stephan, Jean-Luc Vanhée, J.-P. Libert, Conception d'un logiciel de calcul de la thermoneutralité dans les incubateurs fermés pour nouveau-nés prématurés (projet Pretherm®) April 2012 IRBM 33(2):48–54
33. Mohamed aymen Zermani, Feki Elyes, Abdelkader Mami, Building simulation model of infant-incubator system with decoupling predictive controller September 2014 IRBM 35(4)
34. Andrés Fraguela , Francisca . Matlalcuatzi , Ángel M. Ramos, Mathematical modelling of thermoregulation processes for premature infants in closed convectively heated incubators Comput Biol Med. 2015 Feb;57:159-72
35. Stéphane Delanaud, Pauline Decima, Amandine Pelletier, Jean-Pierre Libert, Estelle Durand, Erwan Stephan-Blanchard, Véronique Bach, Pierre Tourneux, Thermal management in closed incubators: New software for assessing the impact of humidity on the optimal incubator air temperature, Medical Engineering & Physics · 46 2017, 98-95.
36. J. S. Ultman, S. Berman, P. Kirlin, J.M. Vireslovic, C.B. Baer, K.H. Marks, "Electrically heated simulator for relative evaluation of alternative infant incubator environments", Med. Instrum., 1988, vol. 22(1), pp.33-8.
37. M. H. LeBlanc, "The physics of thermal exchange between infants and their environment", AAMI Technology Assessment Report, Feb. 1987. Vol. 21 (No.1), pp. 11-15.
38. Saumya Ranjan Sahoo , Shital. S. Chiddarwar. Mobile Robot Control Using Bond Graph and Flatness Based Approach. Procedia Computer Science 133 (2018) 213–221.
39. Vijay P, Samantaray A, Mukherjee A. A bond graph modelbased evaluation of a control scheme to improve the dynamic performance of a solid oxide fuel cell. Mechatronics 2009;19:489e502.
40. Vijay P, Samantaray A, Mukherjee A. Bond graph model of a solid oxide fuel cell with a c-field for mixture of two gas species. Proc Institution Mech Eng Part I J Syst Control Eng 2008;222:247e59.
41. Hassan. Javed, A. Mahmood. A Study of Thermodynamics and Bond Graph Modelling of Evaporation in Infant Incubator. Conference Paper (PDF Available) · December 2013 with 212 Reads.
42. H., Paynter, *Analysis and design of engineering systems*, (M.I.T.Press, 1961).
43. S. Ben Mabrouk ,H. Oueslati ,R. Andoulsi " Bond- Graph modelling of water evaporation in a convective solar dryer" Proc. Of The Seventh International Conference on Renewable Energies and the Environmen eds, Tunisia, pp.1-12,2013,in press.
44. D.C., Karnopp. and R.C., Rosenberg, *Systems Dynamics: a Unified Approach*, (Mac Graw Hill, 1983).
45. R.C., Rosenberg, *Introduction to physical System Dynmics*, Series in mechanical engineering, (Mac Graw Hill, 1983).
46. M., Tagina. and G., Dauphin, Tanguy, *La méthodologie bond graph. Principes et applications*, (Centre de Publication Universitaire, 2003).

47. A., Sallami, N., Zanzouri, B., OuldBouamama, Robust Supervision of Industrials Systems by Bond Graph and External Models, *International Journal of Enhanced Research in Science Technology & Engineering*, 5 (2016) 245–258.
48. A., Sallami, N., Zanzouri, K, Mekki, Robust Fault Diagnosis Observer of Dynamical Systems Modelled by Bond Graph Approach, *8th IFAC Symposium on Fault Detection, Supervision and Safety of Technical Processes (SAFEPROCESS)*,12(2012), pp. 415–420.
49. M.A., Djeziri, B., OuldBouamama and R., Merzouki, *Modelling and robust FDI of steam generator using uncertain bond graph model*. J. Process Control, 19 : (2009) 149-162. DOI:10.1016/j.jprocont.(2007).12.009.
50. Z., Han, W., Li and S.L., Shah, *Fault detection and isolation in the presence of process uncertainties*. Proceedings of the 15th IFAC World Congress, (WC' 02), (2002) pp: 1887-1892.
51. D., Henry, D. and A. Zolghari, *Norm-based design of robust FDI schemes for uncertain systems under feedback control: Comparison of two approaches*. Control Eng. Pract., 14: (2006) 1081-1097. DOI: 10.1016/j.coneng-prac.
52. M.A., Djeziri, B., OuldBouamama and R., Merzouki, *Modelling and robust FDI of steam generator using uncertain bond graph model*. J. Process Control, 19 : (2009) 149-162. DOI:10.1016/j.jprocont.(2007).12.009.
53. D., Alazard, C., Cumer, P., Apkarian, M., Gauvrit and G. Fereres, *Robustesse et Commande Optimale*. 1st Edn., Cépadues-Editions, Toulouse, ISBN-10: (199) 2854 285166, pp: 348.
54. A., Oustaloup. *La robustesse*. 1st Edn., Hermès, ISBN-10: (1994) 2.86601.442.1.
55. M.A., Djeziri, *Diagnostic des systèmes incertains par l'approche bond graph*. Thèse de Doctorat, École Centrale de Lille (2007).